Mitteilungen 131

Converging Glacier Flow – A Case Study: the Unteraarglacier

G. Hilmar Gudmundsson

Zürich, 1994

Herausgeber: Prof. Dr. Dr.h.c. D. Vischer

Preface

A recent investigation of a Greenlandic ice stream has raised the question whether an ice stream flowing through a convergent bedrock channel may experience a special type of ice deformation, influencing its internal temperature distribution and thus its surface velocity. This was the starting point for the present study of a glacier confluence which represents a well defined special case of converging flow. At the confluence of a glacier the flow field is fully three-dimensional. The now available numerical methods make it possible to simulate this type of flow for a nonlinear rheology.

In the present study Dr. Hilmar Gudmundsson combines the results of extensive, thorough field measurements which he has conducted at the confluence of an Alpine glacier with those from his numerical modelling. In this way he elucidates the complex flow field. He can show that an exponent $n = 3$ in Glen's flow law provides the best agreement of numerical and experimental results, and also that this flow law is not perfectly suited for describing ice flow under strongly three-dimensional conditions. By designing and analyzing two complementary 2D-models he brings out the typical features of flow in a confluence. The work presented here refers to essentially non-sliding conditions. However, certain changes to be expected if sliding is significant can be inferred from a related study published as the preceding volume of this series (H. Gudmundsson: Glacier sliding over sinusoidal bed and the characteristics of creeping flow over bedrock undulations).

This study will be a valuable help for interpreting certain features of ice stream flow and also for understanding flow and erosive patterns at glacier confluences in general.

This research has been funded by the Swiss National Science Foundation. Support from the Kraftwerke Oberhasli made it possible to print the graphs in colours, this is gratefully acknowledged.

Almut Iken

Contents

List of Figures

List of Tables

List of Symbols

Dimensional quantities are usually in lower case letters and non-dimensional quantities in capital letters. Symbols used in Sub-sec. 4.2.2 are however an exception to this rule, in which all variables, upper as well as lower case, are non-dimensional.

A	softness parameter, a constant in Glen's flow law
A_b	"best" value of A
A_c	the value of A used for the calculation of $\mathbf{v}^c$
$A(k)$	integration function
$B(k)$	integration function
C	parameter in Weertman-type sliding law
$C(k)$	integration function
$D(k)$	integration function
d	one half of glacier width
E_{ij}	non-dimensional strain rate
e	total strain
f_A	scaling factor, $A_b = f_A A_c$
g	acceleration of gravity
k	wavenumber
n	parameter in Glen's flow law
P	non-dimensional pressure, defined through Eq. 4.11
P_i	the projection of $\mathbf{R}_i$ on $\mathbf{v}_i^c/v_i^c$; $P_i := \mathbf{v}_i^c(\mathbf{v}_i^m - f_A\mathbf{v}_i^c)/(v_i^m v_i^c)$
p	mean normal pressure, for incompressible media defined as: $p := -\frac{1}{3}\sigma_{ii}$
p_a	atmospheric pressure
R	the vector length of the sum over all error vectors
$\mathbf{R}_i$	error vector; $\mathbf{R}_i := (\mathbf{v}_i^m - f_A\mathbf{v}_i^c)/v_i^m$
S_v	normalized root-mean-square error, defined through Eq. 5.3
s_v	standard deviation of velocities, defined through Eq. 5.1
T	non-dimensional time, defined through Eq. 4.11
t	time
U	non-dimensional channel velocity, $u = 2AR\tau_b^n U$
V_X, V_Z	non-dimensional velocities, defined through Eq. 4.12
v	speed; $v = \sqrt{v_x^2 + v_y^2 + v_z^2}$
v_h	horizontal speed; $v_h := \sqrt{v_x^2 + v_y^2}$
$\mathbf{v}^c(x, y, z)$	calculated velocity field
$\mathbf{v}^m(x, y, z)$	measured velocity field
$\mathbf{v}_i^m$	measured velocity of marker i
$\mathbf{v}_i^c$	calculated velocity at the position of marker i
v_i	components of velocity vector, $\mathbf{v} = (v_x, v_y, v_z) = (u, v, w)$
x, y, z	space coordinates
X, Z	non-dimensional space coordinates; $(X, Z) = k(x, z)$
z_0	position of glacier bed

α	surface slope
$\hat{\alpha}$	defined as $\hat{\alpha} := e^k$
β_{ij}	regression coefficients
$\hat{\beta}$	defined as $\hat{\beta} := e^{-k}$
$\Delta_{\dot{\epsilon}}$	strain-rate residual, defined through Eq. 3.4
δ_{ij}	Kronecker delta
$\hat{\delta}$	defined as $\hat{\delta} := ke^{-k}$
$\dot{\epsilon}_{ij}$	components of strain-rate tensor; $\dot{\epsilon}_{ij} = \frac{1}{2}(v_{i,j} + v_{j,i})$
$\dot{\epsilon}_3^s$	vertical surface strain rate
$\dot{\epsilon}$	effective strain rate; $\dot{\epsilon} := \sqrt{\frac{1}{2}\dot{\epsilon}_{ij}\dot{\epsilon}_{ij}}$
η	viscosity
$\hat{\gamma}$	defined as $\hat{\gamma} := ke^k$
λ	wavelength
ρ	specific density
Σ_{ij}	non-dimensional stresses, defined through Eq. 4.13
σ'_{II}	second deviatoric stress invariant; $\sigma'_{II} := \frac{1}{2}\sigma'_{ij}\sigma'_{ij}$
σ_{ij}	components of stress tensor
σ'_{ij}	components deviatoric stress tensor, $\sigma'_{ij} := \sigma_{ij} - \frac{1}{3}\delta_{ij}\sigma_{kk} = \sigma_{ij} + p$
σ_n	component of the stress tensor normal to the bed
σ'_n	component of the deviatoric stress tensor normal to the bed
σ_M	von Mises stress; $\sigma_M := (\frac{3}{2}\sigma'_{ij}\sigma'_{ij})^{1/2}$, *i.e.* $\sigma_M = \sqrt{3\sigma'_{II}}$
σ_p	component of the stress tensor parallel to the bed
σ'_p	component of the deviatoric stress tensor parallel to the bed
τ	effective stress; $\tau := \sqrt{\sigma'_{II}}$
τ_b	basal shear stress or driving stress; $\tau_b := \rho_I g h \sin\alpha$

Suffices

I	properties of ice
B	properties of bedrock
b	basal properties
p	parabolic

Abstract

Theoretical and experimental work concluded on the confluence area of the Unteraarglacier is discussed. With the help of simple conceptual models the general flow characteristics of converging flow are elucidated and general inferences drawn regarding the stress and strain regime of a glacial confluence.

The experimental work was done in the period from spring 1991 to spring 1993. It consisted of radio-echo soundings, measurements of marker velocities, determination of surface strain rates, vertical velocity variation, and ice temperature measurements. The confluence centerline was found to be subjected to longitudinal horizontal extension and a concomitant transversal compression, with the longitudinal extension exceeding the transversal compression. Vertical strain rates change from positive (extension) at the surface to negative (compression) in the lowest layers of the glacier.

A 2D map-plane model and a 2D flow-line model are used to explain the observed strain-rate pattern. It is concluded that, as a response to the change in boundary conditions at a glacier confluence, a surface depression will form at the junction point, and two super-elevated zones at the glacier margins of the two contributing tributaries facing the junction point will be created.

For a fully 3D model, flow velocities are calculated using Glen's flow law.

All features of the measured flow field of the Unteraarglacier, such as the horizontal and vertical strain-rate pattern, as well as the spatial velocity variation, can be reproduced qualitatively within that model. A quantitative comparison, however, shows the presence of systematic differences between measured surface velocities and velocities calculated with Glen's flow law for all values of n, where n is a flow law parameter.

Zusammenfassung

Durch kombinierten Einsatz von theoretischen, numerischen wie auch experimentellen Methoden wurde der Bereich des Zusammenflusses des Finsteraar- und Lauteraargletschers untersucht.

Die experimentellen Arbeiten wurden in der Zeitspanne von Frühling 1991 bis Frühling 1993 durchgeführt. Unter anderem wurden Gletschertiefen, Oberflächengeschwindigkeiten, zeitliche Geschwindigkeitsänderungen, Dehnungsraten und Eistemperaturen gemessen. Im Bereich des Zusammenflusses herrscht an der Oberfläche quer zur Fließrichtung eine starke horizontale Stauchung und entlang der Fließrichtung eine horizontale Dehnung. Die vertikalen Dehnungsraten sind an der Oberfläche positiv, wechseln aber zu negativen Vorzeichnen im untersten Teil des Gletschers.

Vereinfachte 2D-Modelle zeigen, daß wegen der Änderung der Randbedingungen die beim Zusammenfluß zweier Gletscher erfolgen, notwendigerweise ein Einsinken der Oberfläche beim Vereinigungspunkt stattfindet, und daß sich auf den beiden gegenüberliegenden Seiten Zonen erhöhter Topographie bilden.

Mit Hilfe eines 3D-Modells wurde der Zusammenfluß des Unteraargletschers unter Annahme eines nicht-linearen Fließgesetzes modelliert. Eine gute qualitative Übereinstimmung zwischen gemessenen und berechneten Größen wurde festgestellt. Eine genauere Betrachtung zeigte jedoch, daß unter Anwendung des in der Gletschermechanik üblichen Glen'schen Fließgesetzes systematische Abweichungen immer vorkommen.

CHAPTER 1

Introduction

Almost all analyses of measurements of ice deformation of alpine glaciers to date have been done with the help of one or two-dimensional models in spite of the fact that the influence of the third dimension (friction from walls, transverse compression/stretching due to converging/diverging flow, *etc.*) is often large. The effect of the third dimension on the stress field of 2D flow-line models has usually been accounted for by introducing form factors. Form factors can, however, only be considered as a crude correction for three-dimensional effects since: 1) they only give the "average" influence of the third dimension, and 2) because they do not take into account the influence of longitudinal stress gradients. In fact form factors are often used to improve the agreement between measurements and numerical modeling; they become a set of adjustable parameters. Such models have greatly reduced predictive power and cannot be used to estimate the rheological behavior of glacier ice.

The development of fully 3D-models with non-linear rheology has recently become feasible opening up completely new horizons in glaciology. One no longer has to rely on gross simplification but can tackle the problems in their full generality. Studies of glaciers situated in complex terrains where 3D effects must be expected to be of importance, are hence now possible.

There is a number of commonly found flow geometries where stress and strains gradients in all three spatial directions are important and where three-dimensional effects cannot be ignored; the confluence of two glaciers is one of the best examples. In a confluence area one would also expect the internal deformation of ice to decisively influence the overall flow behavior — the glacier having to adjust itself over a small distance to a completely different bed configuration — and it is therefore an ideal place to study the mechanism of ice deformation.

The mechanics of ice deformation that are specific to a confluence are also important in themselves. Most alpine glaciers form confluence areas where two or more glaciers flow together. Sometimes spectacular over-deepenings are known to be associated with such areas, Konkordiaplatz being the best know example in the Alps, and it has been speculated that the flow pattern of the confluence can cause enhanced glacial erosion. It has also been suggested that lateral compression of two converging ice streams is responsible for the form of medial moraines, but this has been debated (*cf.* Sec. 2.2). The possibility of transverse flow caused by the changes in the mechanical boundary conditions associated with a convergence (*cf.* Sec. 2.3) is yet another open question that deserves further consideration.

1.1 Goals of the project

The goal of this project is to gain a better understanding of the general flow characteristics of a confluence area, and to test the applicability of theoretical concepts to an actual glacier flow situation.

To this end a detailed experimental and theoretical study was to be done on one particular confluence area of two glaciers. The merging of the Finsteraar and Lauteraar to form the Unteraarglacier was chosen for this purpose. The reasons for this choice are: the confluence is approximately symmetrical, the angle between the two tributaries is large (about 180°), the glacier lies on a hard bed so that deformation of sediments does not contribute to the flow (*cf.* Sec. 3.2), and there was a considerable knowledge of the bed geometry and the surface velocity variations available from previous field work.

With the help of conceptual models the universality of the findings from the work done on the Unteraarglacier shall be investigated.

1.2 Organization

Chapter 2 discusses previous work, which has mainly concentrated on the deformation pattern at the surface of a confluence. No previous numerical modeling of the confluence of two glaciers has been done.

The field work done on the Unteraarglacier is described in Chapter 3. Separate sections are on the previous field work and the field work done as a part of this project.

In Chapter 4 two simple conceptual models of a confluence are presented. One of the models is a flow-line model and is used to understand the vertical strain-rate variation with depth for the glacier section from the junction point toward the center of the confluence. The other is a map-plane model, and is used to investigate the general flow pattern caused by the change of boundary condition at the junction point.

The non-linear fully 3D model of the confluence area of the Unteraarglacier is described and discussed in Chapter 5. A quantitative comparison between measurements and numerical calculations is used to test the correctness of the form of the flow law. Emphasis is also put on what can be learned about the general flow pattern of glacier confluences.

A summary of results and recommendations for further work are given in Chapter 6.

Chapter 2

Previous Work on Confluences

Relatively few studies have been done on the ice-mechanics of a glacier confluence. The most probable explanation for this is the complexity of flow field which requires fully three-dimensional flow modeling — something which has so far hardly been feasible. Several studies have, however, been done on surface velocity patterns and morphological features of confluence areas. The formation and the subsequent development of medial moraines, resulting from the merging of two glaciers, has been investigated in a number of papers (references given below).

The most detailed work done so far on the converging of two glaciers seems to be the that done on Kaskawulsh Glacier, Yukon Territory, Canada as a part of the Icefield Ranges Research Project. Among other things the bedrock topography, surface velocity, crevasses and morphological features were studied (Anderton, 1970; Clarke, 1969; Brecher, 1969; Wagner, 1969a; Wagner, 1969b; Dewart, 1970; Holdsworth, 1969a; Holdsworth, 1969b; Ewing, 1970; Dozier, 1970). The flow pattern of the confluence of Tyndall Glacier, southern Patagonia, has also been studied, but not in sufficient detail to give any information on the strain-rate pattern (Kadota *et al.*, 1992; Casassa, 1992).

2.1 Velocity field

Measurements of surface ice deformation at the confluence of the north and central arms of the Kaskawulsh Glacier showed how the independent profiles across each arm progressively change towards an unified profile across the combined glacier, resulting in a continuous flow field with no sign of discrete shear along the median line (Anderton, 1970). A morphological study of the medial moraine, however, revealed several instances of vertical or near vertical shear planes oriented in the direction of flow and sometimes showing an offset of few centimeters indicating a discrete slip or shear (Loomis, 1970). Loomis concluded that there was a line of velocity discontinuity along a medial moraine, at least close to the junction, which was several centimeters greater than the ablation rate, estimated to be 6 to 7 cm/d.

Differential velocities have also been measured across the contact line of the north and the south Arms of Berendon Glacier, British Colombia, Canada (Eyles and Rogerson, 1977) as well as on Blue Glacier, Washington (Allen *et al.*, 1960).

Up-glacier from the point of confluence of Kaskawulsh Glacier the north arm had a maximum annual velocity of 215 m/a, while the central arm showed a substantially smaller maximum annual velocity of only 152 m/a. There where indications of marginal sliding of the north arm but not of the central arm. The north arm is somewhat less deep than the central arm which has a maximum depth of 1000 m. No bedrock depression was found at the confluence (Dewart, 1970).

Determination of surface strain rates across both arms of Kaskawulsh Glacier showed the principal compressive strain rates to lie parallel, and the extending strain rates transverse to the direction of flow. But along the medial moraine the opposite was true, with transverse horizontal compression exceeding longitudunal horizontal extension and hence indicating vertical extension close to the surface (Anderton, 1970).

2.2 Medial moraines

In addition to the work of Loomis (1970) there exist a few morphological studies of medial moraines formed at the convergence of valley glaciers. While Loomis (1970), Gomez and Small (1985) and Vere and Benn (1989) conclude that differential ablation of bare and protected ice is responsible for the formation of medial moraines, Eyles and Rogerson (1977, 1978) suggest that in many instances the dynamics of the flow determine the morphology of medial moraines, and they give the immediate confluence area of the north and the south arm of Berendon Glacier as an example for this type of moraine formation. They introduced the terms *ice-stream interaction* model and *ablation dominant* model to describe these two different modes of moraine formation. This mechanical aspect of medial moraine formation and its relative importance to differential ablation has however been a subject of debate (Eyles, 1976a; Small and Clark, 1976a; Eyles, 1976b; Small and Clark, 1976b) and cannot be definitely resolved unless the dynamics of a confluence area are known in sufficient detail.

If the dynamics of flow are mainly responsible for the formation of a medial moraine it is, however, difficult to understand why the width of the moraines is always limited to the width of the supra-glacier debris cover. It is also not clear how a zone of transversal compression can originate that is sufficiently localized as to give rise to a medial moraine. One might rather expect the dynamics of a confluence area to introduce some modifications of the surface geometry that would have wavelengths comparable to the thickness or the width of the converging glaciers. Indeed this is what Collins (1970) did find in his slip-line field analysis of deformation at the confluence of two glacier streams. Interaction between two ice streams may cause the debris to take on the form of a longitudinal septum but differential ablation seems to be the cause of the moraine formation (Smiraglia, 1989).

2.3 Theoretical approach

Collins (1970) calculated the deformation and stress field at the junction of two glaciers by assuming ideal rigid/perfectly plastic material behavior of ice. Further assumptions included that of rigid "plug flow" movement of the ice above and below the confluence zone, and that of plane strain deformation (thereby reducing the problem to two dimensions). As boundary conditions perfectly lubricated as well as perfectly rough walls were used. The assumption of ideal rigid/perfectly plastic material behavior means that the deformation takes the form of regions of finite strain rates and lines (slip lines) of tangential velocity discontinuities. For a symmetrical junction Collins found that there is a velocity discontinuity across the mouth of both confluencing streams as long as the ratio of the velocities up-stream from the junction is not too far from unity. If this ratio becomes larger than a specific critical ratio, which is dependent on the angle of the junction, there will be a line of velocity discontinuity across the mouth of the weaker stream only, but another slip line forms across the down-stream mouth of the confluence. These slip lines should correspond to narrow bands of intense shear on real glaciers.

In plane-strain analysis of a horizontal section of a glacier, zones of high pressure should correspond to super-elevated zones. The actual topography will in addition be determined by a number of other factors such as differential ablation, deviations from plane strain due to vertical extension/compression and flow induced by the presence of the topography itself. Collins suggested that the dynamics of a confluence would introduce some surface modifications that would then be counteracted by the onset of "secondary flow", *i.e.* a small amount of circulating flow superimposed on the main flow. For a Y-shape junction this would be expressed in a downward flow component at the central part of the confluence area and in an upward flow component close to the outer walls of the confluence area. Surface strain-rate measurements on Kaskawulsh Glacier showed the medial moraine to be characterized by dominant transverse compression and somewhat smaller concomitant longitudinal extension indicating a vertical extension as mentioned above. Close to the outer margins vertical compression was measured (Anderton, 1970). This is in general agreement with Collins' findings, but cannot be considered to be a strong test of the applicability of his results since no information on the strain-rate variation with depth was available.

Chapter 3

Field Observations

In this chapter a short summary of former field observations (*cf.* Sec. 3.2) and a detailed description of field experiments done as a part of this project (*cf.* Sec. 3.3) are given. Experiments done and results obtained during the bore-campaign are presented and discussed in Sec. 3.3.2; further results regarding surface strain rates and velocity field are given in Sections 3.3.3 and 3.3.4.

3.1 Setting

The Finsteraar and Lauteraarglacier are the two tributaries of the Unteraarglacier. They are both about 1 km wide and have similar surface velocities. Where they flow together they form an angle of roughly 100 degrees. The Unteraarglacier, which extends about 6 km eastwards from the confluence of the Lauteraar and the Finsteraarglacier, has a mean width of 1 km and a mean slope of approximately 4°. The confluence itself has an area of about 2 km^2 and is 2400 m.a.s.l. No mass balance measurements are available that can give information on the position of the mean equilibrium line. Based on comparison with other glaciers in the area and on an analysis of aerial photographs the mean equilibrium-line altitude is presumably somewhere around 2800 m.a.s.l. so that the area of study is with certainty wholly within the ablation area. Even yearly fluctuations are not expected to cause any part of the confluence to lie within the accumulation zone. All three glaciers are temperate.

A conspicuous feature of the Unteraarglacier is the large ice-cored medial moraine formed by the side moraines of the Lauteraar and Finsteraarglacier. It is overlain with a surfacial rock detritus of typically 5 to 15 cm thickness. Within the area of the confluence the medial moraine is 10 to 18 m high and 150 m wide, becoming higher and wider as it flows downwards to obtain a maximum height of 25 m and width of approximately 300 m, following which it starts to spread out gradually and finally merges with the marginal morainic debris. The Finsteraarglacier is fed by a group of tributaries, as a result of which a number of smaller medial moraines can be found at the south side of the confluence. These moraines also grow in height in down-glacier direction, reach points of maximum elevation and then decline. There are no tributaries that feed large amounts of ice to the Lauteraarglacier, which explains why the north part of the confluence (consisting of ice from the Lauteraarglacier) is almost debris-free.

Deep-reaching crevasses are only found close to the south-east edge of the confluence and at the north side of Unteraarglacier facing the Lauteraar hut. Within 300 m of the junction point (J) the medial moraine is cut by a small number of wide crevasses lying perpendicular to the direction of flow, which do not extent into the ice below.[1]

3.2 Former studies of the Unteraarglacier

The Unteraarglacier is one of the most comprehensively studied glaciers in the Alps. The beginning of quantitative glaciological measurements of the Unteraarglacier can be traced back to the works of Franz Josef Hugi in 1827 and of Louis Agassiz in 1841-46 (Hugi, 1830; Hugi, 1842; Agassiz, 1847). Since 1924 systematic measurements of surface changes and velocities have been made each year (Flotron, 1924 to date).

3.2.1 Flow behavior

The flow behavior of the Unteraarglacier is known in some detail since 1845 (Haefeli, 1970). In 1845-46 velocities along two profiles were measured every month by Agassiz and his coworkers. One of the profiles was close to the confluence. Both profiles showed large seasonal velocity fluctuations, with maximum velocities occurring in the period from the middle of April until the end of June, and minimum velocities from the end of October until the middle of January. The maximum velocities were about 1.6 times larger than the mean velocities. In January 1846 the velocity increased significantly and declined again in February of the same year. Similar increase of surface velocity during the winter is known in happen to some other glaciers in the Swiss Alps and elsewhere (*e.g.* Hodge (1974)). The Findelnglacier, for example, shows an continuous increase in surface velocity during the whole winter, starting in September and ending in May. The late summer is a period where the surface velocities are below the yearly average (Iken, private communications). The buildup of water pressure is not only a function of melt-water runoff but also of the potential sub-glacial drainage. If the sub-glacial drainage system collapses at the end of the melting season when the water pressure drops down to approximately zero, it can take a long time of gradual water pressure buildup until new sub-glacial channels form. The measurements of Agassiz and the data from Findelnglacier can be understood if one assumes that it may take a larger water pressure to create an effective sub-glacial drainage system than to maintain one.[2]

From 1969 until 1980 the ice movements some 2 km below the confluence (close to the Pavillon Dollfuss hut) were studied by means of an automatic camera (Flotron, 1973). Again large seasonal velocity variations were found, with high velocities during summer. The mean summer velocities varied from year to year, but the winter velocities hardly changed during each winter over this period, in contrast to Agassiz findings. An observed increase in mean annual velocities, that can sometimes

---

[1] A detailed inspection of aerial photographs, however, showed one of the wide transverse crevasses to continue into the adjoining ice.

[2] There are of course other possibilities of explaining this behavior. The continuous sliding of the Findelnglacier possibly destroys the subglacial channels faster than they are created and so causes high water pressures, that in turn are possibly to some extent responsible for the basal sliding. The pressure buildup during winter could be caused by ground water flow.

last for several years, during a decrease in surface altitude is presumable due to different amounts of sliding during summer, due to yearly fluctuation of melt-water runoff and/or changes in the sub-glacial drainage system. Over a period of three weeks in June 1975 the camera records were augmented by theodolite measurements at four transverse profiles. A number of uplift events, interpreted to be due to an increased water storage at the bed, were observed (Iken *et al.*, 1983). Since no direct measurements of basal sliding were done, the possibility that some part of the uplift is caused by a transfer of basal velocity anomalies to the surface cannot be ruled out (Iken, private communications; Balise and Raymond, 1985).

It is clear from these measurements that there can be a considerable amount of sliding during summer. A likely explanation for an annual variation of sliding velocity of the magnitude observed is a change in water pressure, and a model that attempts to simulate the summer velocities will necessarily have to incorporate some kind of a sliding law with the water pressure as a pertinent variable. It is on the other hand possible (but not proven) that there is only a negligible amount of sliding occurring during winter. This is suggested by the absence of any velocity increases during winter, indicating that the water pressure does not rise during this period of the year.

3.2.2 Bedrock

A part of the Finsteraar and Lauteraarglacier and the whole of the Unteraarglacier has been investigated by seismic reflection soundings (Knecht and Süsstrunk, 1952). These results show two different depths for the Unteraarglacier. An attempt to decide between the two seismic reflections by the use of D.C. resistivity soundings was not successful (Röthlisberger, 1967). Radio-echo soundings then showed the upper reflector to represent the true glacial bed and additional seismic soundings showed the layer between the two reflectors to consist of unconsolidated material (Sambeth and Frey, 1987b; Sambeth and Frey, 1987a; Funk and Röthlisberger, 1989; Funk, 1986; Funk, 1987a; Funk, 1987b; Funk, 1987c). In the area of the confluence only one reflector was found. From the systematic thinning of the sediment layer in the up-glacier direction and its final disappearance directly below the confluence one can infer that there is a transition from erosion at the glacial bed to sedimentation in the down-glacier direction; the beginning of the sediment layer marks the beginning of sedimentation.

For the purpose of the flow-modeling the rather complex three-dimensional geometry of the confluence was not known in sufficient detail and further radio-soundings were undertaken.

3.3 The field experiments

The purpose of the field measurements, which where made in the period from summer 1991 to winter 1993, was to obtain as detailed information as possible on the flow pattern and the geometry of the glacier bed.

Field work consisted of the following:

- Radio-echo soundings made from 8-12th of April, 1991 and again from 9-11th April, 1992.
- Field trip as preparation for bore-campaign from 17-19th of August, 1991.
- Bore campaign, from 9-18th of September, 1991
- Survey of markers and instruments readings: Oct. 30th 1991, Jan. 16th 1992, Dec. 1st 1992, and Jan. 19th 1993, as well as during the campaigns of August 1991, and April 1992.

3.3.1 Radio-echo soundings

Radio-echo soundings were made from 8-12th of April 1991, along eight profiles. An attempt to interpolate the data to obtain the bed-geometry of the confluence area showed that additional measurements were needed. From 9-11th of April 1992 five further profiles were therefore measured. The resulting bed-geometry is shown in Fig. 3.1.

The interpretation of the data obtained in 1991 was difficult because of reflections from the walls and multiple reflections from the bottom. Close to the confluence the Finsteraar and Lauteraarglacier are thicker than their half-widths. Hence, the signal with the shortest path often came from the steep walls. Even in the middle of the transverse profiles the signal did in general not come from the point of the glacier bed lying directly below. The method used to interpret the data is explained in Fabri (1991). The radio-echo soundings made in 1992 intersected the 1991 profiles at a number of points and allowed a check of the correctness of the previous results. The agreement was excellent except at the lowest profile on the Lauteraarglacier were one of the multiple reflections had been erroneously interpreted.

The most notable features of the geometry of the glacial bed as depicted in Fig. 3.1 are the two over-deepenings on the Lauteraar and the Finsteraarglaciers and the associated two riegels approximately 30 m high lying directly up-glacier of the junction. No over-deepening was found in the area of the confluence itself. There are some examples of over-deepenings that seem to be related to the junctions of glaciers, the most spectacular example most probably being the Konkordiaplatz with an over-deepening of about 400 m. However, by looking at Fig. 3.4, which shows the ice thickness at the confluence, one sees that there is a local ice-thickness maximum there, so although there is no over-deepening there is an "over-thickening".

Below the confluence the bed becomes increasingly flatter. A thorough study of aerial photographs revealed no indication of marginal sliding. Sliding is therefore expected to be limited to the deepest sections of the bed, although a definite statement on the sliding variation across the glacier has to await direct measurement of the slip velocity.

Comparison of Fig. 3.1 based on the radio-echo soundings with the results of the seismic soundings, shows a good agreement in general except for the bedrock of the

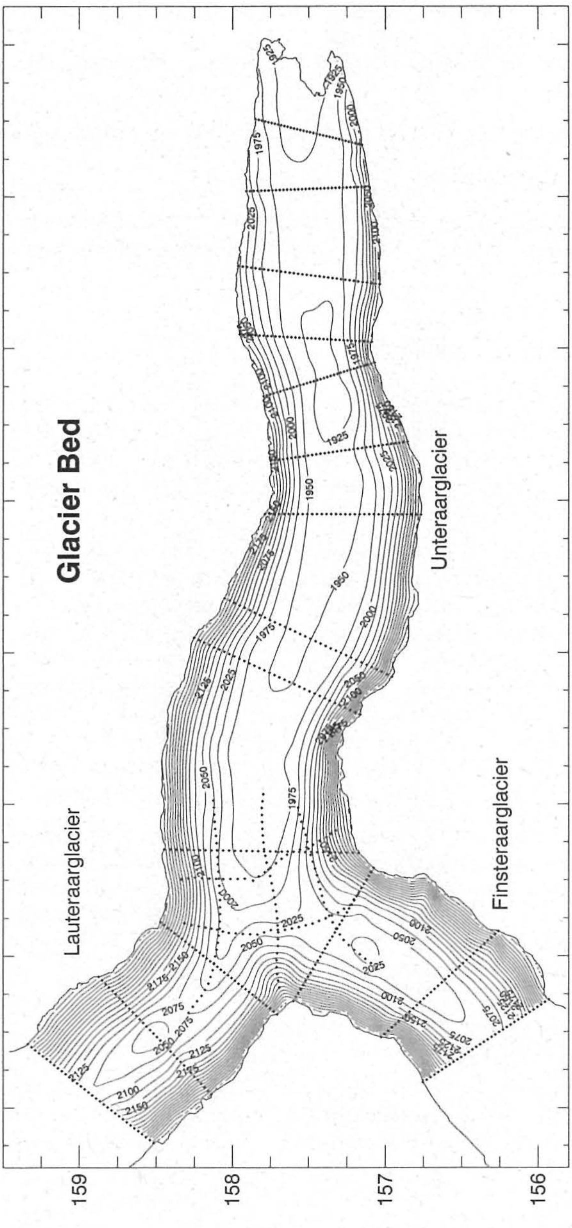

Fig. 3.1: Bedrock of the Unteraarglacier based on results from radio-echo soundings made in 1987, 1991 and 1992. The radar profiles are shown as lines consisting of points. Coordinates are in km and correspond to the official Swiss coordinate system.

confluence, where the radio-echo soundings show bedrock lying about 30 m deeper. This difference is important; if the seismic soundings give the correct result there is no over-thickening. The seismic soundings show no riegel beneath the Lauteraarglacier, but this could be a result of the low data density in that area. It is also possible that the riegel doesn't exist since only few radio-echo data points where available. The existence of the riegel beneath the Finsteraarglacier must, on the other hand, be considered to be proved since a large number of measurements where done. That riegel also shows up in the results of the seismic soundings.

This is not the first time that differences between radio-echo measurements and the seismic measurements of Knecht and Süsstrunk show up. Another such example is the lowest section of the Unteraarglacier. There the differences were so great that it was decided to do additional seismic measurements (Sambeth and Frey, 1987b; Sambeth and Frey, 1987a) that then agreed with the radio-echo findings. Knecht and Süsstrunk never explained in detail how they interpreted their data or how they dealt with the complicated three-dimensional geometry of the confluence area. It is therefore difficult to judge the accuracy of their results, and it was decided to use the results of the radio-echo soundings for modeling purposes.

The interpolation done to obtain Fig. 3.1 deserves an explanation as the same procedure was used for the generation of the bottom nodes of the FE mesh.

Only in the area of the confluence was the density of the measurements high enough such that a standard method for the interpolation of scattered data in a two-dimensional plane could be used. The method chosen calculates a continuously differentiable function, which is locally a quintic polynomial in two variables (Akima, 1978). No smoothing was done. Outside of the area of the confluence the interpolation of the data consisted of the following steps:

1. For some point $\mathbf{r}$ within the glacier the corresponding width of the glacier had to be found. To this end the distance along some straight line through that point to the border of the glacier was calculated. By varying the orientation of the line systematically the minimum distance could be found. The minimum distance so obtained was defined to be the width of the glacier at the point $\mathbf{r}$.
2. The ratio of the distance from $\mathbf{r}$ to one of the boundaries to the width at point $\mathbf{r}$ was calculated and the corresponding points lying on the two closest profiles in the up-glacier and down-glacier direction were found (which included a repetition of step 1). These points are called $\mathbf{r}^{\mathrm{up}}$ and $\mathbf{r}^{\mathrm{down}}$ respectively.
3. The glacier depth at $\mathbf{r}^{\mathrm{up}}$ and $\mathbf{r}^{\mathrm{down}}$ was found by one-dimensional cubic spline interpolation through the data-point of the radio-echo sounding profiles. The data points did not quite lie on on straight lines, so that the data had to be projected onto the best-fitting straight lines.
4. Finally the depth at $\mathbf{r}$ was defined to be the mean of the depths at $\mathbf{r}^{\mathrm{up}}$ and $\mathbf{r}^{\mathrm{down}}$, weighted by the distance from $\mathbf{r}$ to $\mathbf{r}^{\mathrm{up}}$ and $\mathbf{r}^{\mathrm{down}}$. The interpolation is therefore linear and does not produce a continuously differentiable function.

This procedure was repeated for a large number of points lying on an equally spaced grid. The grid was then used, together with a data set defining the boundary of the glacier as well as the points from the confluence, as a basis for the two-dimensional cubic spline interpolation needed for the generation of Fig. 3.1. Exactly the same computer code was used in generating the coordinates for the bottom nodes of the FE mesh. This same program can, with minor modifications, be used for a general generation of FE meshes for a valley glacier where the bed is known along a number of transversely crossing profiles, making the FE modeling of a valley glacier a matter of routine.

The surface elevation of the confluence is depicted in Fig. 3.3. The figure is based on a digital terrain model with a grid spacing of 50 m, which was kindly made available by the engineering firm Flotron AG. The medial moraine as well as a number of smaller moraines on the south part of the confluence can be seen. Close to the junction point (J) a surface depression can be seen. The cause of this depression will be discussed in Sec. 4.2. Notice that the northern part of the confluence (the transition of Lauteraarglacier to the Unteraarglacier) has a unusually high slope of about 6°.

3.3.2 Bore campaign

During the second week of September 1991 four bore holes were drilled, with a hot-water jet, at a location close to the medial moraine and about 500 m downwards from the junction point. The holes, which were only 10 to 20 m apart, had depths ranging from 100 to 281 m. The exact location of the drilling site can be seen in Fig. 3.3. During the campaign air temperatures were above freezing point and considerable surface melting occurred during the day.

To gain information on vertical strain rates, three of the bore holes were equipped with magnetic rings at depths of 100, 150 and 200 m. During the campaign the position of the magnetic rings with respect to reference sticks frozen into the glacier surface were measured several times a day. The absolute positions of the reference sticks were also measured. The results of these measurements are given below.

The magnetic rings were anchored on 1.5 m long aluminum tubes with a strong glue, and the tubes were then fixed to the walls of the bore holes.

The deepest hole, 280.6 m deep, was instrumented with four thermistors and eight one-axis electrolytic tilt sensors (Spectron L-211U). Prior to the field campaign the sensors had been installed in pairs in four metal rods. No experience had been gained beforehand in the use of these sensors. One of them went out of order shortly before the start of the campaign, leaving no time for replacement and another shortly after the installation. The two remaining sensors pairs gave confusing results which could not be interpreted.

The resistivity of the four thermistors corresponded to melting point temperatures, as expected.

For determination of surface velocities some 25 marker sticks were drilled into the ice and surveyed. At the drilling site five markers 25 m apart were used to determine

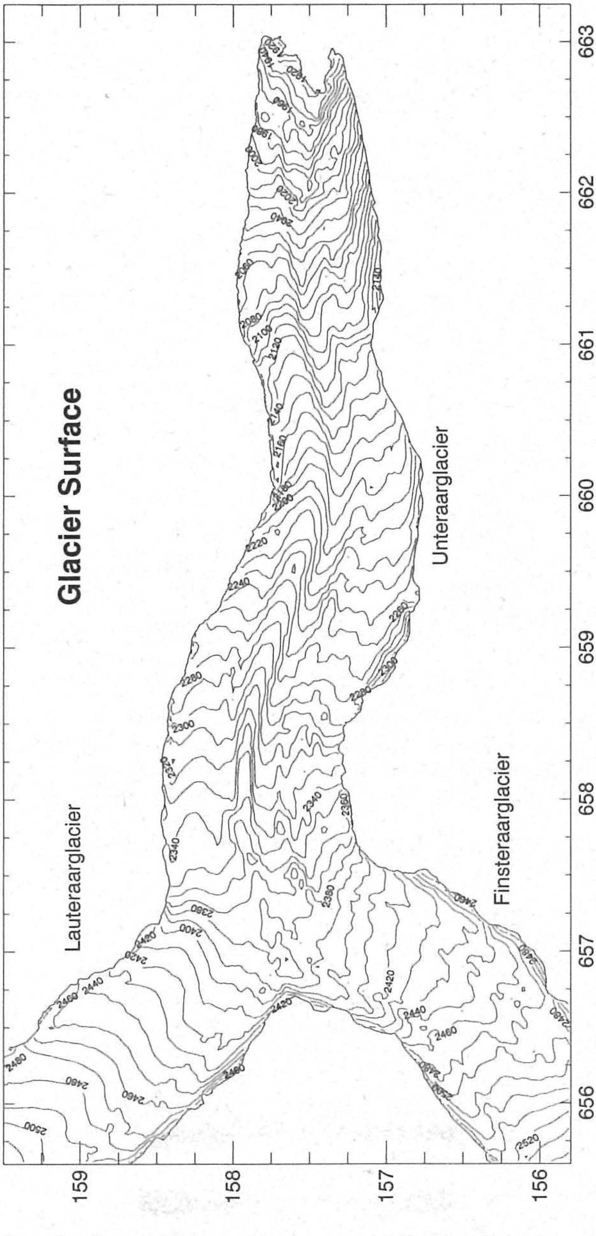

Fig. 3.2: Surface elevation of Finsteraar, Lauteraar, and Unteraarglacier in summer 1991. Based on a digital terrain model with a grid spacing of 50 m. Coordinates are in km.

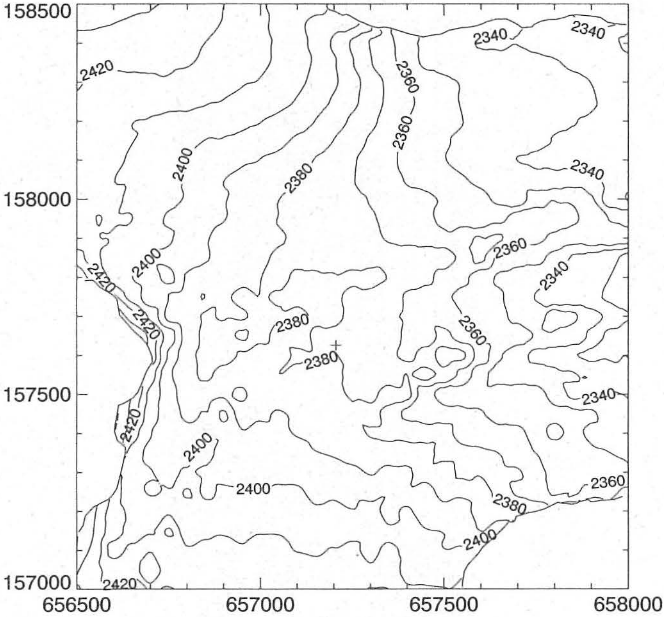

Fig. 3.3: Surface elevation of the confluence area in summer 1991. Based on a digital terrain model with a grid spacing of 50 m. North is pointed upwards. The medial moraine as well as a number of smaller moraines on the south part of the confluence can be seen. The plus symbol close to the center gives the location of the bore holes drilled in autumn 1991.

the surface strain rates. Surface strain rates are discussed in Sec. 3.3.3 and surface velocities in Sec. 3.3.4.

3.3.2.1 Vertical strain rates

The measurements of the vertical position of the three magnet rings at depths of approximately 100, 150 and 200 meters started on Sept. 14th 1991 and were done every day until the 22nd of Sept. Several weeks later or on Oct. 1st one additional measurement was made. The position measurement of the ring in the 150 m bore hole could, however, only be continued until Sept. 15th, since after that date the ring could no longer be found. The reason for this is not clear, but it is possible that the bore hole was somewhat too wide so that the ring was not situated horizontally and that the inclination of the aluminium tube, to which it was attached, changed somewhat with time making a measurement increasingly difficult. Right from the beginning was it difficult to obtain a signal from that ring. Sometimes the measurement cable would get caught in the aluminium tube and could then only be

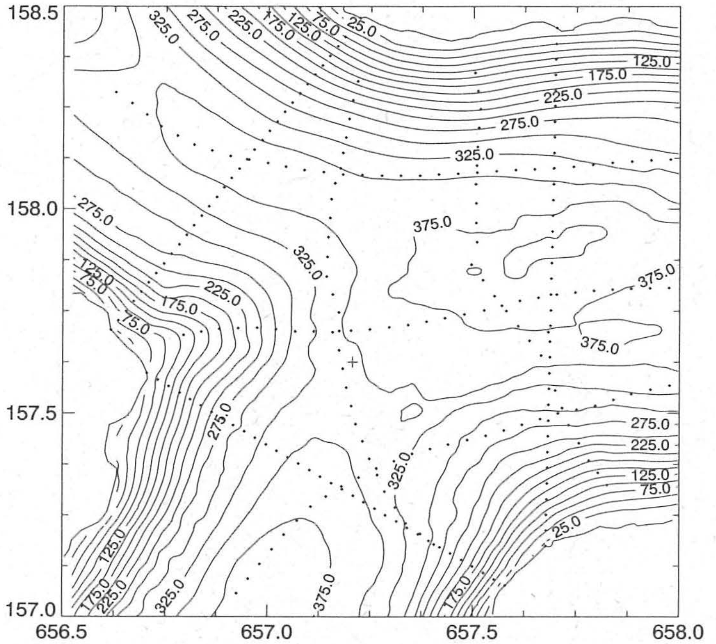

Fig. 3.4: Ice-thickness of the confluence area in summer 1991. The ice-thickness generally increases in the up-glacier direction, as is to be expected since the equilibrium line lies considerable above the area shown. Nevertheless a local ice-thickness maximum, limited to the confluence, can be seen. Based on data from radio-echo soundings. Coordinates are in km.

set free after a time consuming trial and error procedure. Since the measurement was so difficult, and because of the danger of not being able to set the cable free, measurements were discontinued on the 15th of Sept., *i.e.* the day after the ring was installed. Determination of the vertical location of the other rings posed no similar problems.

Since shear changes the length of the holes it is the total stretch above the magnetic rings which is being measured. Harrison (1975) used finite deformation theory to derive for the total strain e caused by surface-perpendicular strain rate as well as shearing the formula

$$\dot{e} \approx \dot{\epsilon}_{zz} + 2\,\dot{\epsilon}_{xz} \sin\alpha + \dot{\epsilon}_{xz}^2\, t \tag{3.1}$$

The time interval between measurements was $\approx 0.003\,a$ and $\sin\alpha \approx 0.05$. Estimates of shear strain rates based on a FE model (discussed in Chapter 5) give $\dot{\epsilon}_{xz} \approx 0.05\,\mathrm{a}^{-1}$. The contribution of shearing to bore-hole stretching is therefore less than $0.005\,\mathrm{a}^{-1}$. Values for $\dot{e}$ given below are considerably larger, so that $\dot{e} \approx \dot{\epsilon}_{zz}$. Shearing

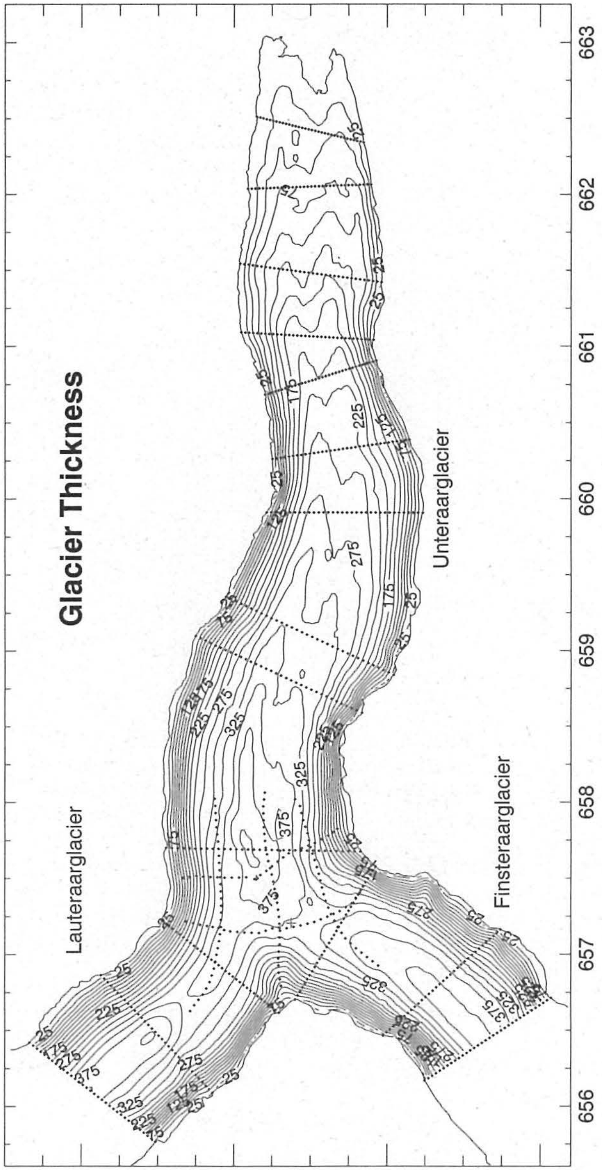

Fig. 3.5: Ice thicknesses of Finsteraar, Lauteraar, and Unteraarglacier in summer 1991. Coordinates are in km.

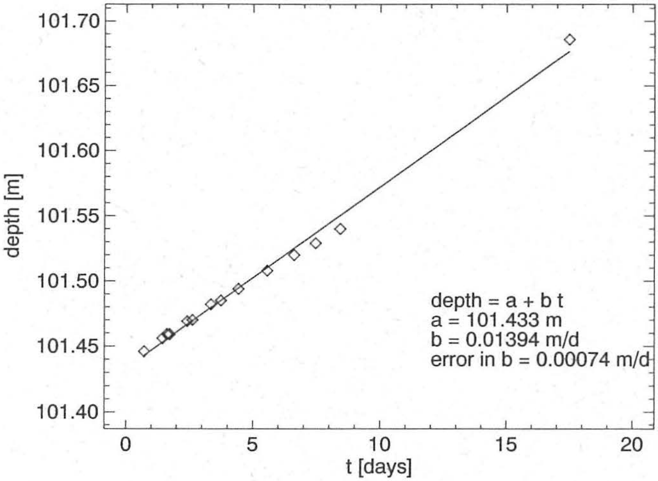

Fig. 3.6: Displacement of a magnetic ring at a depth of 100 m as a function of time. Day zero refers to Sept. 14, 1991.

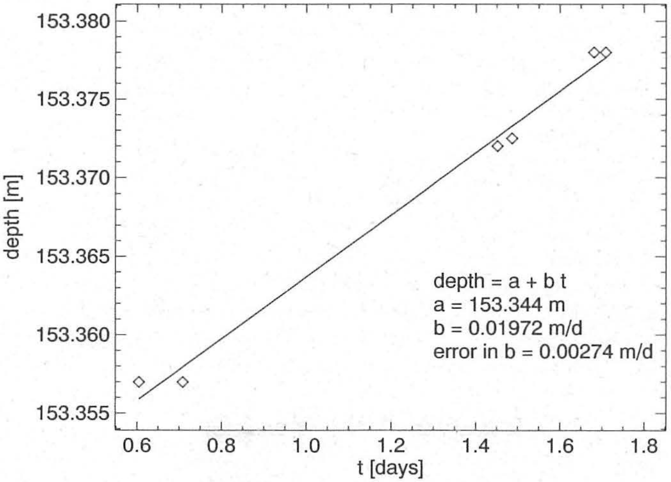

Fig. 3.7: Displacement of a magnetic ring at a depth 150 m as a function of time.

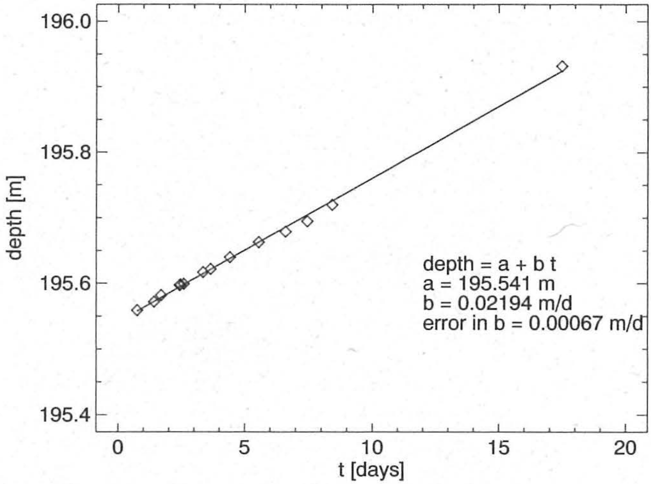

Fig. 3.8: Displacement of a magnetic ring at a depth of 200 m as a function of time.

will hence be ignored, and the change of the distance from surface reference marks to magnetic rings will be referred to as a change of vertical positions.

The vertical positions of the three rings are given in tabulated form in Tables A.1, A.2 and A.3. Vertical displacements of the rings (*cf.* Figs. 3.6 to 3.8) turned out to be surprisingly large: 1.39 ± 0.07, 1.97 ± 0.27 and 2.19 ± 0.07 cm/d for the rings in 100, 150 and 200 m holes respectively. Positive values indicate extension, *i.e.* the distance to the rings with respect to the reference sticks at the glacier surface increase with time.

The measurement done on 1. of Oct. gave depths that seem to be (*cf.* Figs. 3.6 and 3.8) somewhat greater than expected by extrapolation of the values obtained from Sept. 14th to 22nd. This could be due to increased vertical movements or a measurement error. All readings were made relative to horizontal reference bars (one for each bore hole) attached to two poles frozen into the ice. As the horizontal bars were installed care was taken to make sure that they were truly horizontal. On Oct. 1st they were, however, clearly not lying horizontally, which means that at least some of the poles to which the bars were attached had moved with respect to the ice. The errors so introduced could just as well explain the somewhat larger than expected readings.

The movement of the reference marks relative to a fixed point outside of the glacier was also measured and corresponded to a average thickening rate of 1.0 ± 0.5 cm/d. At the point of drilling the glacier is (*cf.* Fig. 3.4) about 340 m thick. The relatively high error estimate compared to the results obtained with the magnetic rings is caused by the fact that a part of the measured vertical displacement is due to vertical stretching/compression and some simply to its overall downward flow. These two

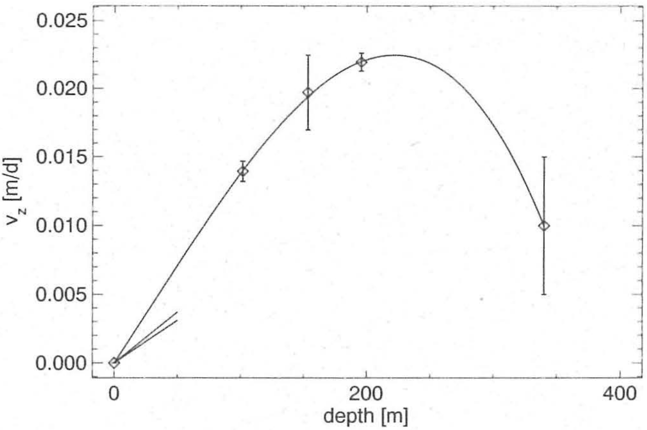

Fig. 3.9: Measured vertical velocity as a function of depth relative to the surface. The rightmost point gives the velocity at the bedrock. The curve is an interpolation of the measured velocities of magnetic rings and is only one of many possibilities of putting a curve through the data. The slope of the curve at depth zero would have to lie somewhere between the two straight lines if an agreement with vertical strain rate measurements based on horizontal movements of sticks at the surface (assuming incompressibility of ice) is to be obtained. Positive velocities denote downward movements. Velocities are relative to the glacier surface.

components can only be separated by estimating the average slope which introduces some errors. This is also the reason for choosing the glacier surface as a reference point and not some fixed point outside of the glacier.

The vertical velocity profile is depicted in Fig. 3.9. Measured values were interpolated using a third degree polynomial and with weighting factors inversely proportional to errors. The interpolating curve goes, as can be seen, nicely through the error bars. The most conspicuous feature of Fig. 3.9 is the maximum at approximately 220 m. The exact location of this maximum is somewhat uncertain as the curve is based on only five data points and the choice of the interpolating function or different weighing factors can shift it somewhat. But it is beyond any doubt that the vertical velocity increases with depth and then decreases again, causing a shift in strain rates from positive (extension) to negative (compression) somewhere between 195 and 340 m.

Vertical strain rates obtained by differentiating the interpolation curve in Fig. 3.9 are given in Fig. 3.10.

In a summary it can be said that the installments of the magnetic rings and the measurement of their vertical displacements with time could be done successfully, and that this method proved to be an easy and effective way of obtaining information on vertical strain rates. A disadvantage of the installation method used is that only one magnetic ring per bore hole can be installed. This problem should be addressed

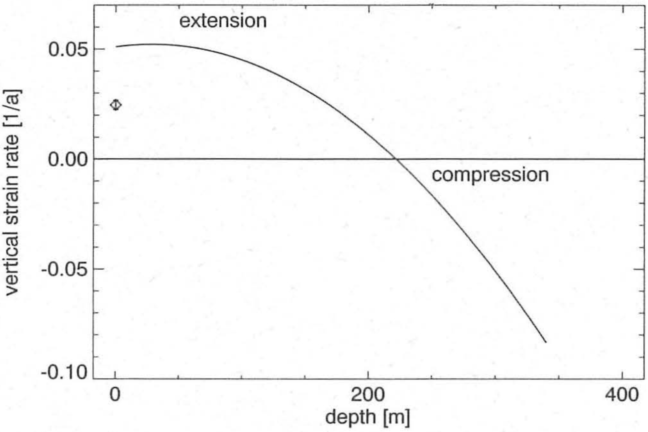

Fig. 3.10: Measured vertical strain rate as a function of depth. The curve is the slope of the curve in Fig. 3.7. The diamond symbol represents the vertical strain rate estimate based on measurements of horizontal strain rates at the surface.

in the future, perhaps using the method of measuring vertical strain using a number of markers within the same bore hole developed and successfully applied by Rogers and LaChapelle (1974). It could be shown unambiguously that at the drilling site the vertical strain-rate variation is complicated, changing from positive to negative at a depth of some 220 m. It is a challenge to a flow model to explain or reproduce this unexpected rate-of-deformation profile. This important finding is also a good example of a complicated vertical strain-rate variation. Simplifying assumptions about the vertical strain-rate variation, such as a constant vertical strain rate (Nye, 1957), of a linear variation from a finite value at the surface to a zero value at the bottom (Dansgaard and Johnsen, 1969), or vertical strain rates being proportional to horizontal velocities (Funk *et. al* 1994, in press), are often made in flow models.

3.3.3 Horizontal strain rates

The horizontal strain rate at the drilling site was determined by measuring the movements of five stakes set up as a perfect square with one stake at the center. This square pattern was suggested by Nye (1959). The distance from the center stake to the others was approximately 50 m.

The stakes were surveyed four times during the winter 1991/1992: Sept. 17 and Oct. 10, 1991, and Jan. 1 and April 4, 1992, making it possible to calculate average strain rates for three successive periods of time. Strain rates were calculated using the method suggested by Nye (1959) as well by finding the best fit of the velocity of each pole to the expression

$$v_i = \beta_{0i} + \beta_{1i}x + \beta_{2i}y \tag{3.2}$$

Method: Nye, 1959				
time period	$\dot{\epsilon}_1[a^{-1}]$	$\dot{\epsilon}_2[a^{-1}]$	ϕ	standard error
17.09.91 to 30.10.91	0.0420	-0.0663	-4.8	±0.0004
30.10.91 to 16.01.92	0.0300	-0.0475	-15.9	±0.0005
16.01.92 to 12.04.92	0.0296	-0.0435	-12.8	±0.0008

Table 3.1: Principal horizontal strain rates at the drilling site calculated from measured data by the method of Nye (1959). The angle ϕ, given in degrees, is defined as positive in a clockwise direction from north.

Multiple linear regression: $v_i = \beta_{0i} + \beta_{1i}x + \beta_{2i}y$			
time period	$\beta_{1x}[a^{-1}]$ $\beta_{1y}[a^{-1}]$	$\beta_{2x}[a^{-1}]$ $\beta_{2y}[a^{-1}]$	R_x R_y
17.09.91 to 30.10.91	0.0384	0.0269	0.997
	0.0118	-0.0630	0.97
30.10.91 to 16.01.92	0.0297	0.0163	0.99
	-0.0182	-0.0478	0.90
16.01.92 to 12.04.92	0.0288	0.0152	0.99
	-0.0097	-0.0438	0.89

Table 3.2: Regression coefficients used for the calculation of surface strain rates. R_x and R_y are the correlation coefficients.

making the calculation of the strain rates using

$$\dot{\epsilon}_{ij} = \frac{1}{2}(v_{i,j} + v_{j,i}) \tag{3.3}$$

straightforward.

The velocities were considered to refer to the mean position of each stick during the beginning and the end of each measurement time interval. The movements of the sticks during the measurement period were so small relative to the dimensions of the glacier that the effect of the velocity gradient on their apparent velocities could be ignored.

The method of Nye (1959) is based on the assumption that the stakes form a perfect square. Care was taken to set the stakes up accordingly but some deviation from that form is inevitable. With time velocity gradients, *i.e.* strain rates, cause further deviation from the form of a perfect square. This is the reason for calculating, in addition to the Nye's method, the rate of deformation using multiple linear regression.

Table 3.1 gives the principal horizontal strain rates at the drilling site calculated according to the method of Nye (1959). Regression coefficients are given in Table 3.2, the strain rate tensor (with respect to a coordinate system with the x-axis pointing west) in Table 3.3, and the principal horizontal strain rates based on linear regression

Method: Multiple linear regression			
time period	$\dot{\epsilon}_{xx}[a^{-1}]$	$\dot{\epsilon}_{yy}[a^{-1}]$	$\dot{\epsilon}_{xy}[a^{-1}]$
17.09.91 to 30.10.91	0.0384 ± 0.0015	-0.0630 ±0.0015	0.0194 ± 0.0015
30.10.91 to 16.01.92	0.0297 ± 0.0009	-0.0478 ± 0.0009	-0.00097 ± 0.0009
16.01.92 to 12.04.92	0.0288 ± 0.0008	-0.0438 ± 0.0008	0.0028 ± 0.0008

Table 3.3: Measured strain rates found by multiple linear regression. Errors are based on estimated surveying errors.

Method: Multiple linear regression				
time period	$\dot{\epsilon}_1[a^{-1}]$	$\dot{\epsilon}_2[a^{-1}]$	ϕ	$\dot{\epsilon}_3[a^{-1}]$
17.09.91 to 30.10.91	0.0419 ± 0.0015	-0.0665 ± 0.0015	10.5 ± 2.4	0.0246 ± 0.0021
30.10.91 to 16.01.92	0.0298 ± 0.0009	-0.0478 ± 0.0009	-0.7 ± 2.1	0.0180 ± 0.0013
16.01.92 to 12.04.92	0.0289 ± 0.0008	-0.0439 ± 0.0008	2.2 ± 2.1	0.0150 ± 0.0011

Table 3.4: Measured principal horizontal strain rates at the drilling site calculated using linear regression. ϕ is the angle in degrees from the x-Axis (pointing west) in anti-clockwise direction to $\dot{\epsilon}_1$. The vertical strain rate $\dot{\epsilon}_3$ was calculated by assuming $\dot{\epsilon}_{ii} = 0$, which is justified by the incompressibility of ice and the absence of crevasses close to the drilling site. Extension is positive, compression negative.

coefficients in Table 3.4. Comparison of Table 3.1 with Table 3.4 shows almost perfect agreement between $\dot{\epsilon}_1$ and $\dot{\epsilon}_2$ calculated with the two methods, but a small difference in the value of the rotation angle ϕ, which is presumably due to the square distortion that is neglected in Nye's method.

During the time period from the 17th of Sept. 1991 to the 30th of Oct. 1991 the rate of deformation was considerably larger than during the two subsequent time periods (see for example Table 3.4). This is a clear indication of a seasonal strain-rate variation that, because of a lack of change in thickness or surface slope, can most easily be explained as a consequence of a temporal change in basal sliding velocity. Considerable surface melting did take place during September and possibly the first week of October. On the 30th of October no melting occurred and the glacier was covered with fresh snow. This presumably led to a drop in water pressure and a consequent decrease in sliding velocity. It is important to notice that no further strain-rate variations were observed during the winter. The velocities of the markers (discussed in Sec. 3.3.4.3) also remained stable. Hence, from November sliding velocities were stable and possibly zero. No marginal sliding was observed during summer or winter showing that sliding variations are confined to the lower sections of the glacier bed. Such non-uniform sliding across a glacier cross-section is known to occur at other glaciers as well, the Athabasca Glacier being the best known example (Raymond, 1971).

The orientation of the principal compressive strain rates is approximately N-S (*cf.* Fig. 3.13), and they exceed the concomitant E-W extension.

Assuming incompressibility of ice, and since there were no crevasses close to the drilling site, the vertical surface strain rate $\dot{\epsilon}_3^s$ can be calculated (*cf.* Fig. 3.4) and compared with the vertical strain-rate measurements using magnetic rings. This is done in Fig. 3.10 where $\dot{\epsilon}_3^s$ is depicted as a diamond symbol. The vertical strain-rate curve (based on vertical movements of the magnetic rings) does, as can be seen, not go through the error bars. There is, however, no reason to infer that the two methods give incompatible values for $\dot{\epsilon}_3^s$, since a relatively small change in the slope of the velocity-depth curve in Fig. 3.9, that cannot be excluded using available measurements, would bring them into agreement. This is indicated in Fig. 3.9, with the help of two short straight lines, that give the range within which the slope of the curve would have to lie in order to produce a vertical surface strain rate in accordance with marker measurements.

3.3.4 Surface velocities and strain-rate pattern

Aerial photographs are taken of the Aareglacier[3] late summer every year. By direct comparison of these photographs the surface velocity field can be constructed (Flotron, 1973; Flotron, 1979).

3.3.4.1 Annual velocities

Direct comparison of aerial photographs taken on the 15th of August 1989 and on the 20th of August 1990, kindly made available by A. Flotron, Meiringen, was done by W. Schmid at VAW-ETHZ. The results can be seen in Fig. 3.11.

There is a number of missing data points in Fig. 3.11 where surface features had changed to such an extent during the time elapsed that it was impossible to find an optimal matching. Still, the overall annual flow pattern becomes quite clear. Maximal annual velocities are about 45 m/a, the maximum being reached close to the center of the confluence area where the ice thickness is greatest (*cf.* Fig. 3.4). Velocities in the up-glacier direction towards Finsteraarglacier are larger than those of Lauteraarglacier, which is also in general accordance with thickness differences. It is, however, questionable to put much emphasis on the interpretation of annual velocities of a glacier known to show large temporal variations in sliding velocity, and hence in surface velocity. Since the boundary conditions change throughout the year (and the surface velocity with them) the average annual velocity field may, and in general will, never obtain for any period of time. The annual velocity therefore reflects the sum of different physical processes realized at different times, but the sum itself may not correspond to any physical reality.

3.3.4.2 Summer velocities

Since the Unteraarglacier shows seasonal velocity variations annual velocities are of limited value, and it was decided to use the method of direct comparison of aerial photographs to get information on the summer velocities. To this end a flight

---

[3] Aareglacier is a collective name for the Finsteraar, Lauteraar, Unteraar and Oberaarglacier.

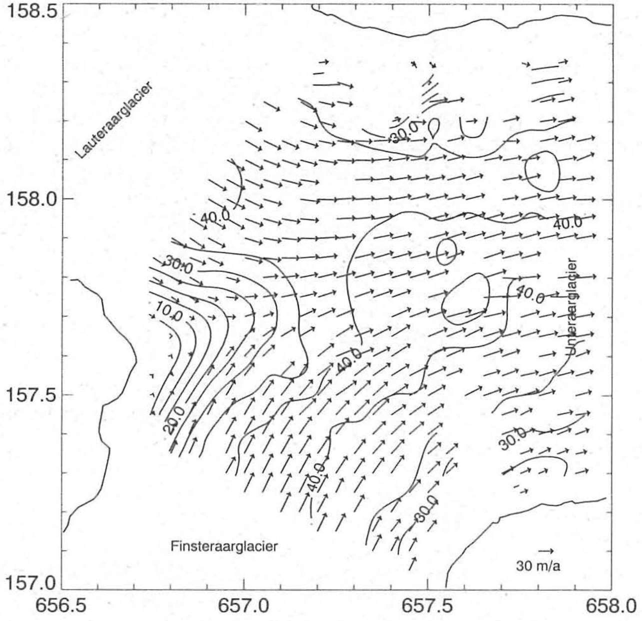

Fig. 3.11: Annual velocities in m/a based on comparison of aerial photographs taken on the 15th of August 1989 and on the 20th of August 1990. Contour interval is 5 m/a. Coordinates are in km. North points upwards.

additional to the yearly flight in August was made on the 23th of July 1991 by the Swiss Federal Institute of Topography[4]. The resulting aerial photographs together with photographs taken on the 22nd of August were evaluated by W. Schmid at VAW-ETHZ, and the resulting velocities can be seen in Fig. 3.12. Although summer velocities of the Unteraarglacier are known to vary on time scales of days and weeks (Iken *et al.*, 1983) these velocities will be called *summer velocities* hereafter.

No post-correction was made to the velocities vectors obtained with the method of direct comparison although some of them are clearly wrong, and Fig. 3.12 therefore gives an indication of the quality of the data acquired with this method. However, some smoothing was done to the horizontal speed variation, which in the figure is represented by contour lines. There are fewer missing data points in Fig. 3.12 than in Fig. 3.11 because of smaller ice displacement and less change of surface features due to melting, displacement of stones, *etc.* , that made it easier to find optimal matching between photographs.

The maximum summer velocities of the confluence area are approximately 55 m/a.

---

[4] Bundesamt für Landestopographie, Wabern — Bern

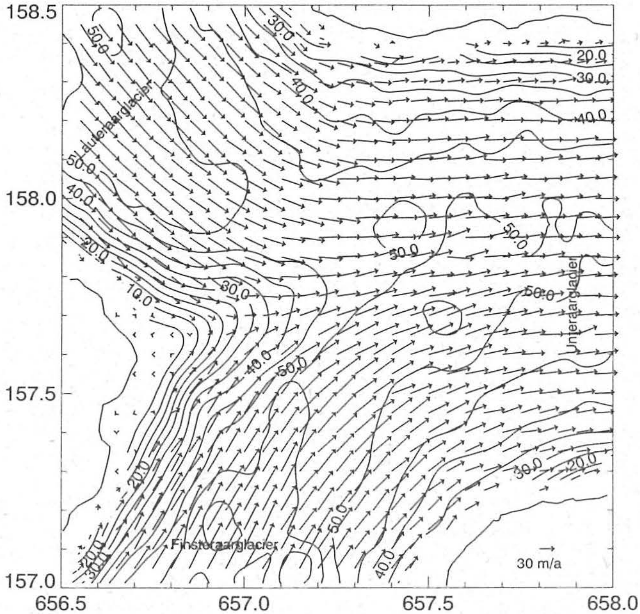

Fig. 3.12: Velocities in m/a based on direct comparison of aerial photographs taken on the 23th of July 1991 and on the 22th of August 1991. Note the high velocity gradients at the north and the south side compared to the much lower gradients along the centerline. Close to the junction point the flow field reverses its direction and flows in the opposite direction to the main flow. This is a reaction to the surface altitude gradients associated with a strong local surface depression that lies in the vicinity of the junction point. The contour interval is 5 m/a. Coordinates are in km. North points upwards.

In the up-glacier direction towards the Lauteraarglacier the velocities decrease and increase again further up-stream. On the Finsteraar side the velocities are larger than on the opposite side. On the west side of the confluence, close to the junction point, an extended area of large velocity gradients can be seen. On the north and south margins velocities are suspiciously high indicating some marginal sliding. These areas also have high numbers of crevasses that are possibly mainly active during the summer time (H. Röthlisberger, private communication).

3.3.4.3 Winter velocities

During the winter snow cover renders the surface more or less featureless making the method of direct comparison inapplicable for the determination of surface velocities. Markers had to be used for this purpose. Altogether 78 markers were installed, of which 25 were installed during the bore-campaign in autumn 1991. These were repetitively surveyed on the 30th of Oct. 1991, the 16th of Jan. 1992 and the 17-19th of April 1992. Additional markers were installed during the radio-echo sounding campaign of April 1992 and measured for about three days. Markers were reinstalled in autumn 1992 and measured on the 1st of Des. 1992, and the 19th of Jan. 1993. Velocities and positions of the markers are listed in Appendix A.

Repeated surveying showed surface velocities to be stable from the end of October 1991 until April 1992. The velocities of winter 1992/1993 were the same as those of winter 1991/1992. This, together with the observation in January 1992 that water levels in bore holes had fallen at least 200 m below the surface, is an indication of the absence basal sliding caused by subglacial water pressure.

Fig. 3.13 depicts marker velocities during the winters 1991/1992 and 1992/1993. Several additional markers, outside the confluence area, are not shown. Interpolation was done with the Akima interpolation algorithm (Akima, 1978). Extrapolation of marker velocities toward the glacier borders are uncertain, and depends to some extent on the assumption that there was no marginal sliding during the winters. Interpolation of velocities within the confluence area does not depend on this assumption.

Because of largely reduced, or even totally absent sliding, winter velocities are only approximately 60% of summer values. But there is also a qualitative difference that can be seen by comparing Fig. 3.13 with Fig. 3.12. There is a clear velocity maximum close to the confluence center that does not show up to the same extent in the summer velocities. Relative velocity gradients are also larger during summer than winter, as can be seen from Fig. 3.14, where summer and winter velocities normalized by respect to maximum velocities are displayed. This is a nice example of a seasonal variation of the deformation profile across a glacier and shows, together with the temporal change in surface strain rates (*cf.* Sec. 3.3.3), that sliding affects the internal deformation pattern. This may be especially important for a confluence where a relatively large contact area between the ice and the bedrock, along which sliding can be effective, transforms at the junction point into a ice-ice contact area, with no or negligible relative slip motion. It is also clear that the three-dimensional geometry of the confluence makes a simple plug-flow velocity field impossible.

3.3.4.4 Surface rate of deformation

The high quality of the measured summer velocity field makes it possible to use it to calculate surface strain rates. Since velocities were determined on a 50 × 50 m equidistant and orthogonal grid, the method of Nye (1959) could be used to calculate strain rates. Use of that method also gives a convenient measure of errors involved, since $\Delta_{\dot{\epsilon}}$ defined by

$$\Delta_{\dot{\epsilon}} = \dot{\epsilon}_0 + \dot{\epsilon}_{90} - \dot{\epsilon}_{135} - \dot{\epsilon}_{45} \tag{3.4}$$

should theoretically be zero, where subscripts denote angles with respect to West.

Fig. 3.15 displays the surface summer strain-rate field obtained in this way. Strain rates with $\Delta_{\dot{\epsilon}} > 0.0007\,\mathrm{a}^{-1}$ were ignored. Vertical strain rates calculated by assum-

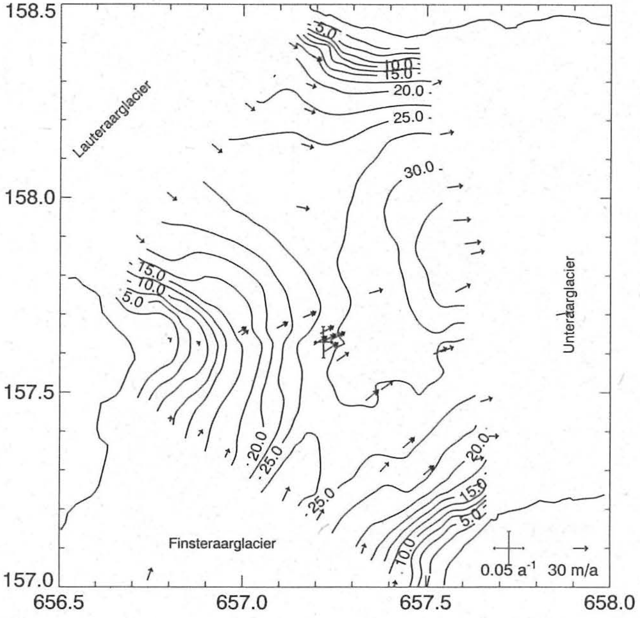

Fig. 3.13: Velocities and principal strain rates calculated from marker movements during the winters 1991/1992 and 1992/1993. Vectors denote horizontal velocities, contour lines speed. Contour interval is 2.5 m/a. Coordinates are in km. North points upwards.

ing no change of ice volume are shown as contour lines with negative contour as dotted lines and positive levels as solid lines.

Toward the glacier margins principal strain rates consistently make angles of about 45° with the flow direction. In the central zones above and below the confluence principal compressive stresses generally lie parallel and principal extending strain rates transverse to the flow direction, but there is a number of exceptions to this, some of which are presumably due to instrumental errors. It is difficult to estimate the errors involved. $\Delta_{\dot\epsilon}$ is only a measure of the residuals that result from solving four equations with three unknown variables and gives no information on systematic errors. It can, however, be concluded that except for the confluence area the rate-of-deformation pattern is consistent with a compressive flow regime, which is for an ablation area the expected state of flow (Nye, 1952). Along the center of the confluence, on the other hand, the flow is strongly extending. Along the medial moraine principal extending strain rates are parallel and the principal compressive strain rates transverse to the flow. The transverse compression outweighs the longitudinal extension, causing considerable vertical stretching. These findings are in agreement with measurements of bore-hole stretching (*cf.* Sec. 3.3.2.1) and marker movements

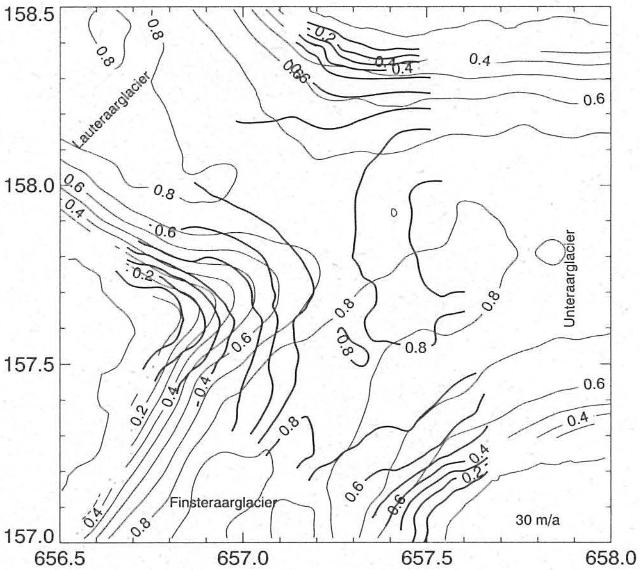

Fig. 3.14: Comparison of summer and winter velocities. Each velocity field was normalized by the maximum velocity. Thick contour lines represent winter velocities, and thin contour lines summer velocities. The contour interval is 0.2. Coordinates are in km. North points upward.

(*cf.* Sec. 3.3.3). There is also a striking qualitative agreement with measurements done on the confluence of the north and the central arms of the Kaskawulsh Glacier (*cf.* Sec. 2.1).

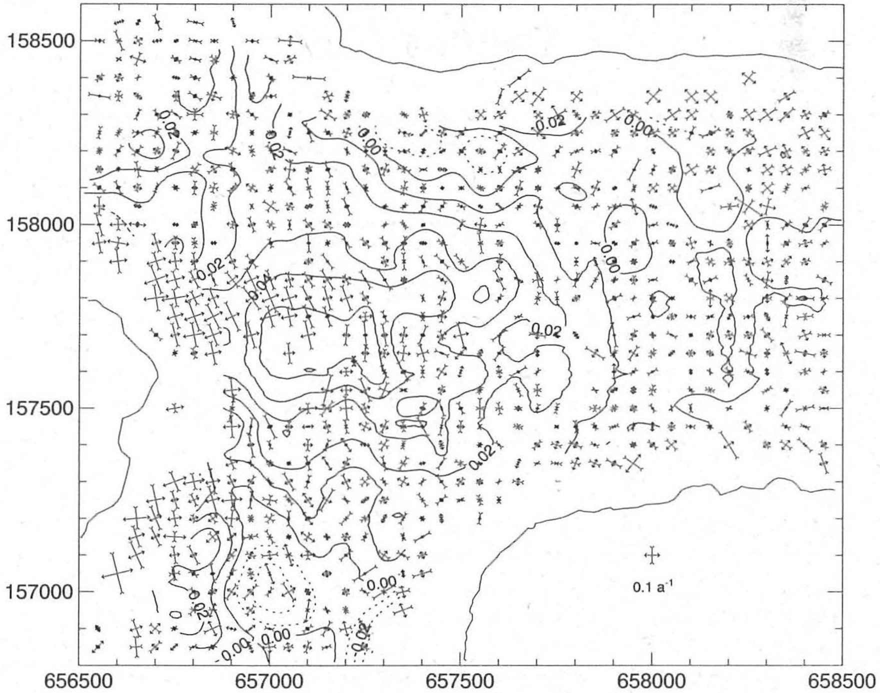

Fig. 3.15: Surface strain rates based on direct comparison of aerial photographs taken on the 23th of July 1991 and on the 22nd of August 1991. Vectors denote the two principal horizontal strain rates $\dot{\epsilon}_1$ and $\dot{\epsilon}_2$. Contour lines represent vertical strain rates calculated according to $\dot{\epsilon}_{ii} = 0$. Negative contours are drawn with dotted lines, and positive levels with solid lines. The contour interval is $0.2\,\mathrm{a}^{-1}$. Coordinates are in meters.

CHAPTER 4

General Flow Characteristics of a Confluence

The purpose of this chapter is to elucidate the observed strain-rate regime of the confluence area of the Unteraarglacier with the help of simple conceptual models, and to determine the flow characteristics of a confluence that are universal and not restricted to one particular case only.

Field measurements have shown that the uppermost section of the confluence of the Finsteraar and Lauteraarglacier is, along the centerline, subjected to large longitudinal extension, transversal compression and vertical extension. Vertical strain rates increase with depth, decrease again and become negative (compressive) for approximately the lower-most one-third part of the glacier thickness. This strong variation of the vertical strain rate with depth and its sign reversal is particularly interesting since it has often been assumed that strain rates do not vary with depth or that the variation is linear with zero strain rate at the bed-rock interface (*e.g.* Paterson (1981)).

Practically identical findings with respect to surface strain-rate pattern have been made on the Kaskawulsh Glacier showing that this kind of strain-rate regime is not limited to the confluence of the Unteraarglacier.

The main features of the surface strain-rate regime can easily be explained. Along the centerline[1] the velocity increases as the ice moves from the junction point toward the center of the confluence. Hence, the medial moraine will be subjected to longitudinal extension. The transversal compression can be seen as a result of this longitudinal extension, but also and presumably more importantly, as a consequence of the change in mean flow direction of the two converging arms within the confluence area. As for the vertical dimension, vertical strain rates integrated over depth must be positive below the medial moraine as long as ice thickness increases in the flow direction. This will in general be true for the distance from the junction point to the confluence center. Since longitudinal and vertical strain rates are positive it follows from the incompressibility of ice that the transverse compression will dominate the longitudinal extension in order to compensate for the vertical extension.

This suggests that the overall strain-rate regime in a confluence can be understood in terms of three different mechanism 1) the apparent ice thickening along the medial moraine from the junction point toward the center, 2) the change in the mean flow direction of the two converging arms within the confluence, and 3) the velocity

---

[1] The centerline is considered to be coincident with the medial moraine.

increase along the medial moraine from the junction point (J) toward the confluence center.

To gain a somewhat better understanding of the flow characteristics, two simple conceptual models will be introduced that focus on the first and the third mechanisms listed above. The first one (discussed in Sec. 4.1) is a flow-line model of a vertical section close to the medial moraine and is used to understand the vertical strain-rate variation with depth. The second one (discussed in Sec. 4.2) is a map-plane model and is used to elucidate the strain-rate pattern caused by the increase in horizontal velocity along the medial moraine.

4.1 Flow-line model

Thickness along a flow-line close to the margin, up-stream from the confluence, will increase as the marginal ice enters the confluence area, with the apparent thickness change depending on the exact bed-rock geometry and the flow-line path. As a consequence a column of ice will experience a net vertical extension, and vertical strain rates will on average be positive. Interestingly, however, depending on the boundary conditions, strain rates can become negative for the region immediately above the bed-rock interface. This can be seen by considering flow over a sinusoidal bed for two different boundary conditions: perfect sliding (*i.e.* perfectly lubricated bed), and no sliding.

The general purpose FE program MARC was used to calculate the flow of a highly viscous material over a sinusoidal bed. Glen's flow law was used, *i.e.*

$$\dot{\epsilon}_{ij} = A \, {\sigma'_{II}}^{(n-1)/2} \sigma'_{ij} \tag{4.1}$$

where $\dot{\epsilon}_{ij}$ are strain rates, σ'_{ij} deviatoric stresses,

$$\sigma'_{ij} := \sigma_{ij} - \frac{1}{3}\delta_{ij}\sigma_{kk} \tag{4.2}$$

σ'_{II} the second invariant of the deviatoric stress tensor

$$\sigma'_{II} := \frac{1}{2}\sigma'_{ij}\sigma'_{ij} \tag{4.3}$$

and δ_{ij} is the Kronecker delta.

Mesh generation, testing of the FE program MARC and estimates of numerical errors have been discussed and given by (Gudmundsson, 1994b), where a detailed analysis of the flow over a perfectly lubricated bed has also been given.

Fig. 4.1 shows vertical velocities over a perfectly lubricated bed. The x axis is parallel and the z axis perpendicular to the mean flow direction as well as to the surface. The surface makes an angle α to the horizontal. The bed, as a function of x, is denoted by $z_0(x)$ and is given by

$$z_0(x) = a \sin kx, \tag{4.4}$$

where a is the amplitude and k the wavenumber.

Only a part of the FE mesh, which had a height and a width of ten times the wavelength λ, is shown. Notice that close to the bed there is, over a part of the figure, one additional level of mesh refining. This destroys the symmetry of the mesh. Theoretically all calculated quantities should have some simple symmetrical properties with respect to a line running parallel to the y axis and through the point $kx = 3\pi/2$ (the deepest section of the bed). A systematic deviation from this symmetrical pattern must result from the asymmetrical mesh and such a deviation therefore gives an estimate of the discretization errors involved.

For $ak \ll 1$ the second order solution for a flow over a sinusoidal bed given by (Gudmundsson, 1994b) shows that $\partial(v_z)/\partial z = 0$ for $z = 0$ and $kx = 0, \pi$, *i.e.* the maximum vertical velocities are found at the bed at the points of maximum slope. The maximum of the vertical strain rates is, however, situated at $kz = 1$ (ignoring second order terms). $\dot{\epsilon}_{zz}$ is therefore positive throughout the glacier where it gets thicker and everywhere negative where it gets thinner.

The numerically calculated vertical velocity field, seen in Fig. 4.1, exemplifies this behavior. As can be seen in Fig. 4.2, depicting vertical strain rates for the same model as in Fig. 4.1, $|\dot{\epsilon}_{zz}|$ has two maxima, situated somewhat above the bed and close to the points of maximum slope.

This situation is quite different to the one which results from a no-slip type boundary condition, as can be seen by considering Fig. 4.3, which shows vertical velocities for the no-slip situation. Except for this difference in boundary condition all parameters are the same as in Fig. 4.1. The main difference to the perfectly-sliding case is that maximum vertical velocities are now not found at $z = z_0$ but somewhat above the bed.

The gentle spatial variation of the bed line introduces a perturbation on the flow which rapidly decays with height. It is the ice directly above the bed and not the surface that reacts to the thickness changes.[2] At the bed-line, however, vertical movements are suppressed and the maximum of the velocity perturbation therefore moves upwards.

This has a profound effect on the strain-rate variation with depth (Fig. 4.4). Where the glacier thickness increases in flow direction, vertical strain rates are now negative directly above the bed, although they are, if averaged over the whole glacier thickness, positive. Where the glacier gets thinner in flow direction the situation reverses. What is causing this effect is the no-slip boundary condition, together with the varying glacier thickness. The exact bed geometry is only expected to change the amplitude of the velocity variations and their extent, but a difference between bed slope and the direction of surface velocities, together with the no-slip condition, will suffice to create them.

No systematic study was done on how the position of the maximum of v_z (Fig. 4.3) depends on changes in roughness or material properties. A few calculations with different values of n and ak, however, showed that the maximum moves towards the

---

[2] This will in general only be true if $\lambda/h \ll 1$.

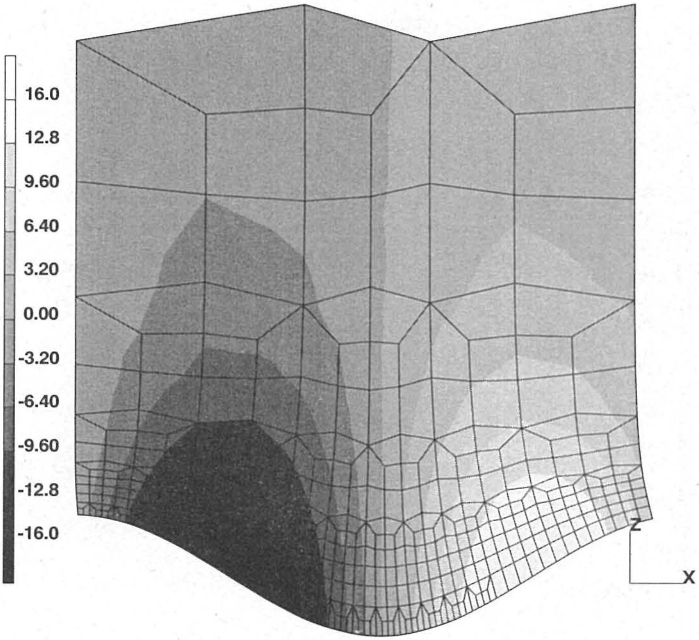

Fig. 4.1: Vertical velocities above a perfectly lubricated sinusoidal bed. Parameters: $a = 2$ m, $\lambda = 20$ m, $h = 200$ m, $n = 3$, and $\rho g \sin\alpha = 8.99577 \times 10^{-3}$ bar/m. Velocities are in m/a. Only a part of the FE mesh is shown. Flow direction is from left to right.

bed with increasing n and ak. For $ak \ll 1$ it is situated at $kz = 1$ (Gudmundsson, 1994a)

The no-slip boundary condition, together with increasing ice thicknesses in the flow direction, gives rise to a vertical strain-rate pattern, that is qualitatively the same as that measured on the Unteraarglacier. There $\dot\epsilon_{zz}$ was positive at the surface, increased with depth and then changed from positive values to negative ones close to the bed. Since the actual flow field is expected to vary in all three spatial directions, there will inevitably be some deviations from the plain-strain-rate situation, causing some additional complications that cannot be fully addressed with this simple conceptual 2D-model. For a quantitative comparison a full 3D-model is needed. Still, this simple 2D-model gives a plausible explanation of the sign reversal of $\dot\epsilon_{zz}$ at a depth of ca. 220 m. It also clarifies the effect that changes in ice thicknesses have on vertical strain-rate variations, which is helpful in identifying the causes of unex-

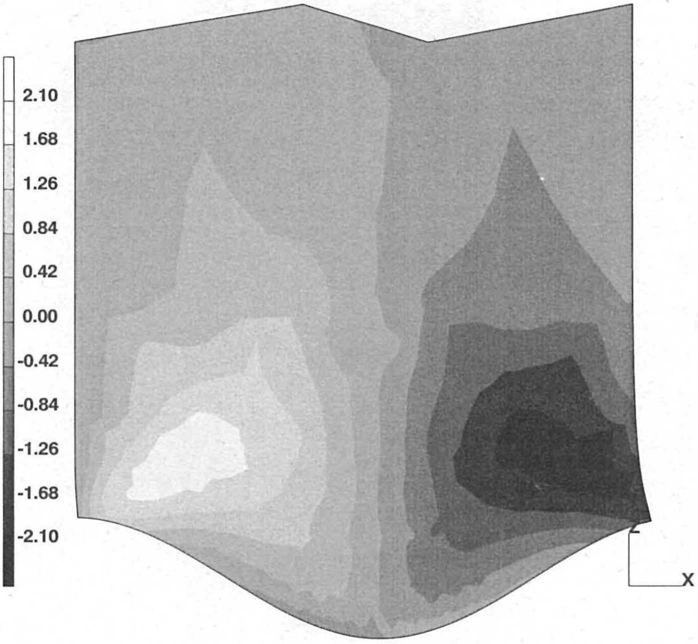

Fig. 4.2: Vertical strain rates ($2\dot{\epsilon}_{zz}$) above a perfectly lubricated sinusoidal bed. Parameters: $a = 2$ m, $\lambda = 20$ m, $h = 200$ m, $n = 3$, and $\rho g \sin\alpha = 8.99577 \times 10^{-3}$ bar/m. Strain rates are in a^{-1}.

pected flow perturbations seen in more complicated models. This also suggests that during the measurement period (second half of September 1991) the bed conditions were closer to being of the no-slip type than of the perfect-sliding type, although velocity variations show that some sliding did take place.

4.2 An idealized two-dimensional map-plane model

Marginal ice entering a confluence experiences an acceleration as it passes the junction point (J). There is also a change in boundary conditions. At the margin, boundary conditions are of the no-slip type (assuming negligible marginal sliding). In the special case of a symmetrical confluence no shear will act on the medial line and, if we further assume infinite glacier thickness, one could theoretically put a

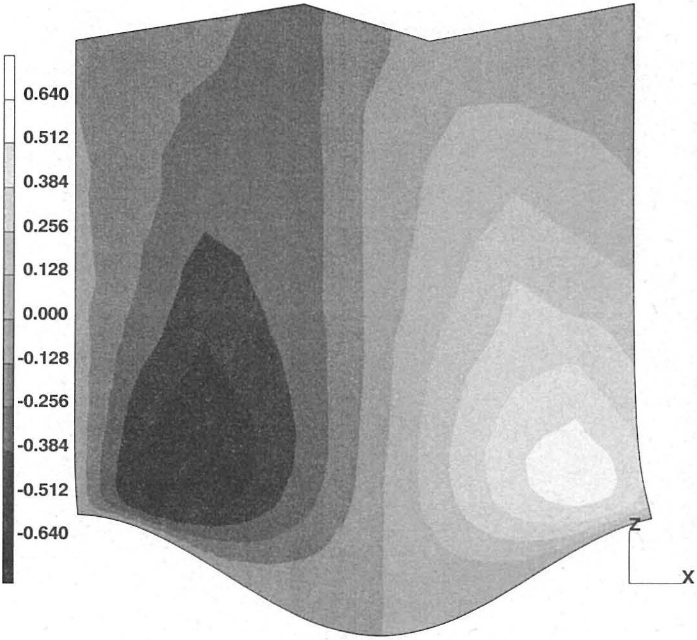

Fig. 4.3: Vertical velocities for no-sliding conditions. Parameters: $a = 2$ m, $\lambda = 20$ m, $h = 200$ m, $n = 3$, and $\rho g \sin\alpha = 8.99577 \times 10^{-3}$ bar/m. Velocities are in m/a. Flow direction is from left to right.

perfectly lubricating plane at the cross-section below the medial moraine without disturbing the velocity or the stress fields. The junction point can then be considered to mark the transition from a no-slip to a free-slip boundary condition. This change in boundary condition is independent of other factors affecting the flow pattern of a confluence such as changes in mean velocity direction and thicknesses. It is the subject of this section to examine this mechanical aspect of the merging of two glaciers to get a qualitative picture of the associated changes in horizontal surface velocities and stress fields as well as in the surface elevation of a confluence area. It will be assumed that the confluence is perfectly symmetrical and infinitely thick. The assumption of infinite thickness restricts the applicability of the results to those sections of a particular confluence where ice predominantly experiences resistance from the margins. The angle between the two tributaries will be set to zero, which can be seen as a part of the definition of the problem considered. There will there-

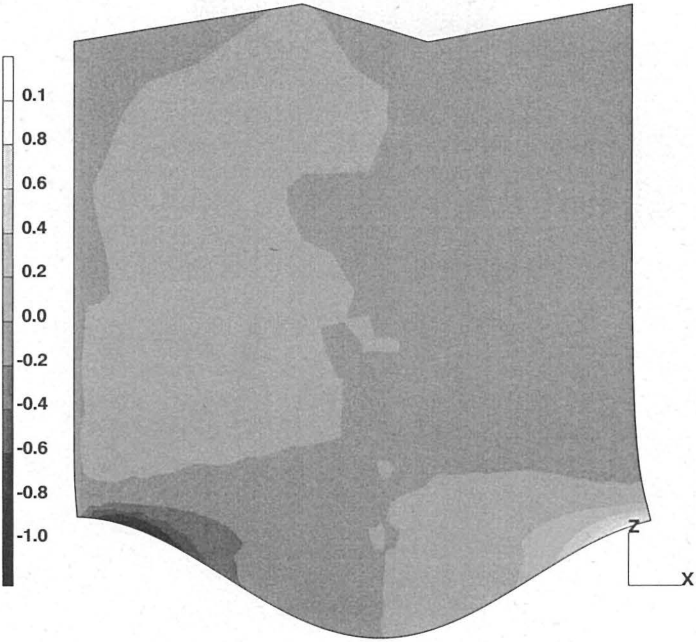

Fig. 4.4: Vertical strain rates ($2\dot{\epsilon}_{zz}$) for no-sliding conditions. Parameters: $a = 2$ m, $\lambda = 20$ m, $h = 200$ m, $n = 3$, and $\rho g \sin\alpha = 8.99577 \times 10^{-3}$ bar/m. Strain rates are in a^{-1}.

fore be no prescribed convergence of flow lines. Thickness changes will be ignored and plane strain conditions assumed.

Flow across a no-slip/free-slip transition has been studied theoretically by Hutter and Olunloyo (1980, 1981) and Barcilon and MacAyeal (1993). Hutter and Olunloyo found the normal and the shear stresses to be singular across the transition point. This can lead to high erosion rates, in agreement with observations (Hutter and Olunloyo, 1981).

Barcilon and MacAyeal confirmed and corrected previous results. They found a gradual velocity change across the transition but singularities in shear stress and pressure at the point of transition. The singularity in pressure represented an inconsistency with the assumptions made, causing first-order pressure to exceed the zeroth-order pressure. They therefore concluded that the problem remains open and unsolved. As a consequence this problem must (at least for the time being) be solved numerically.

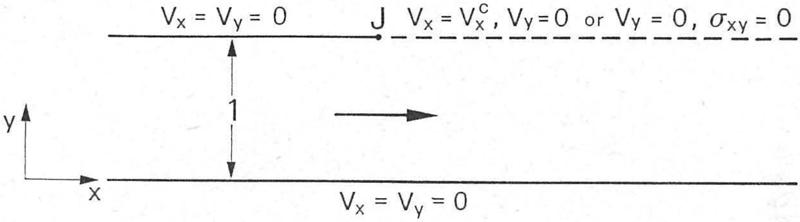

Fig. 4.5: An infinite strip of highly viscous material. The thick lines represent the glacier boundary and the long dashes a centerline of a conceptual confluence. Only one half of the perfectly symmetrical confluence is shown. J denotes the junction point. Along glacier boundaries no-slip boundary conditions are used. Along the centerline two types of boundary conditions are considered: prescribed velocity variation, and a free-slip condition. For prescribed velocity an analytical solution can readily be found for a linear fluid. The no-slip case has to be solved numerically.

The no-slip/free-slip transition problem is difficult to solve because at a part of the ice-bedrock interface velocities are prescribed (*i.e.* set to zero) and on the remaining section shear stresses together with normal velocities are prescribed. If only velocity variations along the interface were to be prescribed, the solution of the corresponding problem would be straightforward. Velocity along a confluence centerline will to a large extent be determined by factors not incorporated in the 2D map-plane model, such as surface inclination and bedrock geometry. Hence, even an exact solution to the no-slip/free-slip problem would only be partially applicable to the physical problem considered. From an observational point of view, information on the velocity field caused by a physically motivated velocity variation along the centerline are, especially as a supplement to a no-slip/free-slip solution, also of considerable interest. This problem, where the velocity along the centerline is an input and not an output, has the great advantage of being, at least for a linear viscous fluid, exactly solvable.

In Sec. 4.2.2 an exact solution of the response of an infinite strip of a highly linear viscous fluid to velocity variation at one of the boundaries will be given. The procedure is similar to the one used by Balise and Raymond (1985) in calculating the transfer of basal sliding variations to the surface of a linearly viscous glacier.

In Sec. 4.2.3 a numerical solution will be presented for the no-slip/free-slip problem with no free surface.

4.2.1 Analytical approach

The problem considered is depicted in Fig. 4.5. The equations that are to be solved are

$$v_{i,i} = 0, \tag{4.5}$$

$$\sigma_{ij,i} + \rho f_j = 0, \tag{4.6}$$

$$\dot{\epsilon}_{ij} = A\sigma'^{\,(n-1)/2}_{II}\,\sigma'_{ij}. \tag{4.7}$$

The equations will now be non-dimensionalized by scaling v_i, σ_{ij} and t with "natural" quantities of the model. Since the width of the channel in the down-stream direction of the confluence is $2d$, d is a natural length scale. The analytical solutions for the velocity and the shear stress for an infinitely deep channel of uniform width $2d$ are

$$\tau_{xy} = -\tau y/d, \tag{4.8}$$

$$u = \frac{2A\tau^n d}{n+1}\{1 - |y/d|^{n+1}\}, \tag{4.9}$$

where $\tau = \rho g d \sin\alpha$ is a scaling for the stresses. A convenient scaling factor for t can be defined to be the time it takes for the strain at the wall to obtain the value unity, *i.e.* $t = cT$ where c is defined by

$$\int_0^c \dot{\epsilon}\,dt = 1, \tag{4.10}$$

The following scalings are therefore introduced:

$$x_i = dX_i \quad , \quad \sigma_{ij} = \tau\Sigma_{ij} \quad , \quad p = \tau P \quad , \quad t = (2A\tau^n)^{-1}T. \tag{4.11}$$

where capital letters are used for non-dimensional quantities.

The non-dimensional velocity V_i is

$$v_i = \frac{x_i/X_i}{t/T}V_i = 2Ad\tau^n\,V_i, \tag{4.12}$$

and the non-dimensional strain rates E_{ij} are

$$\dot{\epsilon}_{ij} = \frac{T}{t}E_{ij} = 2A\tau^n E_{ij}. \tag{4.13}$$

The maximum value of V_X will be $(n+1)^{-1}$. Notice that the maximum of the shear stress and not the pressure is used to scale the stresses.[3] In two dimensions the non-dimensionalized equations are then

$$\frac{\partial V_X}{\partial X} + \frac{\partial V_Y}{\partial Y} = 0, \tag{4.14}$$

$$\frac{\partial \Sigma_{XX}}{\partial X} + \frac{\partial \Sigma_{XY}}{\partial Y} = -1, \tag{4.15}$$

$$\frac{\partial \Sigma_{YX}}{\partial X} + \frac{\partial \Sigma_{YY}}{\partial Y} = 0, \tag{4.16}$$

$$E_{ij} = \frac{1}{2}\Sigma'^{\,(n-1)/2}_{II}\,\Sigma'_{ij}. \tag{4.17}$$

For $n = 1$ the constitutive equation is $2E_{ij} = \Sigma'_{ij} = \Sigma_{ij} + P\delta_{ij}$, which if substituted into the momentum equation gives, together with the equation of continuity

$$V_{i,i} = 0, \tag{4.18}$$

$$\frac{\partial^2 V_X}{\partial X^2} + \frac{\partial^2 V_X}{\partial Y^2} = \frac{\partial P}{\partial X} - 1, \tag{4.19}$$

$$\frac{\partial^2 V_Y}{\partial X^2} + \frac{\partial^2 V_Y}{\partial Y^2} = \frac{\partial P}{\partial Y}. \tag{4.20}$$

---

[3] Various authors have scaled the stresses to the basal pressure, *e.g.* Barcilon and MacAyeal (1993) and Hutter (1983).

4.2.2 Analytical solution for $n = 1$

Capitalized letters will no longer be used. It is to be understood that all variables are dimensionless.

For $n = 1$ Eqs. (4.18) to (4.20) can be solved for an infinite strip with prescribed velocities or stresses as boundary condition. Only anomalous fields resulting from a prescribed velocity anomaly at the boundaries will be considered, and the part of the flow that is gravity driven will be ignored, since it will simply add linearly to the anomalous velocity distribution. The method used for the derivation of the solutions follows Gudmundsson (1989) closely.

The fundamental equations are:

$$\frac{\partial p(x,y)}{\partial x} = \frac{\partial^2 v_x(x,y)}{\partial x^2} + \frac{\partial^2 v_x(x,y)}{\partial y^2}, \tag{4.21}$$

$$\frac{\partial p(x,y)}{\partial y} = \frac{\partial^2 v_y(x,y)}{\partial x^2} + \frac{\partial^2 v_y(x,y)}{\partial y^2}, \tag{4.22}$$

$$\frac{\partial v_x(x,y)}{\partial x} + \frac{\partial v_y(x,y)}{\partial y} = 0. \tag{4.23}$$

The stress-strain relations are:

$$\sigma_{xx}(x,y) = -p(x,y) + 2\frac{\partial v_x(x,y)}{\partial x}, \tag{4.24}$$

$$\sigma_{xy}(x,y) = \frac{\partial v_x(x,y)}{\partial y} + \frac{\partial v_y(x,y)}{\partial x}, \tag{4.25}$$

$$\sigma_{yy}(x,y) = -p(x,y) + 2\frac{\partial v_y(x,y)}{\partial y}, \tag{4.26}$$

These equations will now be Fourier transformed according to

$$f(k) = \int_{-\infty}^{+\infty} f(x) e^{ikx}\, dx \tag{4.27}$$

giving

$$ikp(k,y) + \frac{\partial^2 v_x(k,y)}{\partial y^2} - k^2 v_x(k,y) = 0, \tag{4.28}$$

$$\frac{-\partial p(k,y)}{\partial y} + \frac{\partial^2 v_y(k,y)}{\partial y^2} - k^2 v_y(k,y) = 0, \tag{4.29}$$

$$-ikv_x(k,y) + \frac{\partial v_y(k,y)}{\partial y} = 0, \tag{4.30}$$

$$\sigma_{xx}(k,y) = -p(k,y) - 2ik\, v_x(k,y), \tag{4.31}$$

$$\sigma_{xy}(k,y) = \frac{\partial v_x(x,y)}{\partial y} - ik\, v_y(k,y), \tag{4.32}$$

$$\sigma_{yy}(k,y) = -p(k,y) + 2\frac{\partial v_y(k,y)}{\partial y}. \tag{4.33}$$

With the help of Eqs. (4.30) and (4.28), $p(k,y)$ can be expressed as a function of $v_y(k,y)$, and that expression put into Eq. (4.29) resulting in one inhomogeneous linear differential equation of fourth order for $V_y(k,y)$.

$$\frac{\partial^4 v_y(k,y)}{\partial y^4} - 2k^2 \frac{\partial^2 v_y(k,y)}{\partial y^2} + k^4 v_y(k,y) = 0. \tag{4.34}$$

This differential equation can easily be solved. The solution is

$$v_y(k,y) = (A(k) + B(k)ky)e^{ky} + (C(k) + D(k)ky)e^{-ky}, \tag{4.35}$$

where the *integration functions* $A(k)$, $B(k)$, $C(k)$, and $D(k)$ are to be determined through the boundary conditions.

Using Eqs. (4.28) and (4.30) gives

$$v_x(k,y) = -i\{(A(k) + B(k)(1+ky))e^{ky} + (D(k)(1-ky) - C(k))e^{-ky}\}, \tag{4.36}$$

$$p(k,y) = 2k(B(k)e^{ky} + D(k)e^{-ky}), \tag{4.37}$$

Upon using Eqs. (4.31), (4.32) and (4.33) one obtains

$$\sigma_{xx}(k,y) = -2k\{(A(k) + B(k)(2+ky))e^{ky} + (D(k)(2-ky) - C(k))e^{-ky}\}, \tag{4.38}$$

$$\sigma_{xy}(k,y) = -2ik\{(A(k) + B(k)(1+ky))e^{ky} + (C(k) + D(k)(ky-1))e^{-ky}\}, \tag{4.39}$$

$$\sigma_{yy}(k,y) = 2k\{(A(k) + B(k)ky)e^{ky} - (C(k) + D(k)ky)e^{-ky}\}. \tag{4.40}$$

The problem is now formally solved.

4.2.2.1 Boundary conditions

The boundary conditions are

$$v_x(k,0) = v_y(k,0) = v_y(k,1) = 0 \tag{4.41}$$

and

$$v_x(k,1) = -iv^c_x(k), \tag{4.42}$$

where $-iv^c_x(k)$ is the Fourier transform of $v_x(x,1)$, which describes the velocity anomaly along the centerline ($v^c_x(k) = iv_x(k,1)$).

The resulting system of equations is

$$\begin{pmatrix} 2 & 1 & 1 \\ \hat{\alpha} - \hat{\beta} & \hat{\gamma} & \hat{\delta} \\ \hat{\alpha} + \hat{\beta} & \hat{\alpha} + \hat{\gamma} & \hat{\beta} - \hat{\delta} \end{pmatrix} \begin{pmatrix} A(k) \\ B(k) \\ D(k) \end{pmatrix} = \begin{pmatrix} 0 \\ 0 \\ v^c_x(k) \end{pmatrix}, \tag{4.43}$$

where $A(k) = -C(k)$, and the abbreviations

$$\hat{\alpha} := e^{k} \quad \hat{\beta} := e^{-k} \quad \hat{\gamma} := ke^{k} \quad \hat{\delta} := ke^{-k} \tag{4.44}$$

have been used.

The solution is

$$\begin{pmatrix} A(k) \\ B(k) \\ C(k) \\ D(k) \end{pmatrix} = \frac{v_x^c(k)}{(\hat{\alpha}-\hat{\beta})^2 - 4\hat{\gamma}\hat{\delta}} \begin{pmatrix} \hat{\delta} - \hat{\gamma} \\ \hat{\alpha} - \hat{\beta} - 2\hat{\delta} \\ -\hat{\delta} + \hat{\gamma} \\ -\hat{\alpha} + \hat{\beta} + 2\hat{\gamma} \end{pmatrix} \tag{4.45}$$

which can be substituted into Eqs. (4.35) to (4.40) to yield the velocities, the stresses and the pressure in terms of the velocity perturbation along the centerline. Notice that the solutions do not depend on the viscosity η. Because of the linearity of the underlying differential equations, the sum of the solutions corresponding to two different centerline velocity variations can be superimposed to give the solution of the combined velocity variation. To understand the general properties of the solutions, it will therefore suffice to consider the effect of some particularly simple type of velocity perturbation. A harmonic velocity variation is the most logical choice, since it produces anomalous velocity fields of the same form and frequency. Only the phases and the amplitudes are different.

4.2.2.2 Velocities and pressure as functions of k and y

Consider the velocity and the pressure as a function of k and y for a velocity perturbation of the type $v_x(k, y) = 1$, *i.e.* a harmonic velocity variation. Fig. 4.6 displays the longitudinal velocity $v_x(k, y)$ for $0 \leq k \leq 4\pi$, and Fig. 4.7 the corresponding transversal velocity $v_y(k, y)$. Because of the boundary conditions, $v_x(k, y)$ is unity for $y = 1$ and zero for $y = 0$. Positive values mean that $v_x(x, y)$ is, for some particular value of x, pointing in the same direction as $v_x(x, 1)$, and negative values that the ice is flowing in the opposite direction to the applied velocity perturbation. Since $v_x(k, y)$ changes its sign from positive to negative as y goes from one to zero, the velocity anomaly must recirculate. And in fact it does so for all values of k. The transition point, *i.e.* where $v_x(k, y) = 0$ for $y > 0$, is a function of k, and moves towards $y = 1$ as $k \to \infty$. For $k = 0$ the transition is at $y = 2/3$, as can be found by calculating the limit of $v_x(k, y)$ as $k \to 0$. Hence, for at least two thirds of the glacier cross-section, the direction of the anomalous velocity flow is opposite to the direction of the main flow. This will reduce the maximum velocity of the flow up-stream of the junction point and shift it towards the centerline. For long wavelength velocity components this reduction is quite large, or about 30 % of the applied velocity perturbation, but decreases with increasing k. The position of the maximum negative velocity is also dependent on k. For $k = 0$ it is situated at $y = 1/3$, and moves towards the centerline (*i.e.* $y = 1$) with increasing k.

Balise and Raymond (1985) found the ice to recirculate only for wavelengths shorter than ≈ 5.2, corresponding to $k < 1.2$. This difference is caused by the different boundary conditions at $y = 0$. Balise and Raymond (1985) used a free-surface

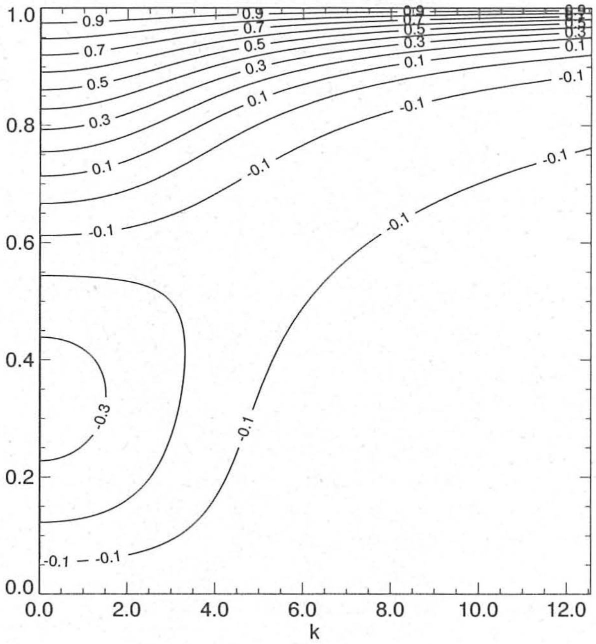

Fig. 4.6: Phase-space picture of the anomalous velocity $v_x(k, y)$ for $v_x(k, 1) = 1$. Contour lines give the relative amplitudes of the longitudinal velocities with respect to a prescribed velocity perturbation along the upper boundary. The upper boundary ($y = 1$) is referred to as the centerline. Velocities along the lower boundary ($y = 0$) are set to zero. The zero contour line gives the y-position of the point where longitudinal velocities change from being directed in the same direction as the applied velocity perturbation, to being directed in the opposite direction.

boundary condition, allowing the surface to react in such a way as to compensate for the mass transfer caused by the velocity perturbation. Because of the no-slip boundary conditions at $y = 0$, however, there is no free surface and internal flow must be set up to counteract the mass transfer at $y = 1$ and ensure mass conservation.

The transversal anomalous velocity is, as Fig. 4.7 shows, always negative, *i.e.* as a function of y, $v_y(x, y)$ does not change its direction. Notice that, as can be seen by comparing Eq. (4.35) with Eq. (4.36), $v_x(x, y)$ and $v_y(x, y)$ are 90° out of phase. v_y therefore reaches a maximum where v_x changes its sign. Hence, the maximum of $v_y(k, y)$ depends on k in exactly the same way as the zero line of $v_x(k, y)$. Transverse velocities can be a substantial fraction of the applied velocity perturbation. The anomalous velocities will therefore cause a marked convergence of the flow-lines of the main flow, even though the mean flow shows no convergence, as well as a transversal compression close to the centerline and extension close to $y = 0$. With

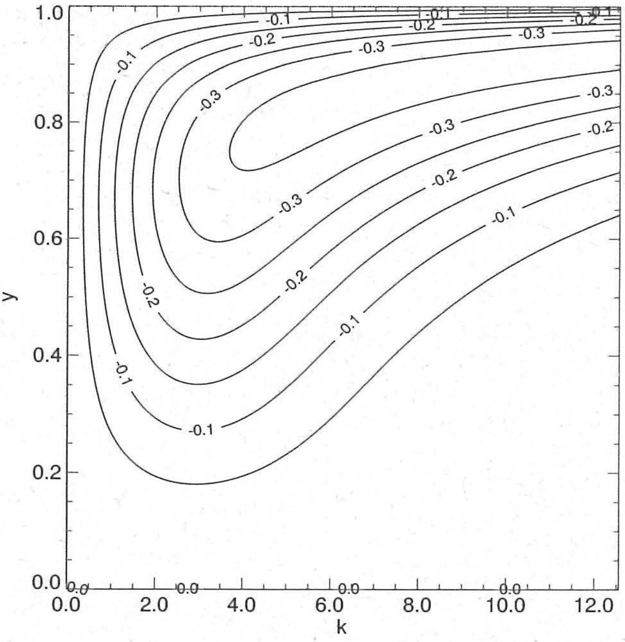

Fig. 4.7: Phase-space picture of the anomalous velocity $v_y(k, y)$ for $v_x(k, 1) = 1$.

increasing k, the maximum of $v_y(k, y)$ moves towards $y = 1$, and becomes more localized, causing larger velocity gradients. Since

$$\lim_{y \to 1} \frac{\partial v_y(k, y)}{\partial y} = k \tag{4.46}$$

the transversal, and the longitudinal, strain rates go linearly to infinity with k, *i.e.* the strain rates become singular in the limit of infinitely high frequencies. The shear strain rates also increase linearly with k towards infinity. In the high frequency limit all strain rates are infinite and localized at $y = 1$. This comes as no surprise since in this limit velocity gradients are in fact forced to become infinite. Although these singularities resemble somewhat those resulting from the comprehensive theoretical treatment of the no-slip/free-slip problem by Hutter and Olunloyo (1980, 1981) no comparison can be made since the two problems considered are fundamentally different. In the treatment of Hutter and Olunloyo the singularities are output and result from the boundary conditions, whereas here the singularities are in essence prescribed.

In the low frequency limit there is no transversal or longitudinal strain, as expected since longitudinal gradients are zero, the deformation being of pure shear type with $\dot{\epsilon}_{xy}(k = 0, y = 1) = 4$ and $\dot{\epsilon}_{xy}(k = 0, y = 0) = -2$.

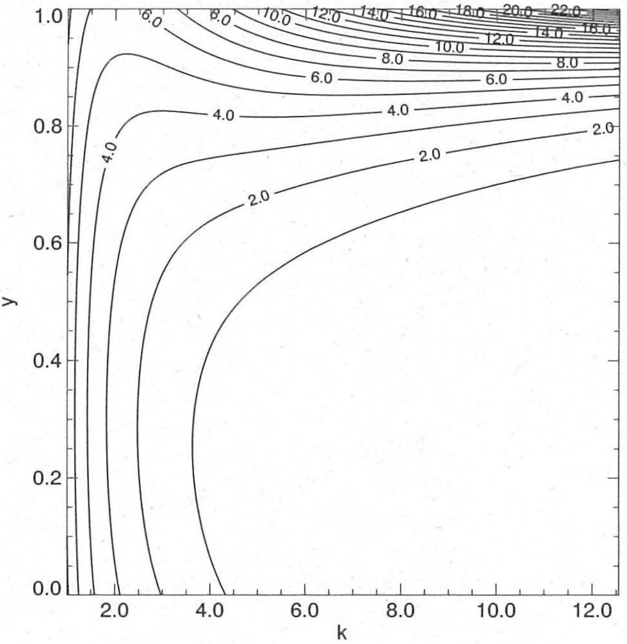

Fig. 4.8: Phase-space picture of the anomalous pressure distribution $p(k, y)$, for $v_y(k, 1) = 1$.

The pressure distribution is of interest because lines of constant pressure will correspond, to some extent, to contour lines on the glacier surface. This is only approximately true because, in general, the deformation will not be of pure plane strain type. Fig. 4.8 gives the pressure as a function of k and y. There will be a pressure drop at $y = 1$ if the velocities increase along the centerline. Close to the junction point one therefore expects a surface depression. This can easily be seen on the Unteraarglacier as well as on numerous other confluences. The pressure drop is strongly dependent on k. It can be shown that $p(k, 1)/p(k, 0) \to \infty$ as $k \to \infty$ representing an infinite pressure drop. The long wavelength limit is: $p(k, 1)/p(k, 0) \to 1$ as $k \to 0$, and the pressure drop will be almost constant across the glacier. Surface elevations close to $y = 0$ will in general be larger than at $y = 0$ for velocities increasing in x direction. This downward slope towards $y = 1$ is needed in order to drive the transverse flow. Superimposed on the general slope of the glacier this anomalous surface change causes the contour lines to tilt somewhat toward the confluence. Tilting of this type can easily be seen in Fig. 3.3, and Anderton (1970) has observed a converging of flow-lines just below the confluence of the north and the central arm of the Kaskawulsh Glaçier and apparently correlated changes in surface slope.

4.2.2.3 Solution for a velocity increase along the centerline

Although the anomalous velocities can best be understood by considering their representation in the (k, y) space it is instructive to look at one particular case in the (x, y) space. Velocities, stresses and pressure were calculated for an applied velocity perturbation of the form

$$v(x,1) = -\cos(\pi x) \quad \text{if} \quad 1/2 \leq x \leq 3/2 \quad \text{and} \quad v(x,1) = 0 \quad \text{otherwise.} \qquad (4.47)$$

The junction point is thought to be at $x = 0.5$ and the mean glacier flow is from left to right.

The Fourier-integrals were approximated through Fourier-series and $v(x, 1)$ was therefore in fact periodic. The period was chosen to be 8π, and was sufficiently large to make the Fourier-coefficient corresponding to the zero frequency small compared to other terms.

Fig. 4.9 depicts velocities resulting from a velocity variation along the centerline. The transversal flow caused by the velocity increase along $y = 1$ can be seen. $v_x(k, y)$ changes its sign at $y \approx 0.75$ which is in agreement with Fig. 4.6. Where the anomalous flow direction is opposite to the mean flow, velocities will be reduced. Since the region of inverse flow will always be larger than two thirds of the cross-section, maximum ice velocities will be expected to decrease as ice enters a confluence, and then to shift from the centers of the tributaries direction toward the centerline. This kind of velocity decrease can be seen in Fig. 3.13 and has also been observed on the Kaskawulsh Glacier (Anderton, 1970). Since a change of other factors affecting flow velocities, such as basal boundary conditions, cannot be excluded the question remains open as to whether this is indeed the cause of the observed velocity decrease. The inverse anomalous velocities will also be expected to pile up ice and to cause a local increase in surface elevation and a tilting of contour lines as discussed above.

Fig. 4.10 depicts the deviatoric principal strain rates.

Close to the junction point at $(x, y) = (1/2, 1)$ there is a longitudinal extension and a concomitant transversal compression. This is in qualitative agreement with observational findings. Somewhat below the junction point the orientation of the principal strain rates changes so that the centerline becomes subjected to shear. The confluence is therefore not perfectly symmetrical. This is expected since the applied perturbation velocity distribution does not result from some symmetry requirements but was simply assumed. Note that the most of the conclusions given above do not depend critically on the confluence being symmetrical. They only depend on the general properties of the flow solutions.

The pressure drop associated with the change in velocity along the centerline (from zero to some finite value) can be seen in Fig. 4.11. It is more or less constant across the glacier since the wavelength is relatively long. For shorter wavelengths the pressure drop at and below the junction point increases and tends to infinity as $k \to 0$.

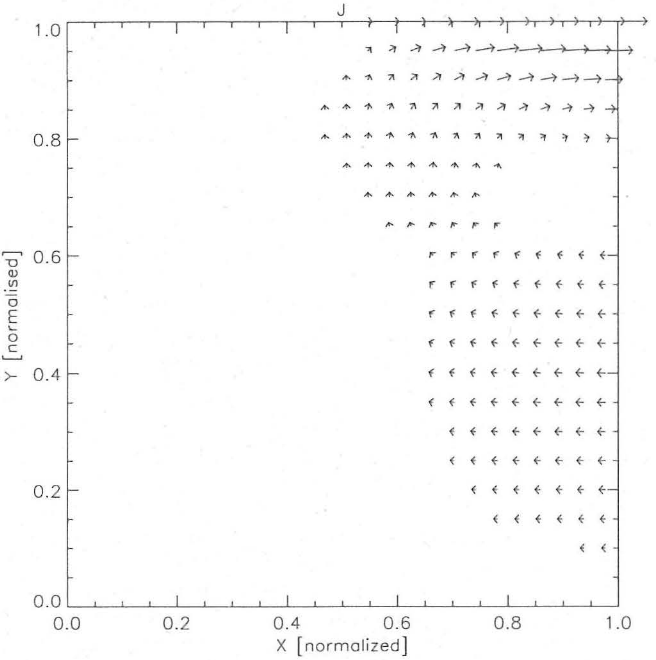

Fig. 4.9: Anomalous velocity distribution. The junction point is at $(x, y) = (1/2, 1)$, and is denoted by the letter J. A prescribed velocity profile along the upper boundary is used: $v(x, 1) = -\cos(\pi x)$ if $1/2 \leq x \leq 3/2$, $v(x, 1) = 0$ otherwise.

4.2.3 Numerical solution

Since a number of important conclusions about the general surface flow pattern of a confluence could be drawn with the help of the analytical solution for $n = 1$ it is important to see to what extent these findings remain correct for non-linear material behavior. It is also of interest to model a correct no-slip/free-slip transition boundary condition, in which case the velocity along the centerline will be an output of the corresponding model and not simply assumed.

Eqs. (4.14) to (4.17) were solved with the general purpose FE Program MARC. The model was infinite and periodic with period 10 and width 1. The coordinate system used was the same as that in Fig. 4.5. The lower left and the upper right corners of the model had the coordinates $(-5, 0)$ and $(5, 1)$ respectively. Along the lower boundary ($y = 0$) all velocities were suppressed. The junction point was at $(x, y) = (0, 1)$. To the left of the junction point along the upper boundary v_x and v_y were suppressed, but to the right of the junction point the ice was allowed to move freely in the x direction. At the left boundary velocities were set equal to those at the right boundary. No assumptions about the velocity profile or the stresses had to

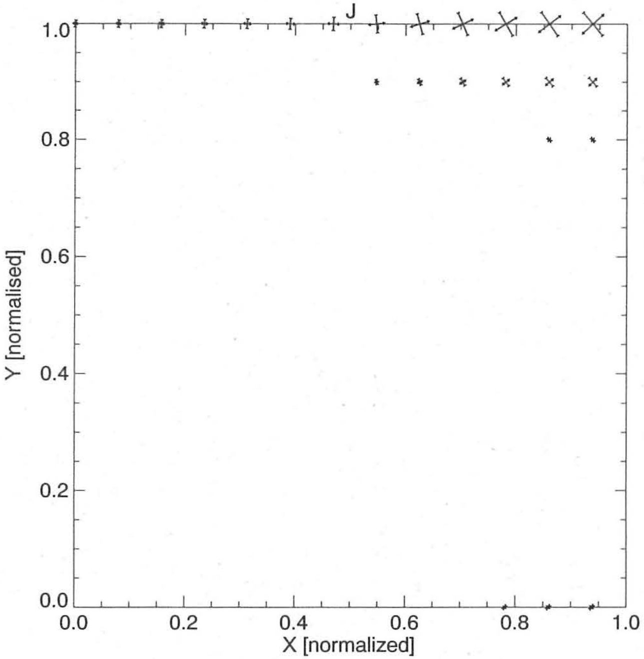

Fig. 4.10: Anomalous deviatoric stress field. The junction point is at $(x, y) = (1/2, 1)$, and is denoted by the letter J.

be made. Since the upper right corner of the model is in effect the same point as the upper left corner there are actually two junction points within the model, lying 5 units apart. The non-dimensionalization done in Sec. 4.2.1 corresponds to $A = 1/2$ and a driving stress of unity.

At the junction point there is an abrupt change of boundary conditions. Some distance X_L up as well as down-stream of that point the flow is Poiseuille flow. Some estimate is needed for this transition length X_L. The developing laminar flow in the entrance of a duct bears some similarity to the idealized confluence. Laminar entry length solutions can be found in the literature for circular and non-circular ducts and parallel plates. Shah and London (1978) give the following expression for the entrance length

$$X_L \approx \frac{0.6}{1 + 0.035\,\mathrm{Re}} + 0.056\,\mathrm{Re}, \tag{4.48}$$

valid within ±2 % for many duct shapes. The entrance length being defined as the that distance where the centerline velocity corresponds to 99 % of the fully developed Poiseuille value. For creeping flow $\mathrm{Re} \approx 0$ and $X_L \approx 0.6$. The distance of 5, from one junction point to the next, can therefore be considered to be sufficient.

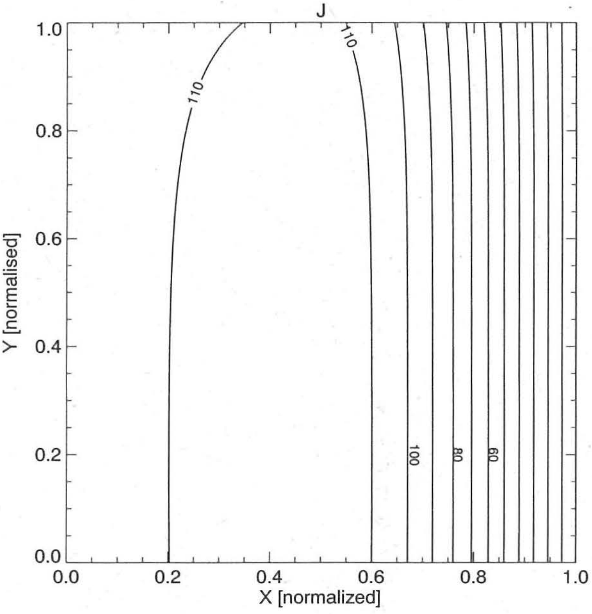

Fig. 4.11: Anomalous pressure distribution. The junction point is at $(x, y) = (1/2, 1)$, and is denoted by the letter J. A prescribed velocity profile along the upper boundary is used: $v(x, 1) = -\cos(\pi x)$ if $1/2 \leq x \leq 3/2$, $v(x, 1) = 0$ otherwise. The pressure drop in the x-direction is caused by the increase of flow velocity along the center-line for $x > 1/2$. There is also a pressure drop in the y-direction, the magnitude of which depends strongly on the wavelength λ of the applied velocity along the centerline. For $\lambda \to 0$ the pressure drop across the glacier at the hight of the junction point tends to infinity. For the particular form of the centerline velocity used for the generation of the figure, the pressure drop is small, because the wavelength used is rather large. For an ideal no-slip/free-slip transition, where the centerline velocity is calculated and not simply assumed as here, one expects the presence of high frequency components that will then lead to a sharp pressure drop. For a glacier with a free surface the pressure drop across the glacier will manifest itself in the form of a local surface depression at J and a super-elevated zone at the glacier margins diametrically opposite to J. The contour interval is 10 units.

Three models, with equidistant rectangular meshes but different grid size were used, one with grid size 0.1, *i.e.* 10 elements over the width of the model and having a total number of 1000 elements, another with grid size 0.05, and still another with grid size of 0.025 having a total of 16000 elements. To test the correctness of the calculations a channel flow was modelled, with velocities at the upper as well as the lower boundary set to zero. For $n = 1$ and $n = 3$ maximum velocities were $1/7.985$ and $1/64.32$ respectively , whereas the corresponding analytical values are $1/8$ and $1/64$. Both calculated number refer to the FE mesh with a grid size of 0.05. Results obtained with both the 0.05 and the 0.025 grid-size meshes differed by less than

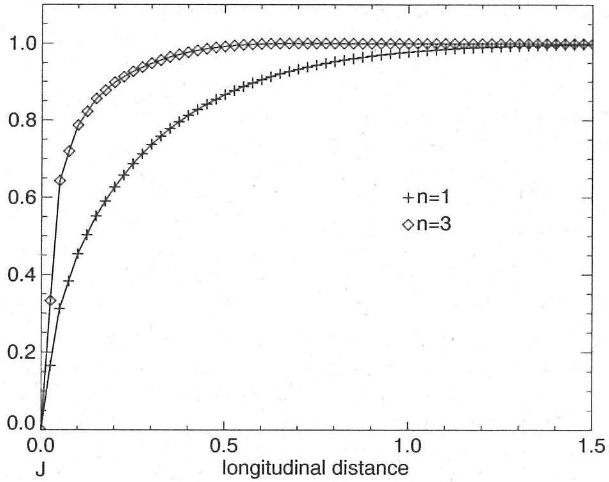

Fig. 4.12: Longitudinal velocities (v_x) along the centerline. J refers to the junction point. The velocities were normalized by the maximum longitudinal velocities at the centerline, which were 0.190 and 0.0417 for $n = 1$ and $n = 3$ respectively. Symbols represent the nodes where numerical values were obtained. The lines were formed by linear interpolation of the calculated values.

0.2%. For the final calculations, discussed below, the 0.025 mesh was used.

The element used was a linear 4-node quadrilateral plane strain element. The assumed strain formulation was used, and incompressibility was enforced with the constant dilatation method. This element does not lock in the incompressibility limit. It cannot represent a singular behavior, and any singularity of the underlying problem will be smeared out in the numerical solution over a region comparable in size to the spatial dimensions of the elements. Successive mesh refinement can therefore be used to detect a singularity. The numerical results do indeed suggest that longitudinal and transversal strain rates become singular at the junction point since a strong variation in calculated quantities, such as strain rates and velocities, was detected that became more localized and larger with each successive level of mesh refinement. On the basis of the analysis in Sec. 4.2.2 this singularity can be understood to be caused by the high frequency components introduced by the infinite velocity variation at the junction point.

The longitudinal velocity (v_x) along the centerline, as a function of the distance in the down-flow direction from the center-point for $n = 1$ and $n = 3$, can be seen in Fig. 4.12. The velocities were normalized by the maximum velocity at the centerline, which was 0.190 for $n = 1$, and 0.0417 for $n = 3$. Notice that these maximum velocities are smaller than those expected for an infinite channel with width $2d$. Because the channel section above the junction point has as smaller width of d, which reduces the overall flux, this velocity reduction is expected, and can be seen as a consequence of the fact that a factor of 2 increase in channel width, for a given driving stress, changes the volumetric flux by about a factor of 2^{n+2}. A real glacier would react to this change by lowering the driving stress below the junction point. In this conceptual model no corresponding changes in surface geometry, which is fixed, can be undertaken, and as a consequence the velocity will be determined in part by the ratio of the lengths of the two sections above and below the junction point, which for the model calculated was set equal to 1. This will, in turn, influence the magnitude of the velocity gradients over the confluence area. In what follows it will be assumed that the area over which the glacier reacts to velocity gradients does not depend on their magnitude, although the conclusions do not depend critically on this assumption. This assumption is reasonable for a creeping flow (the entrance length for a creeping laminar flow in a duct does, for example, not depend on the inflow velocity), but is not correct if acceleration terms are important.

The velocity increase at the junction point (denoted by a capital J in the figure) is very sharp. That the actual slope of the curve at the junction point is not accurately represented in the figure, and should not be finite but infinite, can be explained by two observations 1) the slope increases with each successive mesh refinement, and 2) the slope of the calculated curve in Fig. 4.12 changes abruptly at the second nodal point from the junction, the extrapolation of the curve through the other nodal points towards the junction suggesting a larger slope. Except for the immediate region of the junction point, calculated values obtained with the 0.05 and the 0.025 grid-size meshes differed by less than 1.2%. An infinite slope means that the longitudinal strain rates ($\dot{\epsilon}_{xx}$), and (because of the incompressibility condition) the transversal strain rates ($\dot{\epsilon}_{yy}$) will, become singular.

The region of velocity increase becomes more localized with increasing n, or, equivalently, the transition length gets shorter. For $n = 1$ and $n = 3$, 90 % of the maximum centerline velocity has been reached at $x = 0.78$ and $x = 0.30$ respectively. This is *a posteriori* justification of using a distance of 5 between the two no-slip/free-slip transitions within the model.

Fig. 4.13 depicts the longitudinal and the transversal velocities, along a transversal profile that traverses the channel at the position of the junction point. Velocities were, as in Fig. 4.12, normalized by the maximum longitudinal centerline velocities. Notice that the position of the junction point is represented by J in the figure. The maximum of the velocities is shifted somewhat towards the junction point with respect to the geometric center of the channel modelled. This shift is larger for $n = 3$ than for $n = 1$, and more pronounced for the transversal velocities than for the longitudinal ones. The maximum of the transversal velocity for $n = 3$ cannot, in fact, be localized precisely due the finite spatial dimensions of the FE mesh. The region of positive transversal strain rates is strongly localized around the junction point. The same observations as made in connection with Fig. 4.12 suggest that the slopes of all curves approach infinity at the junction point, and it is concluded that the finite slopes depicted result from numerical errors. Transversal velocities are quite large or about 18% of the maximum longitudinal velocities, leading to a marked convergence of flow-lines. This is in general agreement with the findings obtained in Sec. 4.2.2.

Longitudinal velocities for $n = 1$ and $n = 3$ as function of x and y over the confluence

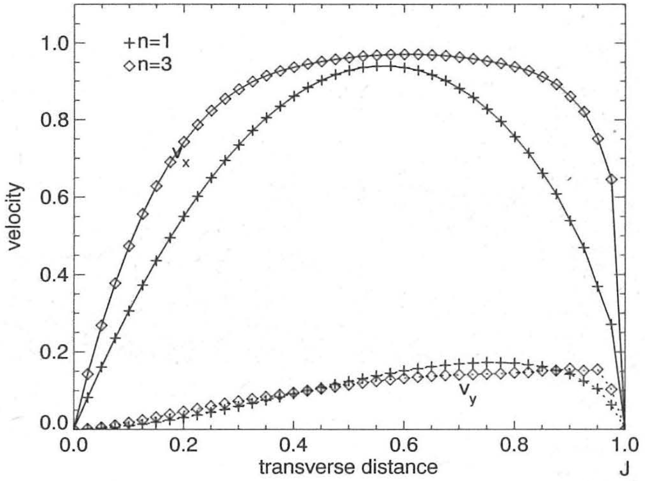

Fig. 4.13: Longitudinal (v_x) and transversal (v_y) velocities across the glacier at the position of the junction point. J refers to the junction point. The velocities were normalized by the maximum longitudinal velocities at the centerline. The symbols connected by solid lines represent longitudinal velocities (v_x) and symbols joined by dotted lines represent transversal velocities (v_y).

area, can be seen in Fig. 4.14 and Fig. 4.16 respectively. The corresponding transversal velocities are depicted in Fig. 4.15 and Fig. 4.17. Only a part of the region covered by the FE mesh is shown. The lower left point of the figure has the coordinates $(-1, 0)$ and the upper right one the coordinates $(2, 1)$. The junction point is, as said before, situated at $(0, 1)$. Light gray tones represent high velocities. No normalization was done. Flow is from left to right.

Figs. 4.14 and 4.16 show clearly how the longitudinal velocities decrease and increase again around the confluence. A velocity decrease of this kind has, as said above, been observed, although it cannot be unequivocally concluded that this mechanism is the cause. Except for the transition point the velocity variation is smooth. Notice that this velocity decrease is less pronounced and more localized for $n = 3$ than for $n = 1$. It cannot, however, be concluded that velocity gradients will in general become smaller with increasing n, since the difference in maximum velocities above and below the confluence point depends on the relative length of these two sections together with n.

The maximum of the transversal velocities (*cf.* Figs. 4.15 and 4.17) moves towards the boundary with increasing n. The region of transversal compression will consequently become smaller. The spatial velocity variation of v_y in flow-direction is limited to a region of similar extent as that of the spatial variation of v_x along the centerline.

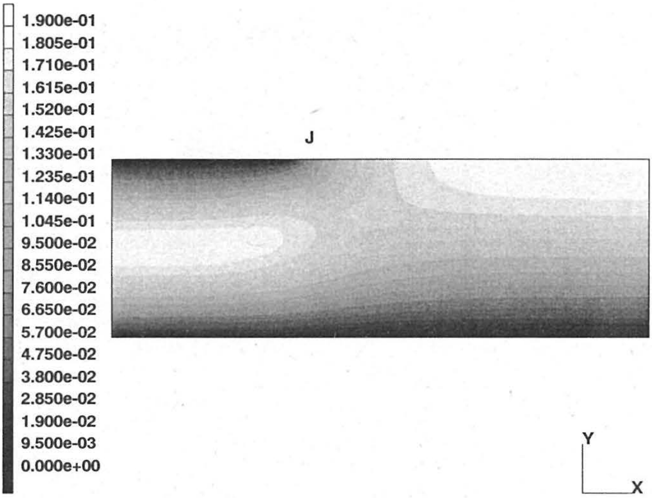

Fig. 4.14: No-slip/free-slip transition. v_x for $n = 1$. The model has a width of unity. The transition point is at the upper boundary, one unit length away from the left edge. Flow direction is from left to right. The coordinate system shown only gives its orientation and not its origin, which was at the lower boundary directly below the junction point.

4.2.3.1 Accuracy of the numerical solution

The numerical results strongly suggest that strain rates and stresses become singular at the junction point and that the slope of the velocity curve is infinite. The discussion in Sec. 4.2.2 indicates that this singularity is, at least for $n = 1$, associated with the infinitely high frequency components of the centerline velocity variation, suggesting that if the no-slip/free-slip transition point would be slightly smoothed out, making the infinite high frequencies disappear, there would be no singularity. This is, however, questionable since Hutter and Olunloyo (1981) found that the singularity remains even for a continuous transition from no-slip to viscous sliding.

The shape function of the elements used for the calculations does not account for singularities, and there will inevitably be errors introduced by this inappropriate choice of shape function. These errors are, however, not expected to propagate very far, since even for the region in the immediate neighborhood of the point of singularity, the balance equations will be, due to the integral nature of the FE method, fulfilled in an average sense (Bathe, 1982). Still, it must be concluded that a proper numerical treatment of this classic theoretical problem can only be done with the use of singular elements.

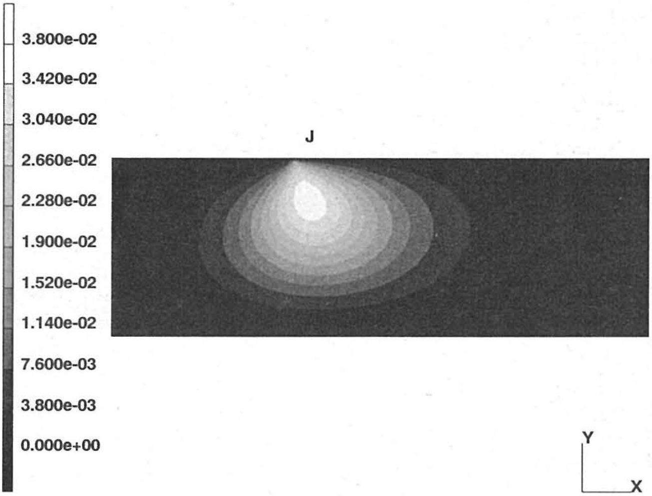

Fig. 4.15: No-slip/free-slip transition. Transversal velocities (v_y) for $n = 1$. The maximum of v_y can clearly be seen. Its position does not depend critically on the spatial resolution of the FE mesh. This distribution of transversal velocities causes a transversal compression close to the junction point (J), and a transversal extension at the margin lying diametrically opposite to J.

The inability of representing the singularity of the underlying solutions makes it difficult to estimate the numerical errors involved. Based on results obtained through successive mesh refinement, as well as comparison with analytical solutions, it can be concluded that overall errors in velocities are less than about 1%. Errors in fields that depend on velocity gradients can be significantly larger.

4.3 Summary

By introducing a simplified map-plane model of a confluence the main features of the observed surface velocity variation on the Unteraarglacier could be explained. A graphical summary of the results is given in Fig. 4.18. Because the map-plane model is strongly idealized, and not specific to one particular confluence the results obtained are considered to be of general validity.

A flow-line model was used to explain why the vertical strain rates along the centerline close to the junction point change from being positive (extension) at the surface to negative close to the bottom. This result is again also thought to be of general

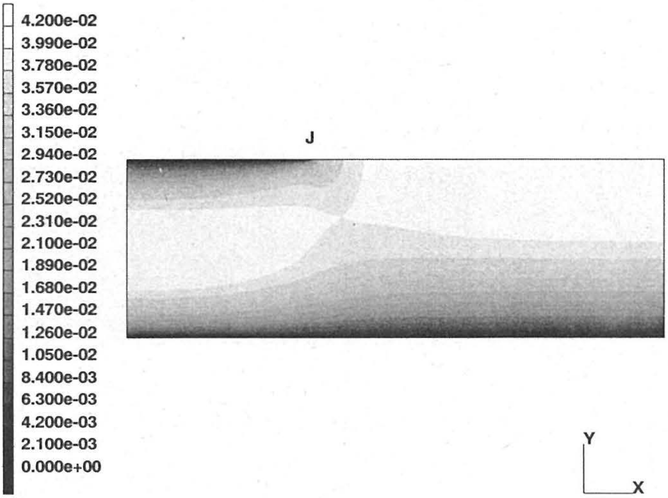

Fig. 4.16: No-slip/free-slip transition. Longitudinal velocities (v_x) for $n = 3$. The velocity decrease is not as strong as for $n = 1$.

validly and not limited to the Unteraarglacier only

The results can be summarized as follows:

- Along the centerline there will be a large transversal compression and longitudinal extension.
- Close to the junction point flow-lines will converge. This converging will happen even when the angle formed by the two tributaries is close to zero.
- Surface velocities will decrease as ice enters the confluence and then increase again.
- Immediately below the junction, a strongly localized surface depression will form, and at both margins of the tributaries lying diametrically opposite to the junction, surface heights will be built up. The spatial dimensions of the surface heights will be larger than those of the surface depression. This will cause a tilting of the contour lines towards the convergence area, giving the needed driving stresses for the transverse flow. If the angle formed by the two tributaries is large, *i.e.* close to 180° no "transverse" flow and no tilting of contour lines is expected.

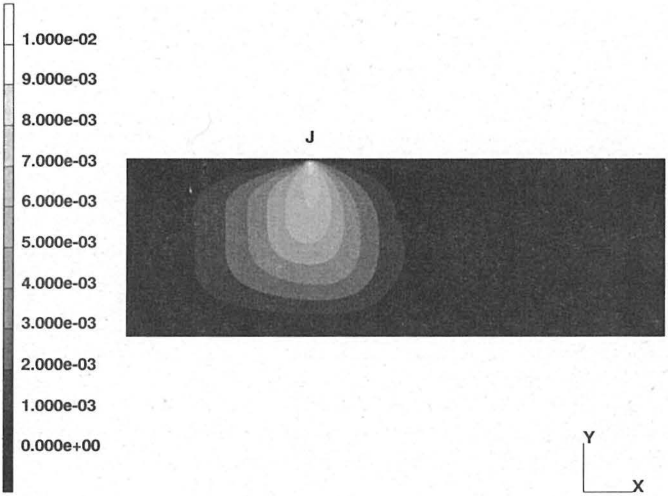

Fig. 4.17: No-slip/free-slip transition. Transversal velocities v_y for $n = 3$. The maximum of v_y lies much closer to J than it does for $n = 1$. The maximum is in fact found only two nodes away from J, which is at the verge of the spatial resolution of the mesh. Further mesh refinements might move the maximum further towards J and increase its magnitude. The zone of transversal compressive strain rates is strongly localized.

- Where ice thickness along a flow-line increases, which will in general be the case for the marginal ice entering a confluence, there will be a net vertical extension over the whole glacier depth. The vertical strain-rate variation will critically depend on the boundary conditions. If they are close to perfect sliding, the maximum of vertical strain rates will be situated somewhat above the bed-rock interface where the downward slope is the largest, lying for $n = 1$, about $\lambda/2\pi$ above the bed-line where λ is a typical wavelength of bedrock variations, and closer to the bed for $n > 1$. If no-slip boundary conditions are more appropriate, the maximum of their vertical extension will be further away from the bed, and the ice lying immediately above it will be subjected to vertical compression.

Increasing the value of n in the flow law shifts the maximum of the transversal flow towards the junction point. It also decreases the width and the length of the zone of transversal compression and longitudinal extension (making the transition length, which is 0.8 for $n = 1$, smaller and velocity gradients larger), and moves the maximum of vertical extension further downwards in the vertical direction.

The two conceptual models introduced explain qualitatively the surface strain-rate

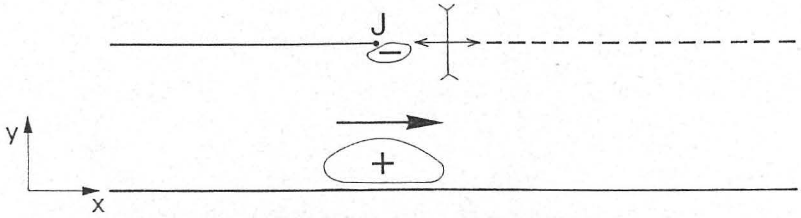

Fig. 4.18: Summary of the results obtained with the help of the map-plane model. J denotes the junction point, the plus symbol a super-elevated zone, and the minus symbol a zone of local surface depression. The thin lines represent velocity contours.

pattern as well as the vertical strain-rate variation measured on the Unteraarglacier. Observational findings, such as the decrease and the subsequent increase of surface velocity of both the Finsteraar and Lauteraarglacier as they enter the confluence, and the tilting of contour lines towards the junction point — at the beginning thought to be caused by the bedrock geometry — can now be seen to be general consequences of the special kinematics of confluence areas.

CHAPTER 5

A 3D Numerical Model of the Confluence Area of the Unteraarglacier

Although the conceptual models discussed in Chapter 4 gave valuable insight into the dynamics of converging glacier flow they represent a gross simplification, as they are 2D, whereas the actual flow field in fact strongly varies in all three spatial dimensions. To test the correctness of the inferences drawn from the 2D models — at least for the particular case of the Unteraarglacier — they must therefore be complemented by corresponding 3D calculations.

A further benefit that emerges from 3D-modeling is the possibility of a quantitative verification of the set of assumptions made about glacier flow used in the modeling procedure. This includes for example a test of the applicability and the correctness of the flow law and the boundary conditions.

The purpose of the 3D-calculations is therefore twofold: 1) to test with a fully 3D-model the correctness of the theoretical concepts developed in Chapter 4 and to further determine the universal features of flow dynamics of a glacier confluence, and 2) to quantitatively test assumptions about the rheological properties of glacier ice and the kinematic boundary conditions by comparing calculated velocities and strain rates with results from field measurements.

5.1 Program specifications and mesh generation

The general purpose FE program MARC was used for the calculation. A testing of the exactness of the numerical calculations done for incompressible creeping viscous flow has been described by (Gudmundsson, 1994a).

The FE element used for the calculation was an eight-node isoparametric, three-dimensional brick element, with trilinear interpolation. The assumed strain formulation was used to improve the bending characteristics of the element. Two different methods were used to enforce the conditions of incompressibility: the *constant dilatational method*, where a selective integration uses the eight Gaussian integration points for the calculation of the deviatoric strain-rate contribution and the centroid for the dilatation contribution, and the $\mathbf{v}$-*p-formulation*, where the velocities and the pressure are together considered as the unknown variables and the pressure interpolation function is of one order lower than the velocity interpolation functions

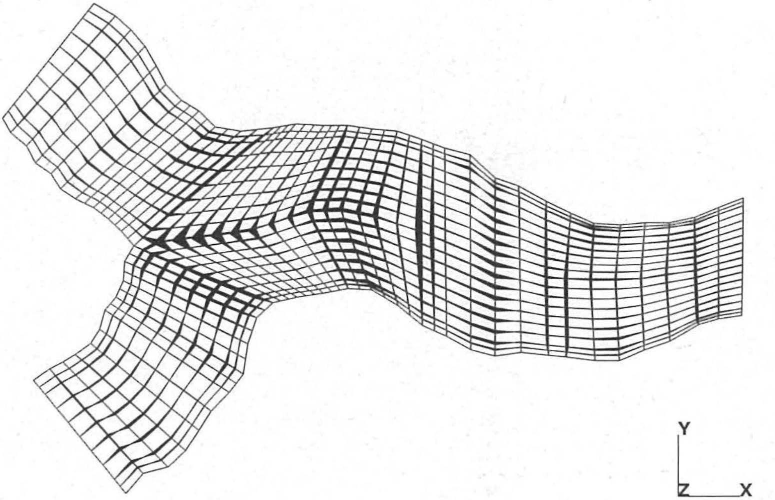

Fig. 5.1: The FE mesh used for the calculations of velocity field on the Unteraarglacier. The mesh consists of 6426 elements and 7920 nodes. The geometry of the mesh is based on a digital terrain model for the surface and radio-echo soundings for the bed-rock. The element type chosen was a eight-node isoparametric, three-dimensional brick element with a trilinear shape function.

(MARC, 1992; Gartling *et al.*, 1977; Chung, 1978; Bathe, 1982; Zienkiewicz *et al.*, 1984; Pironneau, 1989; Kleiber, 1989).

The coordinates of the nodes lying on the upper surface of the FE mesh were based on a digital terrain model from the year 1991. The same digital terrain model was used for the generation of Fig. 3.3. The coordinates of the nodes lying on the lower surface were generated by an algorithm described on page 25. Due to the number of FE nodes the generation of a 3D mesh has to be fully automated. To this end a number of programs were written that can be used for the automatic generation of a three-dimensional FE mesh of valley glaciers. The input needed consists of a number of transversal profiles giving the glacier depth, a digital terrain model of the glacier surface, and the coordinates of the glacier border. The development of this program package, called *3D FE mesh tools*, turned out to be quite time consuming (approximately three months were needed), but essential for the successful generation of the complicated mesh. This program package opens up the possibility of "mass production" of 3D FE models of valley glaciers. The resulting mesh and its geometry can be seen in Figs. 5.1 and 5.2. Meshes with various numbers of elements were generated. The calculations presented below were done with a mesh with 6424 elements and 7920 nodes. To get an estimate of the discretization error results obtained with a mesh consisting of 2800 elements and 3732 nodes was used

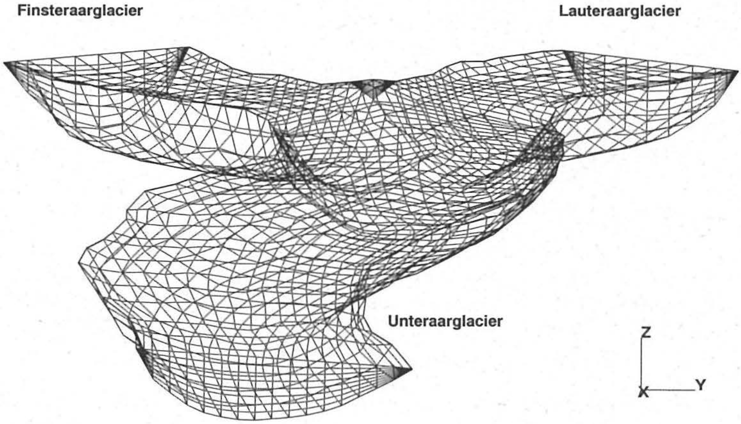

Fig. 5.2: A perspective plot of the FE mesh of the Unteraarglacier. Only the outlines of the elements are shown.

as a comparison.

The coordinates of the FE nodes correspond to the official Swiss coordinate system. The x axis points east, the y axis north, and the z axis points upwards.

The resulting equation system was solved with a direct as well as an iterative solver. The direct solver is based on the Gauss elimination algorithm. The iterative solver uses the conjugate gradient method with an element-by-element pre-conditioner. Considerable computational savings could be achieved with the use of the iterative solver, and it was hence used for almost all calculations.

The non-linearity of Glen's flow law results in a non-linear equation system that has to be solved in an iterative way. The iteration was continued until the maximum relative change in velocity over the whole mesh was less than 0.1 %. After each calculation the effective viscosity distribution was written to a file and could therefore be used as a starting distribution for the next calculation. A single calculation for five different values of n running from $n = 1$ to $n = 5$ using the iterative solver and a "good" starting values for the effective viscosity distribution took approximately 6.6 CPU hours on a Convex C3820. With no prior knowledge about the effective viscosity distribution the same calculations took approximately 27 hours. About 240 Mb of memory were needed for a single run.

It can be concluded that a fully 3D non-linear calculation of the flow field of temperate valley glaciers having spatial dimensions usually found in the Alps has become possible and poses no particular problems with respect to computer time or memory resources.

5.2 Flow law and boundary conditions

Sliding affects the internal deformation of the Unteraarglacier, as has been discussed in Sec. 3.3. It will in general be difficult to separate the effects that a change in flow law parameters have on the velocity field, from the changes caused by a different type of sliding law. One could in principle obtain some information on the form of the sliding law by observing simultaneously fluctuations of water pressure and velocity (Iken, 1978; Iken, 1981; Iken *et al.*, 1983; Iken and Bindschadler, 1986). Information of this kind is, however, not available for the confluence area of the Unteraarglacier. For this reason, it is practically impossible to model the summer velocities, as they are known to be caused to a large extent by sliding.

To circumvent this difficulty, it was decided to focus on the winter velocities, and the assumption was made that sliding has a negligible effect on the winter velocities of the Unteraarglacier. This simplifies the boundary conditions, since then no sliding law is needed. This simplification is important because the process of sliding is poorly understood and has traditionally been dealt with in an *ad hoc* way.

The assumption is justified to some extent by the fact that sliding with bed separation is not effective at the Unteraarglacier during the winter. Measurements of water levels in January 1992 showed that water pressures were quite low and possibly close to zero (*cf.* p. 40). No velocity variations were observed during the winters 1991/1992 and 1992/1993. This does, of course, not exclude the possibility that some sliding may be taking place, but if so, it is not dependent on high water pressures.

No observations of marginal sliding over these same winter periods were made. Notice also that sliding without bed separation is expected to depend mainly on the magnitude of shear stresses, and since marginal shear stresses of the confluence area are similar to bottom shear stresses — for some cross-sections stresses are actually largest at the margins — and physical properties of basal ice are not expected to change significantly over the glacier cross section[1], the possibility of significant sliding over the winter is judged to be unlikely. Only direct measurements can, however, give unambiguous answers, so this assumption remains to be tested at some later point in time.

Glen's flow law has most often been used for modeling purposes, although there are reasons to believe that it represents some, if not drastic, oversimplification of the rheological behavior of glacier ice. Moisture and debris content, ice fabric, ice composition, *etc.* , affect the rheological properties of ice (*cf.* (Mellor, 1980; Jacka, 1984a; Jacka, 1984b; Duval *et al.*, 1983; Lile, 1978; Budd and Jacka, 1989; van der Veen and Whillans, 1990)). Since these factors vary from one glacier to another, the values for A and n that are in some sense appropriate for one particular glacier, cannot be used with confidence for other glaciers. Furthermore, n and A are possibly only approximately independent of the stress regime. It therefore comes as no

---

[1] This may be especially true for a confluence area, since the drastic change in bed geometry will introduce a large scale redistribution of ice. Marginal ice flowing past the junction point will, as an example, be transferred towards the deepest parts of the glacier cross-sections below the junction point.

surprise, that there is no general consensus on what values for the parameters n and A are to be considered to be the correct ones, although traditionally $n = 3$ has probably most often be used in flow modeling, *cf.* Colbeck and Evans (1973), Raymond (1980), Paterson (1981), Doake and Wolff (1985), Alley (1992).) The search for a single flow law for ice may be illusory (Lliboutry and Duval, 1985).

Still, the decision was made to use Glen's flow law for modeling the ice flow at the Unteraarglacier. A and n were considered to be purely phenomenological parameters that could be varied freely in an attempt to obtain best possible agreement between calculated and measured quantities. The justification for using Glen's flow law is not that it is physically the most appropriate one, or that field measurements have shown it to be correct, but rather that it has a small number of parameters, and has been shown to be flexible enough to give a good fit to a number of field observations. There is also a historical argument for using Glen's flow law, because the use of it allows an easy comparison with results from other areas.

Only a section of the Finsteraar, Lauteraar, and Unteraarglacier, which includes the confluence area, was modelled. At the three cross sections, up-stream and down-stream of the confluence area, stresses were applied as boundary conditions. All cross-sections were approximated by ellipses, and the analytical solution for flow in a slightly elliptical channel was used to obtain an estimate of the stress tensor (Nye, 1965). At first the change in longitudinal velocity and the magnitude of stress gradients close to the edges was used as a measure of the correctness of the inflow boundary conditions. It then turned out to be necessary to introduce some additional multiplying factors to the applied stresses (that were dependent on n) in order to ensure a smooth variation of the calculated fields towards the cross-sectional boundaries. The whole procedure was, however, unsatisfactory, and it was concluded that additional information on the velocity field close to the cross-sectional boundaries was needed to test the correctness of the applied stress distribution.

During the winter of 1991/1992 no markers were situated at locations close to the boundaries of the numerical model, making direct verification of the boundary conditions difficult. In the autumn of 1992 some additional markers were therefore installed at locations further upwards and downwards of the confluence than before. The smooth variation of the calculated stresses and strain rates towards all three cross-sections finally obtained, as well as the agreement with the measured surface-velocity variation at the corresponding locations, was taken as proof of the correctness of the cross-sectional boundary conditions.

5.3 Comparison of calculated and measured surface velocities

Numerically calculated surface velocities were compared with the measured marker velocities to optimize the values employed in the flow law and to test for systematic deviations. This type of comparison also tests the correctness of the (glacier bed) boundary conditions used.

Since no velocities were prescribed as boundary conditions, calculated velocities depend linearly on A. This was indeed the main reason for using stress type cross-sectional boundary conditions. It therefore suffices to calculate them for one particular A. The "best" value of A can be found afterwards by comparing scaled calculated velocities with measured ones, and asking how the calculated values have to be scaled to give the best possible agreement with measurements. If, for example, A_c was the value of A used for a calculation that gave the velocity field $\mathbf{v}^c(x, y, z)$, the best value of A could be defined to be A_b, with $A_b = f_A A_c$, where f_A is a scaling factor found by minimising the standard deviation s_v of the velocities

$$s_v^2 := \frac{1}{N} \sum_{i=1}^{N} (\mathbf{v}^m(\mathbf{r}_i) - f_A \mathbf{v}^c(\mathbf{r}_i))^2, \tag{5.1}$$

where $\mathbf{v}^m(\mathbf{r}_i)$ are measured velocities at the points $\mathbf{r}_i$, and N is the total number of points where measured velocities are available. A_b will then be the value of A, for some particular value of n, that minimizes the root-mean-square error between calculated and measured velocities. f_A is given by

$$f_A = \frac{\sum_{i=1}^{N} \mathbf{v}^m(\mathbf{r}_i)\mathbf{v}^c(\mathbf{r}_i)}{\sum_{i=1}^{N} \mathbf{v}^c(\mathbf{r}_i)\mathbf{v}^c(\mathbf{r}_i)}. \tag{5.2}$$

The *normalized root-mean-square error* (S_v) is defined as

$$S_v := \sqrt{\frac{\sum_{i=1}^{N} (\mathbf{v}^m(\mathbf{r}_i) - f_A \mathbf{v}^c(\mathbf{r}_i))^2}{\sum_{i=1}^{N} \mathbf{v}_i^m \mathbf{v}_i^m}}. \tag{5.3}$$

The normalized difference between the measured and the (scaled) calculated velocity vector at the position of marker i is

$$\mathbf{R}_i := (\mathbf{v}_i^m - f_A \mathbf{v}_i^c)/v_i^m \tag{5.4}$$

where $\mathbf{R}_i$ is the dimensionless *error vector*, and the subscript i refers to the i-th marker. The length of the sum of all error vectors is a measure of the systematic errors. This sum is denoted by $\mathbf{R}$, *i.e.*

$$\mathbf{R} := \frac{1}{N} \sum_{i=1}^{N} \mathbf{R}_i \tag{5.5}$$

The best value (A_b) of A, found by minimizing expression (5.1), is listed in Table 5.1 together with the normalized root-mean-square error (S_v), and the length R of the total sum ($\mathbf{R}$) of the error vectors. Winter velocities were used. All velocities were obtained from repeated surveying of markers with time intervals larger than one month. These velocities were, as explained in Sec. 3.3, constant throughout two winters. Velocities based on repeated surveying with time interval of 3 to 4 days were not used, since the errors of the resulting velocity gradients were considered to be too large. For markers that had been surveyed more than twice, averaged velocities were used.

n	A_b [$\mathrm{a^{-1}bar^{-n}}$]	S_v	R
1	0.060	0.13	0.029
2	0.069	0.13	0.0097
3	0.075	0.11	0.0058
4	0.078	0.13	0.015
5	0.081	0.14	0.023

Table 5.1: A_b was found by minimising the root-mean-square error between measured marker velocities and calculated velocities, and is thought to represent, in this sense, the best possible value of A. A and n are parameters in Glen's flow law. For $n = 3$, A_b is less than one-half of the value often recommended in the literature, which is $0.167\,a^{-1}$ bar^{-3} (Paterson, 1981). The normalized root-mean-square error S_v is almost constant and rather large, or about 12%. This corresponds to s_v (defined in text) being approximately 4 m/a, where maximum velocities where approximately 35 m/a. R is the length of the sum of all error vectors R_i. It is a measure of systematic errors. R is smallest for $n = 3$. A total number of 39 velocity measurements was used, *i.e.* $N = 39$.

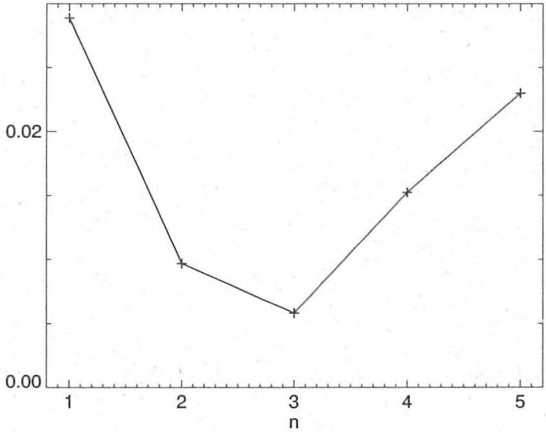

Fig. 5.3: R as a function of n. R is the length of the sum of the error vectors $\mathbf{R}_i$ defined in text. R is smallest for $n = 3$. As explained in text, do systematic errors however remain.

As Fig. 5.3 shows, R is a convex function of n with a minimum at $n = 3$, suggesting that $n = 3$ is the best estimate of n. If N random vectors having length l are added together, their sum will, on average, have the length $\sqrt{N}l$. The medial length of $\mathbf{R}_i$ was 0.18 and $N = 39$, so that a pure statistical variation is expected to give $R \approx 0.18/\sqrt{39} = 0.016$, which is almost twice as larger as the value of R obtained for $n = 3$. This is only a rough estimate of the contribution of random errors to the length of $\mathbf{R}$, since not all $\mathbf{R}_i$ had the same lengths. A comprehensive study of the errors involved has not been made, since it would require a good estimate of the measurement errors involved, which is not available.

A simple estimate of the errors involved can, however, be obtained by using different numbers of marker velocities to calculate the variation of R with respect to n. Several calculation made by using only 80% of the measured velocity vectors, revealed that although the shape of the $R(n)$ curve changes somewhat, the minimum is always at $n = 3$.

The error vectors $\mathbf{R}_i$ for $n = 1$ to $n = 5$ can be seen in Figs. 5.4 to 5.8.

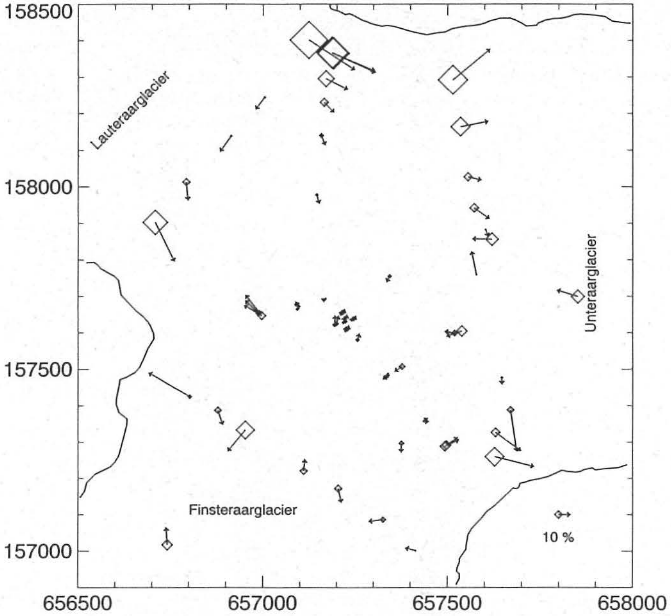

Fig. 5.4: Difference between measured and calculated surface velocities for $n = 1$. Vectors represent a vector quantity $\mathbf{R}_i$ defined by $\mathbf{R}_i := (\mathbf{v}_i^m - f_A \mathbf{v}_i^c)/v_i^m$, where f_A was found by minimising $\sqrt{\sum_i (\mathbf{v}_i^m - f_A \mathbf{v}_i^c)^2}$. The subscript i refers to the i-th marker. $\mathbf{v}_i^m$ are measured velocities of markers, and $\mathbf{v}_i^c$ are calculated velocities. f_A gives information on what would have been the best value (in an average sense) of A to use for the numerical calculations. Systematic changes in the orientation and the magnitude of the vectors do not depend on the value of A, but indicate that a wrong flow law, or a wrong type of boundary conditions, were used. The size of the diamond symbols is proportional to the length of P_i, defined to be the projection of $\mathbf{R}_i$ on $\mathbf{v}_i^c/v_i^c$, *i.e.* $P_i := \mathbf{v}_i^c(\mathbf{v}_i^m - f_A \mathbf{v}_i^c)/(v_i^m v_i^c)$. If $\mathbf{R}_i$ is transversal to the calculated flow vectors, P_i is zero. Coordinates are in meters and those of the official Swiss coordinate system. North points upward.

In addition the projection P_i of $\mathbf{R}_i$ on $\mathbf{v}_i^c/v_i^c$ is shown as a diamond symbol. P_i gives

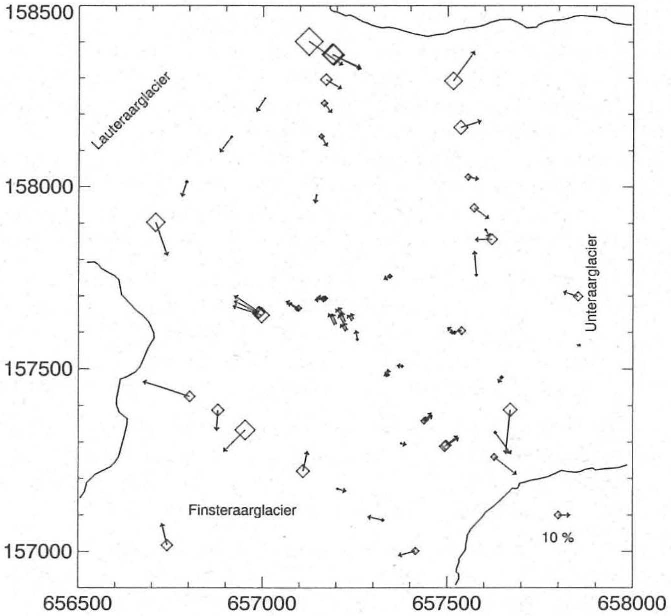

Fig. 5.5: Difference between measured and calculated velocities for $n = 2$.

a information about the error in longitudinal velocities.

Markers along the two profiles running across the Lauteraar and Finsteraarglacier above the confluence and the profile across the Unteraarglacier below the confluence area, were only measured twice with a time interval of approximately 4 days. The associated errors in the velocities are correspondingly large. Since the surveying errors are estimated to be about 3 cm, the errors of the velocities are about 4 m/d. The markers along the lines that run from the junction point and the two marginal zones of the confluence towards its center, were, on the other hand, measured repeatedly with time intervals of approximately 40 days, and the errors are correspondingly much smaller.

The most conspicuous feature of Figs. 5.4 to 5.8 is the *systematic change* of $\mathbf{R}_i$ across the glacier (*cf.* for example Fig. 5.5) for those markers that were measured over a long period of time (more than a month). Conversely, the variation of the error vectors of the markers measured over a short period of time (3 to 4 days) is more or less random. The conclusion is that no value of n and A gives a perfect fit to the data, *i.e.* systematic errors always remain. The discrepancy between calculated and measured surface velocities is, however, too small to be reflected in the error vectors of the marker measured over time period of only four days. In what follows only the variation of the error vectors based on the long interval measurements will be discussed.

The error vectors are in general shortest at the center of the confluence and increase towards the margins. This is to some extent caused by the higher-than-average spatial density of markers near the location of the bore holes, assigning that area a larger weight in the determination of f_A. The systematic change in the orientation of $\mathbf{R}_i$, however, exemplifies the presence of non-random errors. This finding undermines the importance of the conclusion drawn from Fig. 5.3. Using $n = 3$ only minimizes the systematic errors but does not eliminate them. Different measures of the errors, for example using absolute errors and not relative ones, do not affect this conclusion.

On the other hand the errors are usually less than about 15%, which is probably sufficient for most modeling purposes. Since the general flow characteristic of the confluence area form the main focus of this study, an error of this magnitude is quite acceptable. The systematic deviations, however, show unambiguously that the "best" values for A and n given above, cannot be extrapolated to other glaciers.

For $n = 1$ (*cf.* Fig. 5.4) the largest errors are found at the north margin of the confluence. The error vector points approximately in the flow direction. The (scaled) calculated velocities are therefore, at that location, smaller than the measured ones. For the marker closest to the junction point the situation is reversed.

For $n = 2$ (*cf.* Fig. 5.5) the error vectors at the north and the south margins point more or less in the flow direction, and the vectors along the medial line in the reversed direction. Qualitatively the same picture is found for $n = 3$ to $n = 5$ (*cf.* Figs. 5.6, 5.7, and 5.8). The orientation of the error vectors at the north and the south sides of the confluence is hence consistently opposite to the orientation close to the junction point.

At the north and south margins the deformation pattern is close to simple shear, whereas along the medial line there is a strong extension with negligible amount of shear. This suggests that Glen's flow law does not give the change in the effective ice viscosity correctly, as the stress regime changes from pure shear ($\sigma'_{ij} = 0$, if $i = j$), to no shear ($\sigma'_{ij} = 0$, if $i \neq j$).[2] The strong correlation of the orientation and the magnitude of the error vectors with the strain regime, is taken as a clear indication that the discrepancy, between measured and calculated values, is caused by the flow law and not by inappropriate boundary conditions.

It is concluded that no value of n gives results devoid of systematic variations. $n = 3$ is simply the lest unacceptable of a number of unsatisfactory alternatives. Notice that for $n = 3$ the errors are distributed almost symmetrically about the medial line. For $n < 3$ the errors tend to be larger along the north than the south margin; for $n > 3$ it is the other way around. For $n = 5$ the only significant errors are close to the junction point and at the south margin, but there is still a clear tendency of calculated marginal velocities to be smaller than measured ones. With respect to the centerline the error distribution for $n = 5$ is the opposite to that for $n = 1$.

---

[2] The original measurements of Glen (Glen, 1952; Glen, 1955) were made with a stress state of uniaxial compression. They were generalized to a 3D stress configuration by Nye (1953, 1957).

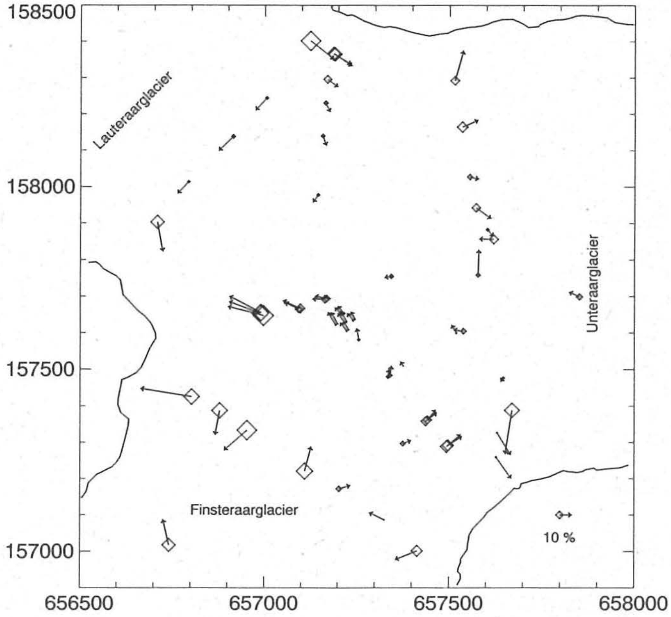

Fig. 5.6: Difference between measured and calculated velocities for $n = 3$.

It is further concluded that the errors in the (scaled) velocity field are sufficiently small to justify the use of Glen's flow law with the parameters given in Table 5.1. Since the main goal of the 3D modeling is to elucidate the general flow characteristics of a confluence, and to test the corresponding theoretical predictions made in Chapter 4, calculations will be made for various values of n although (systematic) errors are smallest for $n \approx 3$.

It is tempting to resort to a different type of flow law to reduce or eliminate the systematic discrepancy. The limited number of marker velocities and the lack of measurements of bore-hole deformations, however, makes such an undertaking highly questionable. There is no doubt that a sufficiently long trial and error procedure will give a flow law producing better results, but the agreement could be purely fictitious. Only with better knowledge of the velocity variation with depth, together with comprehensive surface velocity measurements, and with information on the spatial variation of factors such as debris content and crystal orientation (to name a few), can one hope to obtain somewhat reliable information on the rheological behavior of glacier ice. Until then one has to work with locally adjusted parameters, usable only for some particular glacier, or some particular section of one glacier.

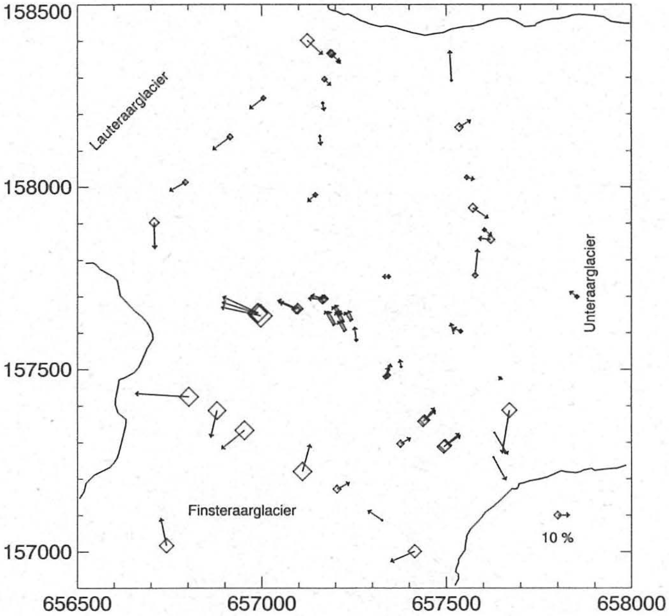

Fig. 5.7: Difference between measured and calculated velocities for $n = 4$.

5.4 Surface velocities

5.4.1 Horizontal surface velocities

Horizontal velocities for $n = 1$ and $n = 3$, and for the corresponding values of A from Table 5.1, can be seen in Figs. 5.9 and 5.10. Vectors represent the v_x and v_y components of the velocity field, and contour lines the horizontal speed $v_h := \sqrt{v_x^2 + v_y^2}$. These figures should be compared with Fig. 3.13 that shows measured winter velocities. Among common features of Figs. 5.9 and 5.10 is a local maximum of horizontal velocity somewhat below the confluence center, that surface velocities of the Finsteraarglacier are larger than those of Lauteraarglacier, and a velocity decrease as both tributaries enter the confluence. This velocity pattern is consistent with measurements (*cf.* Fig. 3.13).

The largest transversal velocity gradients are found at the confluence marginal zones. Longitudinal velocity gradients along the medial line close to the junction point are notably small.

Maximum horizontal speeds are not always found along the glacier's geometric centerline. Where the valley geometry forces the velocity vectors to rotate rightwards

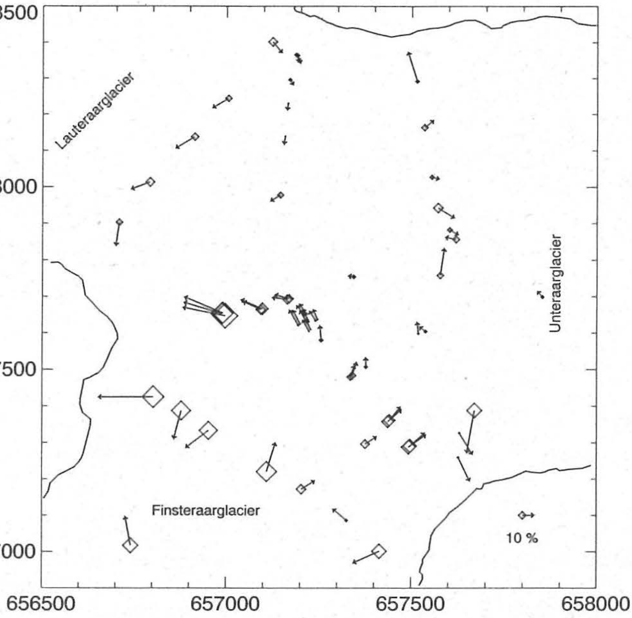

Fig. 5.8: Difference between measured and calculated velocities for $n = 5$.

in down-flow direction, the maximum speed is shifted towards the north margin (towards the outside of the bend), and where the velocity vectors rotate to the left, the maximum shifts towards the south margin (again towards the outside of the bend). Similar effects of the curvature of the flow-lines on the position of the velocity maximum have for example been observed on the Blue Glacier (Meier *et al.*, 1974; Echelmeyer, 1983; Echelmeyer and Kamb, 1987). Echelmeyer and Kamb (1987) performed a numerical and analytical study of the flow in curved channels, and found the stress centerline in a curving parabolic channel to be shifted towards the inside margin. The position of the maximum velocity, on the other hand, may be shifted towards the inside or the outside of the geometric centerline depending upon n and the curvature of the channel. For the Unteraarglacier the direction of the calculated velocity shift was always towards the outside of the bend for all values of n. The density of marker measurements on the Unteraarglacier is not large enough to detect this effect.

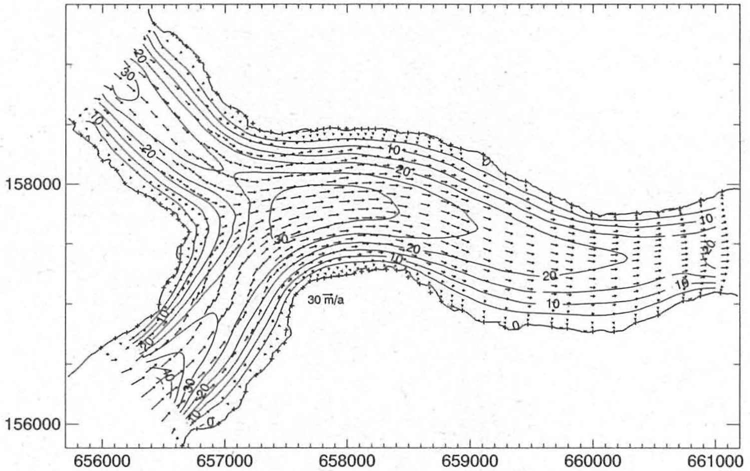

Fig. 5.9: Calculated horizontal surface velocities for $n = 1$ and $A = 0.060\,\mathrm{a}^{-1}\mathrm{bar}^{-1}$. The surface of the whole model is shown. Vectors represent horizontal velocities v_x and v_y, and contour lines horizontal speed. The contour interval is 5 m/a. Coordinates are in meters. North points upwards. The boundaries are based on a digital terrain model. The plus symbols give the locations of the boundary nodes of the FE model.

5.4.2 Vertical surface velocities

Vertical surface velocities for $n = 1$, $n = 3$, and $n = 5$, with corresponding values for A from Table 5.1 are depicted in Figs. 5.11, 5.12, and 5.13. Positive values represent upward movements.

There is a narrow zone of relatively large downward movements running from the junction point down the entire Unteraarglacier, that coincides with the medial moraine. Except for the zone in the immediate vicinity of the junction point, where there is a few-meters-deep surface depression, these negative vertical velocities are the expression of the disintegration of the medial moraine, and are caused by its higher elevation with respect to the surrounding ice.

The highly negative vertical velocities close to the junction coincide with a surface depression. Since a surface depression would be expected to cause upward movements in the same way as the higher-than-average elevation of the ice-cored medial moraine results in downward movements, these negative velocities must result directly from the dynamics of the confluence. Within the context of the map-plane model discussed in Sec. 4.2, these negative movements can be understood to be caused by the change in boundary conditions at the junction point (J), and the associated pressure drop. A sharp increase of the medial line velocities would cause the zone of high pressure drop to be strongly localized. The velocity increase is

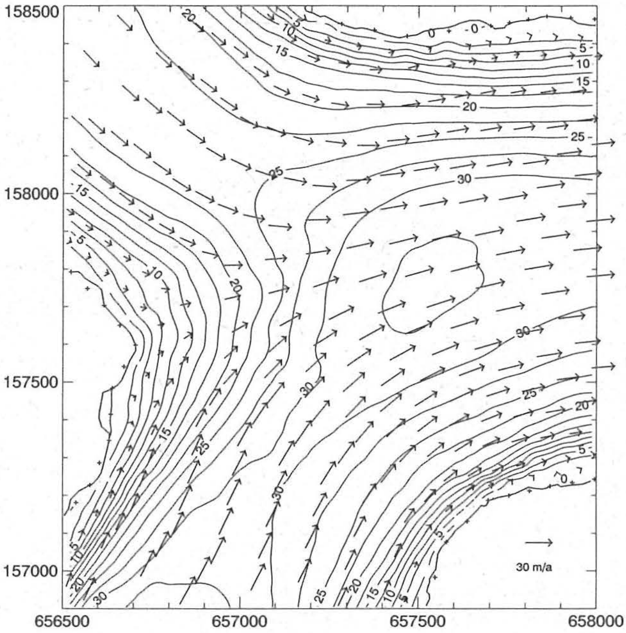

Fig. 5.10: Calculated horizontal surface velocities for $n = 3$ and $A = 0.075\,\mathrm{a^{-1}bar^{-3}}$. Only a part of the model is shown. Vectors represent horizontal velocities v_x and v_y, and contour lines horizontal speed. The contour interval is 5 m/a. Coordinates are in meters. North points upwards. The boundaries are based on a digital terrain model. The plus symbols give the locations of the boundary nodes of the FE model.

indeed sharp and gets sharper with increasing n, as can be seen in Fig. 5.14, which depicts v_x and v_z at the surface as functions of the distance from the junction point. The strain rates and the deviatoric stresses are consequently large. The FE mesh is, however, clearly too coarse to give an exact estimate of the vertical velocities, since the (negative) vertical velocity maximum is obtained at the FE node lying closest to J. A further mesh refinement would presumably move the maximum even closer to J and give larger negative values. Calculations with a coarser mesh (2800 elements instead of 6424) also showed the position and the magnitude of the maximum to depend on the level of mesh refinement. The slope of the horizontal velocity profile (Fig. 5.14) did, on the other hand, not depend significantly on the number of elements used. And there is no indication that the slope becomes infinite at J, as happens at an exact no-slip/free-slip transition (*cf.* Sec. 4.2.3). This is taken as an indication that the change in boundary conditions is sufficiently smooth to depress the singularity in longitudinal and transversal strain rates and to give a finite increase in longitudinal velocities at the junction point.

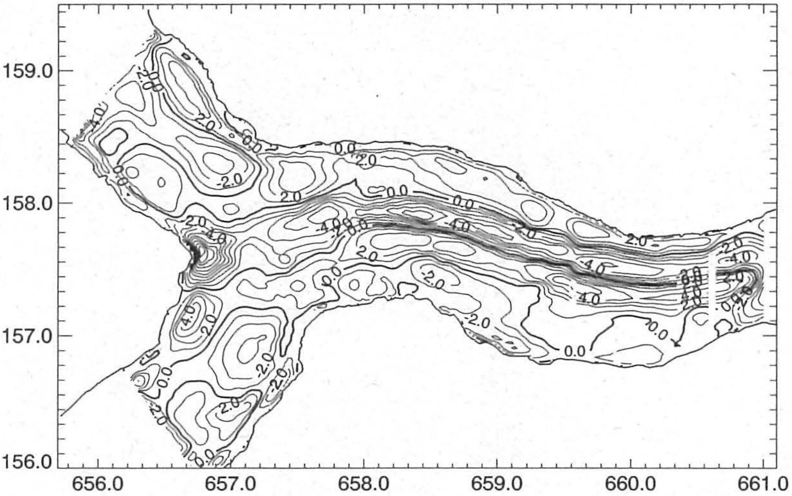

Fig. 5.11: Calculated vertical surface velocities for $n = 1$ and $A = 0.060\,\mathrm{a^{-1}bar^{-1}}$. The surface of the whole model is shown. The contour interval is 1 m/a. Coordinates are in km. North points upwards.

Since vertical velocities along the ice-cored medial moraine are always negative, the dynamics of the confluence cannot be considered to be directly responsible for its creation. It is clear that the change in boundary conditions at J and the converging of the two tributaries does not pile up ice; rather the contrary: it causes a strong local surface depression. The differential ablation of the debris-covered marginal ice of the two tributaries, that is transferred at the junction point towards the centerline, and the adjacent clean ice must be the sole cause of the moraine ridge. The dynamics of the confluence counteract this process and only at some distance below the junction point, where the effect of differential ablation starts to dominate the strong downward movements, does the ice-cored medial moraine start to form. The surface debris does not immediately give rise to a medial moraine as described by Gomez and Small (1985) in their model of ice-stream interaction moraines. Further down-stream from the junction point differential ablation is needed to maintain the form of the medial moraine against the disintegration effects of glacier flow.

The magnitude of the negative vertical velocities along the medial moraine is quite dependent on n, and decreases with increasing n. This can be understood to be a consequence of the fact that the stresses causing these movements are much smaller than the driving stresses. Using A from Table 5.1 gives, for a pure shear of approximately 0.8 bar, the same shear strain rate for all values of n. This of course results from the fact that A was determined in such a way as to give as-close-as-possible overall agreement between measured and calculated velocities, and that the cause of

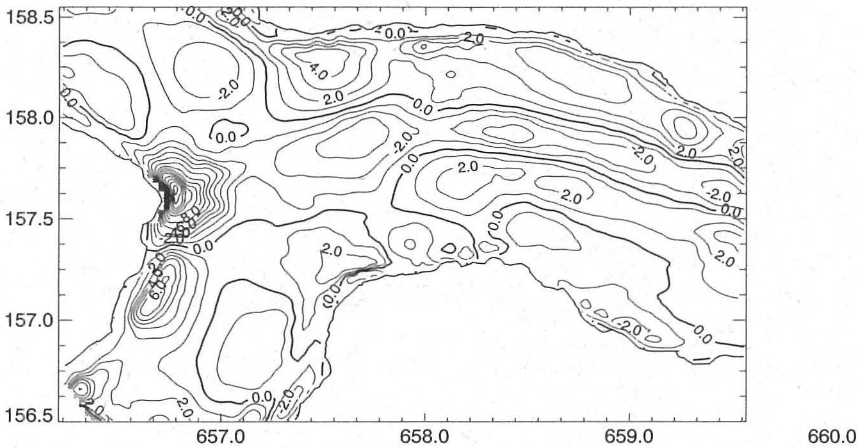

Fig. 5.12: Calculated vertical surface velocities for $n = 3$ and $A = 0.075\,\mathrm{a}^{-1}\mathrm{bar}^{-3}$. Only a part of the model is shown. The contour interval is 1 m/a. Coordinates are in km. North points upwards.

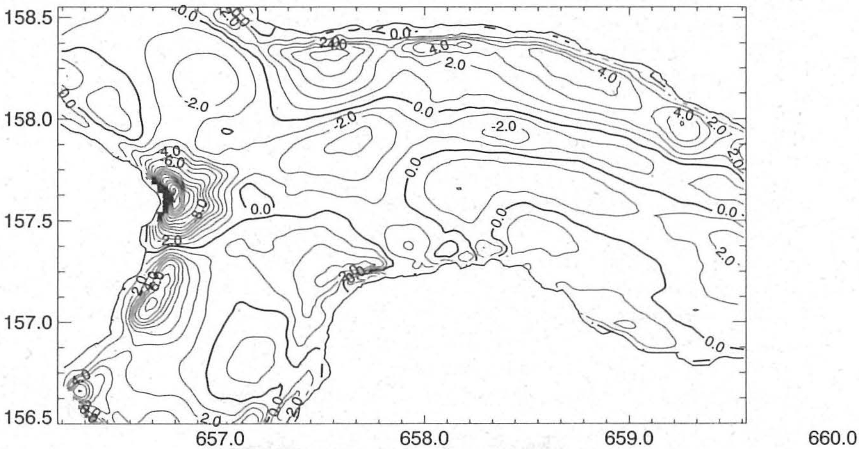

Fig. 5.13: Calculated vertical surface velocities for $n = 5$ and $A = 0.081\,\mathrm{a}^{-1}\mathrm{bar}^{-5}$. Only a part of the model is shown. The contour interval is 1 m/a. Coordinates are in km. North points upwards.

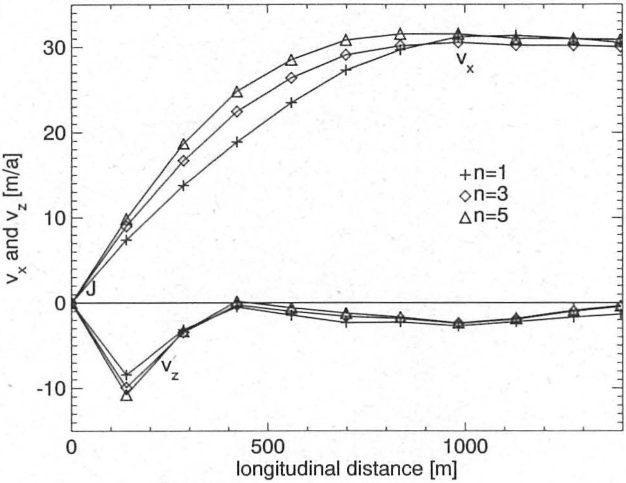

Fig. 5.14: Calculated velocity profile along the surface from the junction point (denoted by J in the figure) towards the center of the confluence. The profile is approximately along a flow line. Velocity gradients increase with n. The negative velocity peak in v_z coincides with a surface depression, and is caused by the dynamics of the confluence. The negative velocities further away from the junction point are associated with the disintegration of the medial moraine. Symbols represents FE nodes. Calculations with different mesh refinements showed the location and the magnitude of the negative vertical velocity maximum to depend on the level of mesh refinement. The slopes of the horizontal velocity are, on the other hand, produced with a sufficient numerical accuracy to conclude that they are finite.

the observed movements is a driving stress of ≈ 0.8 bar. For smaller/larger stresses the strain rates decrease/increase with increasing n. Detailed measurements of the vertical and the transversal velocities across the medial moraine could therefore give information on the rheological behavior of ice at stresses far less than the typical driving stresses, and would so strongly complement measurements of longitudinal velocities. This also indicates that the calculated values of the vertical movements of the medial moraine must be used with care, since the rheological parameters used (Table 5.1) were tuned with respect to surface velocities that are caused by much larger stresses. Still, the vertical velocities at the top of the medial moraine are always larger than 1 m/a, indicating that without differential ablation the moraine would disappear within 20 years, in which time it would have traveled less than 700 meters.

The peak of the negative velocity zone in the immediate vicinity of the junction increases in magnitude with increasing n. The stresses responsible for these large velocities must therefore be larger than the overall driving stress.[3] There is also

---

[3] For a valley glacier the usual definition of the driving stress as $\tau_b = \rho g h \sin\alpha$ is inappropriate. A better definition is $\tau_b = \frac{1}{2}\rho g h \sin\alpha$ which gives, for the Unteraarglacier, $\tau_b \approx 0.8$ bar.

a tendency for the zone to become more localized, but the coarseness of the FE mesh makes it difficult to make a definitive statement in this respect. On the basis of the numerical calculations discussed in Sec. 4.2.3 this is, however, the expected behavior.

On the basis of the analytical solution of the map-plane model (*cf.* Sub-sec. 4.2.2) one expects the anomalous flow not only to cause a local surface depression at J but also to pile up ice at the margins of the two tributaries facing the junction point. The resulting super-elevated zone should have spatial dimensions considerably larger than those of the surface depression. In fact a number of zones displaying positive vertical velocities can be seen.

First of all one finds a zone of positive vertical velocities on the north-west side of the Finsteraarglacier, about 500 m upward from the junction point. The cause of this velocity anomaly, which increases in magnitude with n, is not clear, but it is presumably caused by the shape of the bedrock and the decreased marginal ice thicknesses at the junction (*cf.* Fig. 3.1 and Fig. 3.4), that will act to reduce the ice velocities. There is a corresponding albeit smaller, velocity anomaly on the south-west side of the Lauteraarglacier.

On the north and the south side of the confluence, diametrically opposite to the negative vertical velocity anomaly of the junction point, one finds two positive vertical velocity anomalies (*cf.* Fig. 5.15). With increasing n their magnitude increases. For $n = 1$ they are hardly noticeable (+ 3 m/a on the north side, +2 m/a on the south side) but can be seen quite clearly for $n \geq 3$. There are no apparent changes in bedrock geometry or ice thicknesses that could be causing these anomalies. Nor are these anomalies are caused by lower than average elevation, on the contrary they are associated with unexpectedly high elevations that cause a tilting of the contour lines towards the junction. It can therefore be concluded that the dynamics of the confluence themselves are responsible for the anomalies, and that they in turn cause the super-elevated zones. Within the context of the conceptual models introduced in Sec. 4.2 they can be seen to be expressions of the recirculation set up by the change in boundary conditions at J.

Fig. 5.15 summarizes the velocity anomalies caused by the confluence dynamics, and which are not just a result of surface processes such as differential ablation. The plus signs denote upward movements, and the minus sign denote downward movements. The solid lines give the approximate spatial extent of the zones that were seen in the 3D model and that can be understood with the help of the conceptual models in Sec. 4.2. These zones are considered to be universal, *i.e.* they should be found in all confluence areas (neglecting velocity variations caused by local topographic features such as moraines). The dashed lines border zones were found with the 3D model, but are possibly caused by some unique features of geometry of the particular confluence modelled, such as the particular geometry of the bed.

5.5 The 3D velocity and stress fields

The graphical presentation of 3D flow fields poses some difficult problems. After various attempts it was concluded that the best way of displaying the result is with

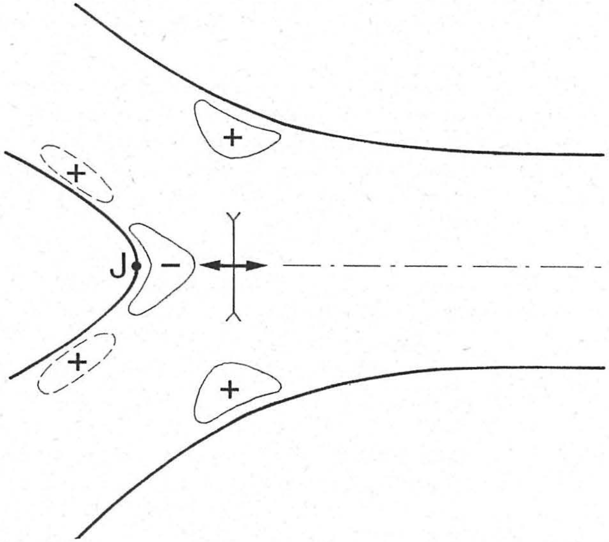

Fig. 5.15: Vertical velocity anomalies of the 3D model. Plus symbols denote zones of larger than average upward velocities, and minus symbols a zone of downward velocities. The dashed lines mark the approximative spatial extent of velocity anomalies found with the 3D-model that cannot be explained with the help of the conceptual map-plane model introduced in Chapter 9, and the solid lines those anomalies that did result from that model. The zones boarded by the solid lines are considered to be of universal nature and are expected to found at all glacier confluences. They should manifest themselves in the form of higher than average elevation, although processes such as differential ablation may sometimes make their observation difficult.

the use of colored 3D-isosurfaces.

5.5.1 Vertical velocities

Isosurfaces of vertical velocities for $n = 1$, $n = 3$, and $n = 5$ are displayed in Figs. 5.16, 5.17 and 5.18.

In all figures one can clearly see the strongly localized zone of negative (downward) velocities at the junction point J, which is caused by the dynamics of the confluence and which is associated with a local surface depression. In the immediate neighborhood of to the junction point, the maximum of the negative vertical velocities is found at the surface. Several hundred meters further in the down-flow direction, close to the location of the bore holes drilled in autumn 1991, the maximum is not at the surface but at a depth corresponding approximately to one half of the glacier thickness. The downward movements at these great depths disappear below the confluence center. They are clearly caused by the strong glacier thickening along those flow lines that lie close to J. Below the confluence center the glacier has adjusted to the new bed geometry and the divergence of the flow-lines over the depth and the associated vertical velocity components are strongly reduced.

Also clearly identifiable in the figures is the line of negative velocities running from J down the whole glacier and coinciding with the medial moraine, which is (as said above) an expression of its disintegration through glacier flow. On both adjacent sides of the medial moraine vertical velocities are positive. To the south of the moraine (to the left in the figures) the upward movements are especially large. There the ice is practically free from supra-glacier debris cover, and the differential ablation forms a mild surface depression. Since the whole area of the glacier shown is within the ablation zone[4], emerging velocities are on average positive. (The glacier has a mean slope of about 4°.)

5.5.2 Strain rates

The zones of positive vertical velocities caused by the change in boundary conditions at J (*cf.* Fig. 5.15) are hardly identifiable for $n = 1$, but for $n = 3$, and especially for $n = 5$, they can clearly be seen. The vertical velocities are positive throughout the whole glacier thickness, but the maximum obtains at the surface. At these locations one therefore expects positive vertical strain rates close to the surface. That this is the case can be seen in Fig. 5.21 which depicts the positive isosurfaces of $\dot{\epsilon}_{zz}$ in the confluence area. In fact the largest positive values of $\dot{\epsilon}_{zz}$ within the whole confluence are found there (yellow colors). At the confluence center, and where the vertical strain-rate profile in Fig. 3.10 was measured, relatively large positive values are also found. Fig. 5.21 clearly demonstrates the large spatial variability of $\dot{\epsilon}_{zz}$. Positive values are limited to the upper sections of the confluence area.

Fig. 5.19 gives the vertical strain rates $\dot{\epsilon}_{zz}$ for $n = 1$, and Fig. 5.20 those for $n = 3$. The vertical strain rate usually increases with depth and then decreases again. Notice that because of the no-slip condition at the bed, $\dot{\epsilon}_{zz}$ must there be close to zero if the slope of the glacier bed is small. Only close to the junction point, where the slope of the bed in flow direction is large, can one expect to find large vertical strain rates at great depths.

The effect of the medial moraine on $\dot{\epsilon}_{zz}$ is to cause a zone of vertical compression directly below it that extends throughout the whole glacier thickness. The maximum is obtained at a depth of approximately 70 m depth below the peak of the moraine. The isosurfaces thus have the form of tubes. The maximum is much more pronounced for $n = 1$ than for $n > 1$.

Close to the center of the confluence the tube dips downwards in the up-flow direction, and reappears at the surface at the junction point. At the confluence center vertical strain rates are therefore positive close to the surface, in spite of the presence of the ice-cored moraine. There the ice experiences a vertical extension (*cf.*

---

[4] There are no direct measurements of the ablation rates, but they can be expected to lie in the range of 2 to 5 meters per year.

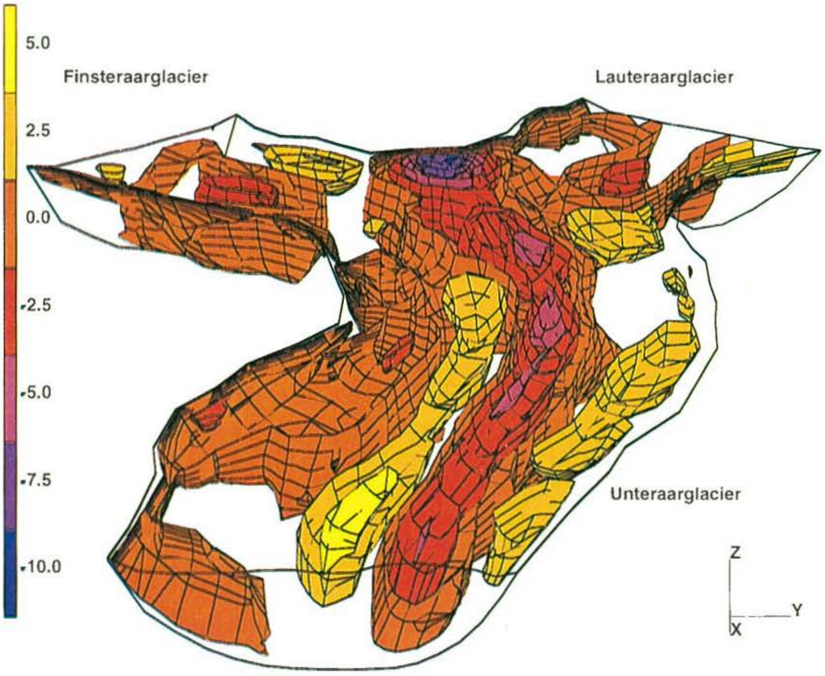

Fig. 5.16: Isosurfaces of vertical velocities v_z, for $A = 0.060\,\mathrm{bar}^{-1}\mathrm{a}^{-1}$ and $n = 1$ in the units m/a. North is approximately to the right.

Fig. 5.21). Close to the surface and close to the junction point vertical strain rates are negative (*cf.* Fig. 5.22). This can be understood, as explained in Sec. 4.1, to be a consequence of the ice thickening in the down-flow direction along flow-lines running close to J and of the no-slip condition.

That the negative vertical strain rates close to the junction point are caused by the ice thickening in flow direction can also clearly be seen in Figs. 5.23, 5.25, and 5.27, that show $\dot{\epsilon}_{zz}$ along a vertical section running from the junction point towards the center of the confluence. The section is approximately along a flow-line. B denotes the position of the bore holes drilled in autumn 1991. Note that the vertical strain-rate pattern is not strongly dependent on n. There is excellent qualitative agreement between measured and calculated vertical strain-rate variations. At the surface $\dot{\epsilon}_{zz}$ is positive, decreases with depth, becomes negative at a depth below the surface corresponding to about 3/5 of the glacier thickness, and increases in magnitude

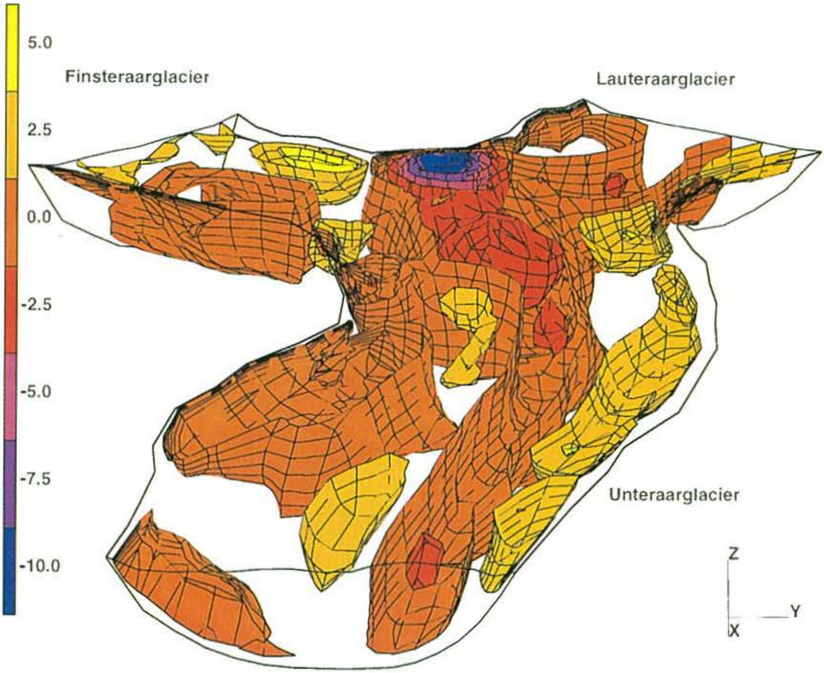

Fig. 5.17: Vertical velocities v_z, for $A = 0.075\,\text{bar}^{-3}\text{a}^{-1}$ and $n = 3$ in the units m/a.

towards the glacier bottom, where the maximum negative strain rates are obtained.

Quantitatively the calculated values close to the bed-rock are somewhat too small. The calculated curve in Fig. 3.10 is, however, the slope of the curve in Fig. 3.9, which is based on only four vertical velocity measurements. It is hence concluded that the qualitative agreement is as good as can be expected and that the discrepancies found could just as well have been caused by the rather limited vertical resolution of the measured data as by errors associated with the model calculations.

The model predicts a strong variability of the vertical strain rates in all three spatial directions. Measurements of $\dot{\epsilon}_{zz}$ therefore provide an effective means of testing its prediction and pointing the way to further improvements.

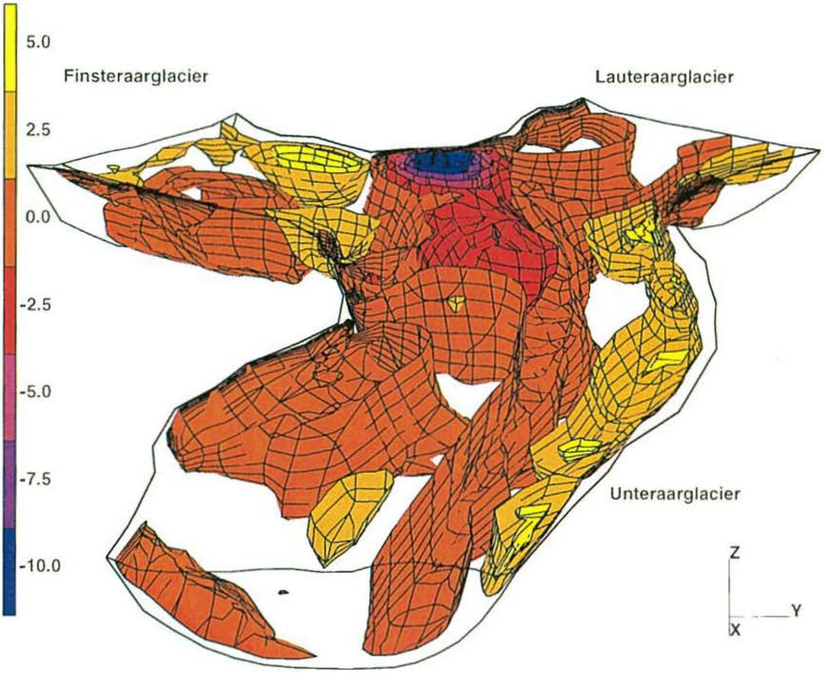

Fig. 5.18: Vertical velocities v_z, for $A = 0.081\,\mathrm{bar}^{-5}\mathrm{a}^{-1}$ and $n = 5$ in units of m/a.

5.5.3 Stresses

Isosurface of the von Mises stress σ_M of the confluence for $n = 3$ are depicted in Fig. 5.29. The von Mises stress is defined as

$$\sigma_M := \left(\frac{3}{2}\sigma'_{ij}\sigma'_{ij}\right)^{1/2} \tag{5.6}$$

Note that $\sigma_M = \sqrt{3\sigma'_{II}} = \sqrt{3}\tau$, where τ is the effective stress.

The smallest stresses are found along the centerline. Where the ice enters the confluence the stresses across the glacier surface increase somewhat and then decrease again, so that a local minimum of σ_M is found at the surface of the center of the confluence. Stresses increase from the centerline towards the margins and the deepest-lying sections of the bed. Friction from the margins strongly affects the flow.

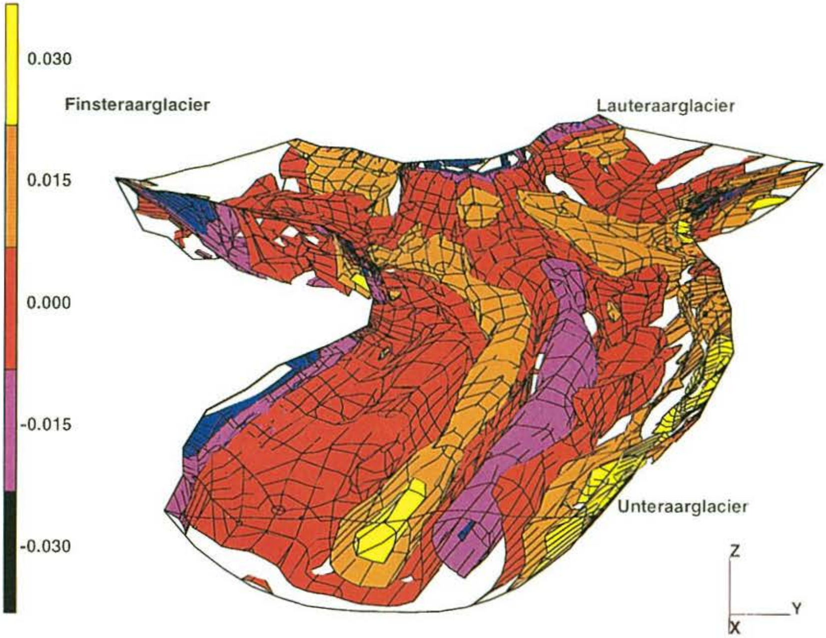

Fig. 5.19: Vertical strain-rate isosurfaces for $n = 1$. Units are 1/a.

There is a local maximum of σ_M in the immediate neighborhood to the junction point. This stress concentration is nevertheless not exceptionally high and equally high values of σ_M are found diametrically opposite to the junction point. This can be seen in Figs. 5.30 and 5.31, which depict the von Mises stress along the bed-rock interface for $n = 1$ and $n = 5$, respectively. The local stress maximum at J is strongly localized. The regions of high effective stress lying diametrically opposite to J are much larger in extent. Note that the center sections of the confluence bed do not display high effective stresses.

With increasing n, the stress variation along the bed becomes more uniform in the sense that the difference between maximum and minimum effective stresses gets smaller. For $n = 1$, σ_M lies in the range of 0.2 bar to 2.2 bar and for $n = 5$ between 0.7 and 1.7 bar. The average effective stress is approximately 1 bar.

The von Mises stress along the glacier surface for $n = 1$ and $n = 5$ can be seen in Figs. 5.32 and 5.33.

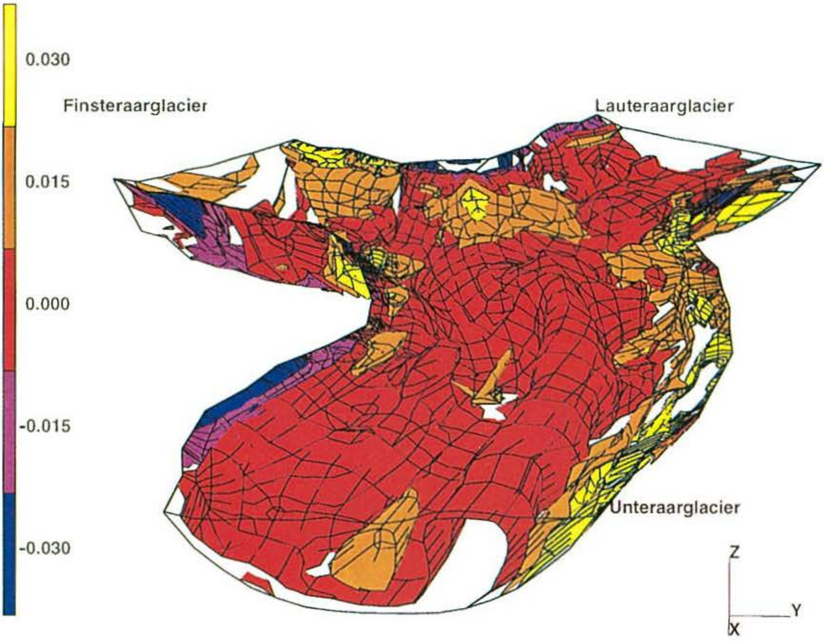

Fig. 5.20: Vertical strain-rate isosurfaces for $n = 3$. Units are 1/a.

For $n = 1$ a strongly localized maximum is found in the immediate vicinity of to the junction point (*cf.* Fig. 5.33). This maximum is not seen to the same extent for $n = 5$ (*cf.* Fig. 5.33). The numerical calculations of a no-slip/free-slip transition discussed in Sec. 4.2.3 showed the maximum of strains and stresses to move towards J with increasing n. Since the stress maximum seen in Fig. 5.32 for $n = 1$ is on the verge of the spatial resolution of the FE mesh, it cannot be concluded that there is no corresponding maximum for $n = 5$. In fact the maximum could be detected for $n = 2$ and was found to be lying closer to J than it did for $n = 1$. For $n \geq 3$ the maximum could not be distinguished from the zone of high marginal stresses.

Due to the curvature of the glacier bed the location of the line of minimum effective stress (which coincides with the neutral stress line) is not always found along the geometric centerline, but is displaced towards the inside of the bend. This same effect of the radius of curvature on the location of the centerline has been investigated by Echelmeyer (1983) and Echelmeyer and Kamb (1987). It causes the crevasses on

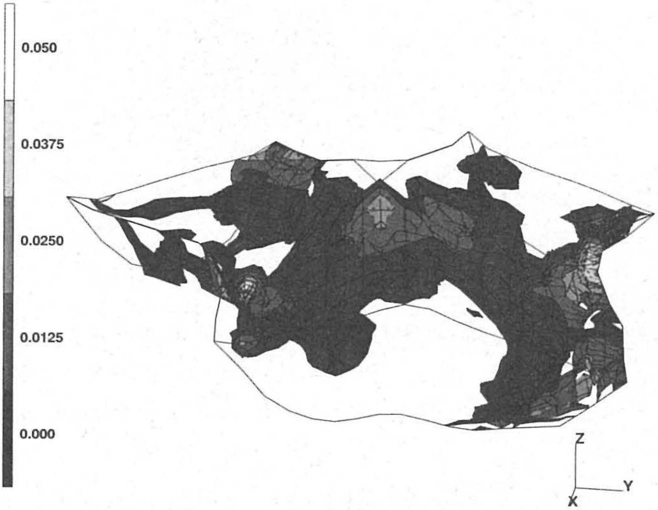

Fig. 5.21: Vertical strain-rate isosurfaces for the confluence area for $n = 3$. Only positive values (extension) are shown. Units are 1/a. Close to the center of the confluence there is zone of ice experiencing large vertical extension. At the junction point strain rates are negative.

the outside of the bend to extend further towards the geometric centerline than those situated on the inside (Meier *et al.*, 1974). This can easily be observed on the Unteraarglacier.

The maximum of the marginal stresses is not alway found directly at the margin, but is sometimes somewhat displaced towards the center. An example of this can be found along the south side of the Unteraarglacier. This shift is caused by the geometry of the glacier bed. As Nye (1965) has pointed out, the maximum of the shear stresses in an infinite and straight parabolic channel cannot be reached at the margin, and is thus displaced toward the center (*cf.* Hutter (1983), p. 448). As expected, and as can by seen by comparing Fig. 3.1 of the glacier bed with Figs. 5.32 and 5.33, there is a good correlation between the displacement of the maximum of

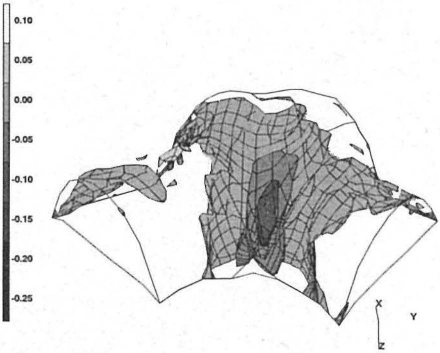

Fig. 5.22: Bottom view of the vertical strain-rate isosurfaces of the confluence area for $n = 3$. Units are 1/a.

the the marginal effective stresses and the marginal cross-sectional slope of the bed.

5.6 Glacier abrasion and the convergence of glaciers

Based on the results given above two reasons can be seen for expecting a change in abrasion rates as glacier ice enters the confluence of two glaciers.

The downward velocity component of the surface ice close to the junction point will result in a transfer of some of the marginal supra-glacier debris cover towards the glacier bed. The corresponding enhancement in basal debris concentration could led to a different abrasion rate along the medial line with respect to the surrounding sections of the bed. Since the increased debris concentration will eventually reduce the sliding velocity the abrasion rate must not, however, necessarily become greater.

The vertical compression of the basal ice, which is, as said above, limited to the center of the confluence area, must on the other hand be expected to lead to an increased abrasion. The contact force between rock fragments and the bed depends (among other factors) on the vertical strain-rate pattern (Hallet, 1981). Vertical convergence will press the rock particles against the bed and give the necessary contact force for the abrasion process to be effective.

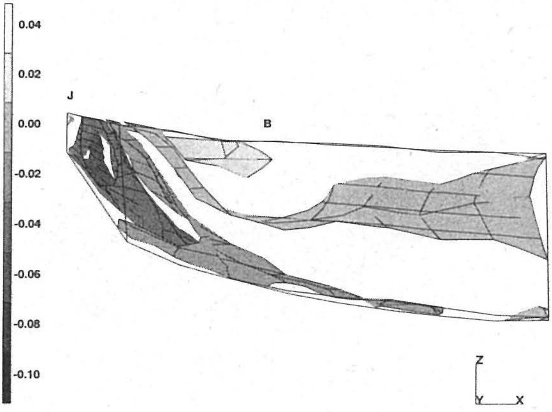

Fig. 5.23: Vertical strain rates $\dot{\epsilon}_{zz}$, for $A = 0.060\,\mathrm{bar}^{-1}\mathrm{a}^{-1}$ and $n = 1$, along a vertical section from the junction point J towards the center of the confluence. B denotes the position of the bore hole. The section is approximately along a flow-line. Units are a^{-1}. Extension is positive, compression is negative.

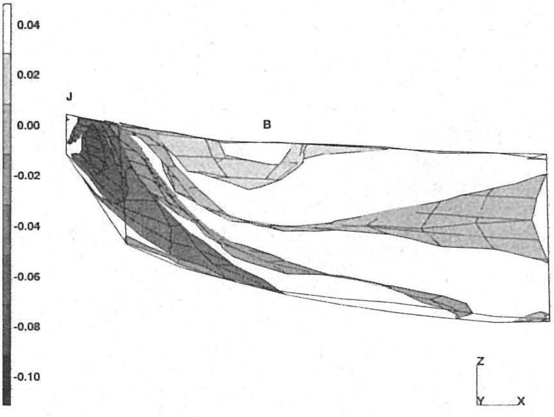

Fig. 5.24: Vertical strain rates $\dot{\epsilon}_{zz}$, for $A = 0.069\,\mathrm{bar}^{-2}\mathrm{a}^{-1}$ and $n = 2$, along a vertical section from the junction point J towards the center of the confluence. B denotes the position of the bore hole. The section is approximately along a flow-line. Units are a^{-1}. Extension is positive, compression is negative.

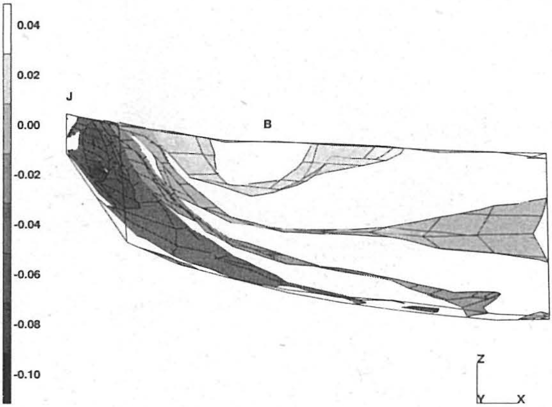

Fig. 5.25: Vertical strain rates $\dot{\epsilon}_{zz}$, for $A = 0.075\,\text{bar}^{-3}\text{a}^{-1}$ and $n = 3$, along a vertical section from the junction point J towards the center of the confluence. B denotes the position of the bore hole. The section is approximately along a flow-line. Units are a^{-1}. Extension is positive, compression is negative.

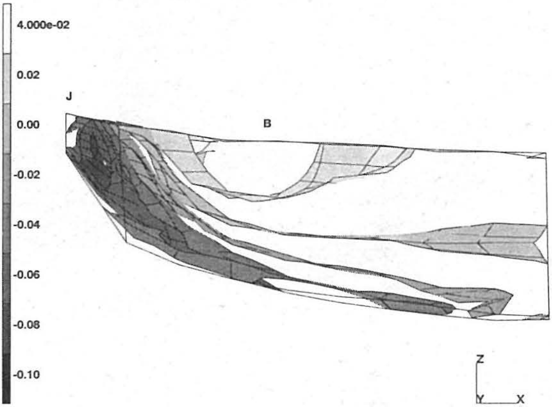

Fig. 5.26: Vertical strain rates $\dot{\epsilon}_{zz}$, for $A = 0.078\,\text{bar}^{-4}\text{a}^{-1}$ and $n = 4$, along a vertical section from the junction point J towards the center of the confluence. B denotes the position of bore hole. The section is approximately along a flow-line. Units are a^{-1}. Extension is positive, compression is negative.

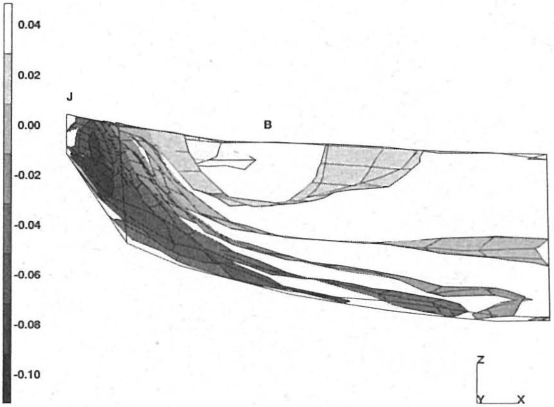

Fig. 5.27: Vertical strain rates $\dot{\epsilon}_{zz}$, for $A = 0.081\,\mathrm{bar}^{-5}\mathrm{a}^{-1}$ and $n = 5$, along a vertical section from the junction point J towards the center of the confluence. B denotes the position of the bore hole. The section is approximately along a flow-line. Units are a^{-1}. Extension is positive, compression is negative.

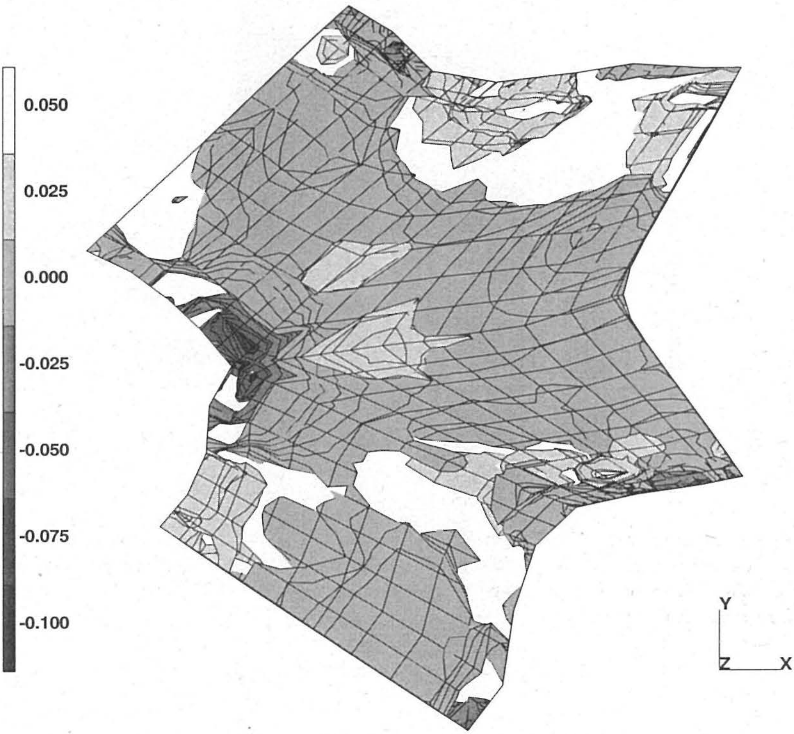

Fig. 5.28: Vertical strain rates $\dot{\epsilon}_{zz}$, for $A = 0.075$ bar^{-3}a^{-1} and $n = 3$. Units are a^{-1}. Extension is positive, compression is negative. Only the confluence area is shown. North points upwards.

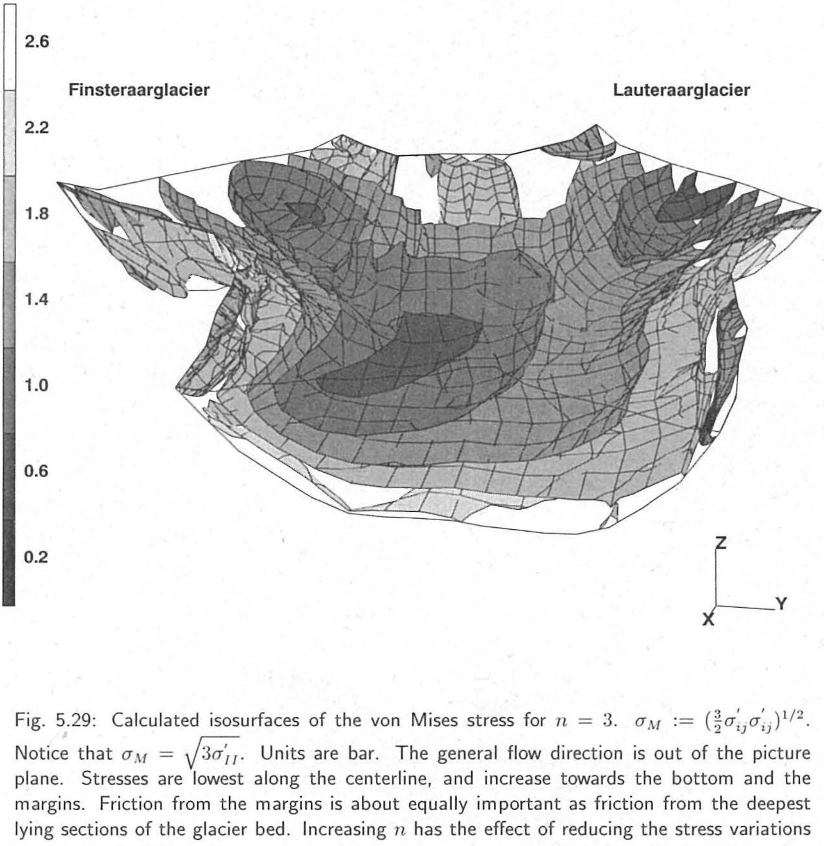

Fig. 5.29: Calculated isosurfaces of the von Mises stress for $n = 3$. $\sigma_M := (\frac{3}{2}\sigma'_{ij}\sigma'_{ij})^{1/2}$. Notice that $\sigma_M = \sqrt{3\sigma'_{II}}$. Units are bar. The general flow direction is out of the picture plane. Stresses are lowest along the centerline, and increase towards the bottom and the margins. Friction from the margins is about equally important as friction from the deepest lying sections of the glacier bed. Increasing n has the effect of reducing the stress variations over the bed. Although there is a local maximum of σ_M found close to the junction point, stresses are not exceptionally large there.

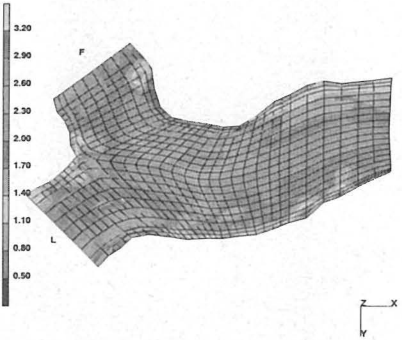

Fig. 5.30: Bottom view of the von Mises stresses σ_M for $n = 1$ in units of bar. F refers to Finsteraarglacier, and L to Lauteraarglacier. The largest stress concentrations are found where there is an abrupt change in flow direction, and along the sections of the bedrock lying closest to the centerline.

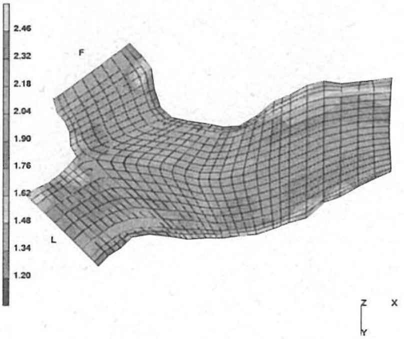

Fig. 5.31: Bottom view of the von Mises stresses σ_M for $n = 5$ in units of bar. F refers to Finsteraarglacier, and L to Lauteraarglacier.

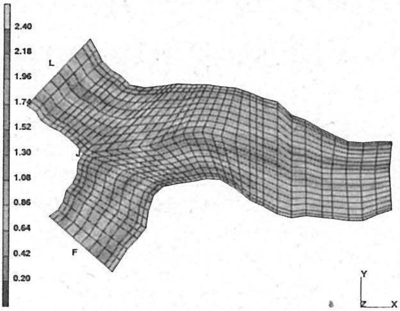

Fig. 5.32: Surface von Mises stresses σ_M for $n = 1$ in units of bar. The area close to J displays a notably large stresses and has a strongly localized maximum.

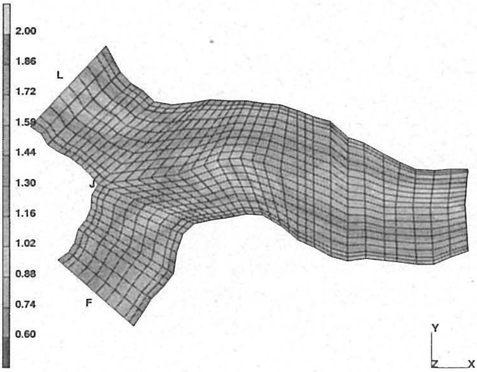

Fig. 5.33: Surface von Mises stresses σ_M for $n = 5$ in units of bar. The longitudinal curvature of the glacier causes the stress neutral line to move toward the inside of the bend.

CHAPTER 6

Conclusions and Recommendations for Further Research

6.1 Measurements

Measurements of surface velocities showed the centerline of the confluence area of the Unteraarglacier to be subjected to a transversal compression that exceeds a concomitant longitudinal extension in magnitude.

Surface velocities are considerably smaller during the winter than summer, *cf.* Figs. 3.12 and 3.13. Whereas the summer velocities are know to be subjected to strong temporal variations, velocities are constant during winter. No variation in winter velocities could be detected despite repeated measurements of marker velocities over two winters.

Horizontal strain rates and the orientation of the principal axis during the winter period are different from those of the summer period, *cf.* Table 3.3. The annual change in basal sliding thus strongly affects the internal deformation of the ice.

At a drilling site located almost at the center of the confluence (*cf.* Fig. 3.3) measurements of the vertical displacements of magnetic rings gave quantitative information on the variation of vertical strain rates with depth. Close to the surface $\dot{\epsilon}_{zz}$ is positive, decreases in magnitude with depth, and then becomes negative, *cf.* Fig. 3.10.

Radio-echo soundings were used to get a detailed picture of the bed-rock, *cf.* Fig. 3.1. They indicated the bedrock to lie some 30 m further down at the confluence than did previous measurements.

Direct comparison of aerial photographs gave annual and summer surface velocities with a spatial coverage that could hardly be obtained with traditional methods, *cf.* Figs. 3.11 and 3.12. Displacements over one year were at the upper limit of what could be detected by the method. Using aerial photographs taken about one month apart gave much better results. Note that estimating the field of annual surface velocities of glaciers is a questionable undertaking in itself since the velocities so obtained are average velocities, that in general correspond to no actual physical situation.

6.2 Theory

The overall strain-rate regime in a confluence can be understood in terms of three different mechanisms: 1) the apparent ice thickening along the medial moraine from the junction point towards the center, 2) the change in the mean flow direction of the two converging arms within the confluence and the corresponding lateral compression, and 3) the velocity increase along the medial moraine from the junction point (J) toward the confluence center.

A map-plane model was used to elucidate the strain-rate pattern at the surface, caused by the change in boundary conditions at the junction point. The results have been summarized in Sec. 4.3. One of the results obtained is that there must be a local surface depression in the vicinity of the junction point, and two super-elevated zones on the marginal sides of the tributaries facing the junction point. A corresponding displacement of contour lines can not only be seen on the Unteraarglacier but also at confluences on numerous glaciers elsewhere.[1]

The effect of the apparent ice thickening along the medial moraine from the junction point towards the center of the confluence on the vertical strain-rate variation was investigated by calculating flow over a sinusoidal bed. No-slip and free-slip boundary conditions were used. For the no-slip boundary condition a vertical strain-rate variation results that is in qualitative agreement with that observed.

With a fully three-dimensional non-linear model the flow field of the Unteraarglacier was calculated. A quantitative comparison of measured and calculated winter velocities revealed systematic errors for all values of n in Glen's flow law. The errors were however rather small, *i.e.* maximum of 15%. Note that the model had only two adjustable parameters. The cause of the systematic errors is not clear. One possible explanation is of course that the flow law itself is not an adequate description of the mechanical properties of glacier ice, and it is speculated that Glen's flow law does not correctly describe the change in effective viscosity as the stress regime changes from pure shear ($\sigma'_{ij} = 0$, if $i = j$), to no shear ($\sigma'_{ij} = 0$, if $i \neq j$). But other explanations are also possible. The applied boundary conditions (no slip) would, for example, be wrong if the glacier slides during winter, which although considered to be unlikely cannot be excluded. The assumption of isotropic and uniform ice is also somewhat questionable.

The qualitative agreement of the numerical calculation with field observations is excellent. All of the main features of the observed flow were reproduced by the calculations. No adjustment of parameters was needed to obtain this agreement. The general conclusions reached with the help of the idealized two-dimensional models were all confirmed by the three-dimensional calculations. Fig. 5.15 gives an overview of the vertical velocity variation along the surface caused by the dynamics of the confluence. One of the surprising results of the 3D calculations is that in the immediate vicinity of the junction point the surface ice is compressed in the vertical direction. Only somewhat further from the junction are the vertical surface strain rates positive.

The ice-cored medial moraine is not caused by the dynamics of the confluence. Differential ablation is the sole cause of the moraine ridge. The ridge starts to form

---

[1] How commonly this effect can be found at glacier confluences was investigated by inspecting maps from glaciated areas in the Alps, China and Alaska. No systematic study was done but it was concluded that practically all confluences display this feature.

at some distance away from the junction point where the differential ablation more than compensates the downward vertical movements at the junction point.

In general the following flow characteristics are expected:

- Transversal compression and longitudinal extension will be found along the centerline. Where the glacier thickens along the medial line the vertical strain rates integrated over the depth will be positive. For no-slip boundary conditions vertical strain rates close to the bed will be negative (compression), and for free-slip (perfect sliding) vertical strain rates will be positive (extension) throughout the whole thickness of the glacier.
- If there is no marginal sliding the maximum of transversal compression at the confluence surface will not be situated close to the junction point (J), but some distance away from it in the down-flow direction. This distance will, however, be small compared to the glacier dimensions. Since transversal flow gradients are zero at J the local surface depression at J will cause a flow reversal. This has been measured and can be seen in Fig. 3.12.
- Super-elevated zones will form at the confluence margins facing the junction point. The resulting surface inclination towards the junction point is needed to drive the transverse flow associated with the shift of the velocity maximum from the center of the two tributaries towards the centerline of the confluence. Theoretically this transverse flow should cause a transverse extension close to the margins facing J, but since this will be superimposed on the strong marginal shear caused by the main flow this will, in general, hardly be a detectable effect.

6.3 Recommendations for further research

The limited number of velocity measurements did not make it possible to localise precisely the spatial extent of the zone of surfacial vertical extension. In particular the possibility of a zone of vertical compression close to the junction point cannot be ruled out. This is predicted by the numerical model and should be put to the test.

Measurement of vertical strain rates with magnetic rings is a simple and effective way of obtaining valuable information on the flow behavior. Since, according to the numerical model, the vertical strain-rate pattern varies strongly in all three dimensions, measurement of $\dot{\epsilon}_{zz}$ will give a further test of the correctness of the numerical model.

It is also important for further quantitative work that efforts towards direct measurements of slip velocity are undertaken.

Measurements of ice movements along the medial moraine relative to the adjacent ice give information on the flow behavior in the low stress limit and would strongly augment the information on the mechanical properties of ice that was derived, in this work from the magnitude and spatial variation of horizontal flow velocities.

APPENDIX A

Listing of Measurement Readings

A.1 Displacement of magnetic rings

In the following three tables the vertical positions of the three magnetic rings used in the measurement campaign are listed. These readings were used for the calculation of vertical strain rates.

day	month	hour	minutes	depth [m]
14	9	17	5	101.446
15	9	10	35	101.456
15	9	14	50	101.459
15	9	17	20	101.459
16	9	10	00	101.469
16	9	15	00	101.470
17	9	8	20	101.482
17	9	17	40	101.485
18	9	10	15	101.494
19	9	13	15	101.508
20	9	14	40	101.520
21	9	10	55	101.529
22	9	10	5	101.540
1	10	11	30	101.686

Table A.1: Changes of vertical position of the magnetic ring in the 100 m deep bore hole with time. Errors of vertical measurements estimated to be ±0.002 m.

day	month	hour	minutes	depth [m]
14	9	14	30	153.357
14	9	17	00	153.357
15	9	10	50	153.372
15	9	11	40	153.373
15	9	16	20	153.378
15	9	17	00	153.378

Table A.2: Changes of vertical position of the magnetic ring in the 150 m deep bore hole with time. Errors of vertical measurements estimated to be ±0.002 m.

day	month	hour	minutes	depth [m]
14	9	18	00	195.559
15	9	10	00	195.572
15	9	16	40	195.582
16	9	10	10	195.597
16	9	11	00	195.598
16	9	14	10	195.599
17	9	8	30	195.617
17	9	15	40	195.622
18	9	10	00	195.640
19	9	13	5	195.663
20	9	14	20	195.679
21	9	10	45	195.695
22	9	10	0	195.720
1	10	11	30	195.932

Table A.3: Changes of vertical position of the magnetic ring in the 200 m deep bore hole with time. Errors of vertical measurements estimated to be $\pm 0.002\,\mathrm{m}$.

A.2 Marker velocities

In the following tables measured velocities of markers are listed. From left to right the columns give marker numbers, time of repeated measurement in days since 17 August 1991, time between measurements in days , velocities in the x and y directions (x pointing eastwards, y northwards and z upwards), and the marker positions. Markers 91100, 91200 and 91300 were situated at the 100, 200 and the 300 m bore holes respectively.

Marker	t [d]	δt [d]	v_x [m/a]	v_y [m/a]	x [m]	y [m]
9112	43.000	43.000	21.575	-8.579	657183.750	158367.705
9112	121.000	78.000	16.389	-6.743	657186.770	158366.480
9112	205.493	84.493	16.384	-6.830	657190.415	158364.970
9113	43.000	43.000	25.313	-10.023	657166.450	158296.960
9113	121.000	78.000	19.714	-7.586	657170.045	158295.560
9114	43.000	43.000	27.946	-10.363	657161.215	158231.640
9114	121.000	78.000	21.587	-8.054	657165.165	158230.170
9115	43.000	43.000	31.174	-9.598	657153.065	158140.685
9115	121.000	78.000	24.210	-7.867	657157.485	158139.280
9116	43.000	43.000	33.552	-6.286	657140.435	157978.440
9116	121.000	78.000	25.567	-4.730	657145.140	157977.565
9121	43.000	43.000	18.093	11.807	656985.175	157651.745
9121	121.000	78.000	13.252	8.007	656987.655	157653.295
9121	204.754	83.754	13.214	8.678	656990.585	157655.145
9121	208.667	3.912	14.937	8.402	656992.180	157656.185

Table A.4: Marker velocities

Marker	t [d]	δt [d]	v_x [m/a]	v_y [m/a]	x [m]	y [m]
9122	43.000	43.000	24.973	13.336	657089.160	157662.695
9122	121.000	78.000	19.152	9.459	657092.675	157664.490
9122	204.743	83.743	18.667	9.639	657096.860	157666.605
9122	208.668	3.925	19.542	8.375	657099.105	157667.755
9123	43.000	43.000	28.880	11.467	657160.330	157690.535
9123	121.000	78.000	21.915	8.382	657164.370	157692.105
9123	204.741	83.741	22.201	8.854	657169.255	157694.015
9123	208.670	3.929	23.240	7.437	657171.925	157695.070
9124	43.000	43.000	35.421	10.108	657338.745	157753.355
9124	121.000	78.000	27.113	7.211	657343.725	157754.720
9131	43.000	43.000	30.579	17.838	657213.390	157625.450
9131	121.000	78.000	22.992	13.299	657217.645	157627.920
9131	208.604	87.604	23.348	13.509	657222.900	157630.960
9132	43.000	43.000	31.683	17.243	657236.145	157631.635
9132	121.000	78.000	23.648	12.690	657240.535	157634.005
9132	208.604	87.604	24.140	12.758	657245.955	157636.890
9133	43.000	43.000	30.154	18.942	657219.195	157602.125
9133	121.000	78.000	22.711	13.861	657223.395	157604.720
9133	208.604	87.604	23.098	13.842	657228.590	157607.860
9134	43.000	43.000	29.560	17.498	657189.720	157618.960
9134	121.000	78.000	22.055	14.142	657193.815	157621.500
9134	208.604	87.604	22.598	13.759	657198.880	157624.660
9135	43.000	43.000	30.919	15.884	657206.680	157648.325
9135	121.000	78.000	23.086	11.894	657210.965	157650.530
9135	208.604	87.604	23.432	11.966	657216.240	157653.235
9141	43.000	43.000	30.494	19.961	657252.035	157577.725
9141	121.000	78.000	23.413	15.547	657256.330	157580.560
9142	43.000	43.000	29.560	22.849	657331.550	157476.935
9142	121.000	78.000	22.009	16.858	657335.640	157480.080
9142	204.736	83.736	22.377	17.230	657340.555	157483.855
9142	208.662	3.926	22.330	10.234	657343.240	157485.885
9143	43.000	43.000	25.907	22.085	657433.485	157354.930
9143	121.000	78.000	19.901	16.436	657437.135	157357.985
9143	204.733	83.733	19.499	16.620	657441.495	157361.645
9143	208.642	3.910	19.618	8.408	657443.835	157363.595
9144	43.000	43.000	22.934	19.537	657489.960	157285.670
9144	121.000	78.000	17.747	14.891	657493.205	157288.410
9144	204.733	83.733	17.361	14.875	657497.090	157291.705
9144	208.639	3.906	15.899	8.417	657499.165	157293.455
91100	43.000	43.000	29.984	17.923	657195.795	157622.925
91200	43.000	43.000	29.984	17.923	657199.755	157622.055
91300	43.000	43.000	27.012	16.564	657205.860	157625.155
92101	208.615	3.906	1.870	9.350	656802.250	157425.230
92102	208.611	3.899	8.430	11.240	656878.555	157387.560
92103	208.608	3.892	7.507	15.014	656952.740	157333.360

Table A.5: Marker velocities

Marker	t [d]	δt [d]	v_x [m/a]	v_y [m/a]	x [m]	y [m]
92104	208.604	3.066	13.104	26.209	657109.885	157220.640
92105	208.601	3.877	13.189	19.784	657203.760	157172.085
92106	208.597	3.872	6.604	17.925	657325.905	157086.265
92107	208.594	3.872	2.830	10.378	657414.245	157001.445
92201	208.580	3.853	9.478	19.905	656898.440	156519.145
92202	208.576	3.844	14.251	22.802	656756.165	156654.800
92203	208.569	3.833	8.577	22.872	656741.825	157017.280
92301	208.684	3.906	16.831	7.480	657514.030	158292.030
92302	208.682	3.915	27.058	4.665	657534.245	158164.015
92303	208.681	3.917	30.774	3.730	657554.825	158026.940
92304	208.678	3.918	34.492	1.864	657571.555	157942.390
92305	208.677	3.920	31.679	3.727	657602.720	157882.200
92306	205.506	0.721	35.469	25.335	657577.445	157758.515
92306	208.674	3.168	28.823	11.529	657577.605	157758.590
92307	205.512	0.724	30.286	25.238	657518.790	157598.695
92307	208.656	3.144	25.555	8.131	657518.930	157598.755
92308	208.646	3.128	23.350	7.005	657646.490	157476.930
92309	208.635	3.115	18.763	0.000	657669.850	157388.320
92310	208.633	3.108	18.801	4.700	657629.740	157326.460
92311	208.632	3.104	15.296	4.707	657627.075	157259.350
92402	208.698	3.215	31.808	-13.632	658869.480	157809.770
92501	208.675	3.181	16.077	-10.335	657123.530	158401.415
92503	208.681	3.183	18.358	-13.769	657004.360	158243.720
92504	208.682	3.182	19.514	-16.070	656913.605	158137.860
92505	208.683	3.181	18.374	-14.929	656792.580	158013.155
92506	208.684	3.180	14.932	-13.784	656708.535	157902.590
92601	208.663	3.056	40.642	-59.768	655940.280	159452.160
92602	208.660	3.042	39.627	-18.012	655845.275	159364.345
92603	208.656	3.042	34.824	-25.217	655751.125	159298.795
1001	490.000	49.000	24.449	18.113	656532.970	156166.545
1002	490.000	49.000	21.468	20.797	656564.320	156545.415
1003	490.000	49.000	16.995	21.244	656601.340	156729.615
1004	490.000	49.000	19.306	-20.350	656104.115	158756.485
1005	490.000	49.000	20.573	-21.021	656192.930	158864.770
1006	490.000	49.000	21.542	-19.828	656281.815	158967.510
1007	490.000	49.000	0.969	0.596	656802.715	157635.370
1008	490.000	49.000	5.143	3.354	656875.445	157623.235
1009	490.000	49.000	12.896	8.125	656996.825	157646.995
1010	490.000	49.000	16.399	17.070	657376.000	157296.625
1011	490.000	49.000	22.735	14.983	657377.565	157507.545
1012	490.000	49.000	25.568	9.169	657538.085	157604.275
1013	490.000	49.000	26.313	4.547	657851.585	157699.195
1014	490.000	49.000	26.835	5.665	657619.480	157855.920
3001	490.000	49.000	21.915	-12.076	658651.810	157514.570
3002	490.000	49.000	20.424	-12.076	658921.580	157812.380
3003	490.000	49.000	15.355	-7.230	658876.180	158091.075
3004	490.000	49.000	16.548	-6.112	659926.360	157498.790
3005	490.000	49.000	16.772	-5.889	659899.385	157181.865
3006	490.000	49.000	9.243	-2.013	660473.140	157064.655
3007	490.000	49.000	14.014	-1.938	660452.790	157513.680

Table A.6:

Bibliography

Agassiz, L. (1847). *Nouvelles études et expériences sur les glaciers actuels.* V. Masson, Paris.

Akima, H. (1978). A method of bivariate interpolation and smooth surface fitting for irregularly distributed data points. *ACM Transactions on Mathematical Software*, 4:148–159.

Allen, C. R., Kamb, W. B., Meier, M. F., and Sharp, R. P. (1960). Structure of the Lower Blue Glacier, Washington. *Journal of Geology*, 68:601–625.

Alley, R. B. (1992). Flow-law hypotheses for ice-sheet modeling. *Journal of Glaciology*, 38(129):245–256.

Anderton, P. W. (1970). Deformation of surface ice at a glacier confluence. In Bushnell, V. C. and Ragle, R. H., editors, *Icefield Ranges Research Projects. Scientific Results*, volume 2, pages 59–76. American Geographical Society and Arctic Institute of North America.

Balise, M. J. and Raymond, C. F. (1985). Transfer of basal sliding variations to the surface of a linearly viscous glacier. *Journal of Glaciology*, 31(109):308–318.

Barcilon, V. and MacAyeal, D. R. (1993). Steady flow of a viscous ice stream across a no-slip/free-slip transition at the bed. *Journal of Glaciology*, 39(131):167–185.

Bathe, K. J. (1982). *Finite Element Procedures in Engineering Analysis.* Prentice-Hall Inc., Englewood Cliffes, New Jersey.

Brecher, H. S. (1969). Surface velocity measurements on the Kaskawulsh Glacier. In Bushnell, V. C. and Ragle, R. H., editors, *Icefield Ranges Research Projects. Scientific Results*, volume 1, pages 127–144. American Geographical Society and Arctic Institute of North America.

Budd, W. F. and Jacka, T. H. (1989). A review of ice rheology for ice sheet modeling. *Cold Regions Science and Technology*, 16:107–144.

Casassa, G. (1992). Foliation on Tyndall Glacier, southern Patagonia. *Bulletin of Glacier Research*, 10:75–77.

Chung, T. J. (1978). *Finite Element Analysis in Fluid Dynamics.* McGraw-Hill, Inc.

Clarke, G. K. C. (1969). Geophysical measurements on the Kaskawulsh and Hubbard Glaciers. In Bushnell, V. C. and Ragle, R. H., editors, *Icefield Ranges Research Projects. Scientific Results*, volume 1, pages 89–106. American Geographical Society and Arctic Institute of North America.

Colbeck, S. C. and Evans (1973). Flow law of temperate glacier ice. *Journal of Glaciology*, 12(64):72–86.

Collins, I. F. (1970). A slip-line field analysis of the deformation at the confluence of two glacier streams. *Journal of Glaciology*, 9(56):169–193.

Dansgaard, W. and Johnsen, S. J. (1969). A flow model and a time scale for the ice core from Camp Century, Greenland. *Journal of Glaciology*, 8(53):215–223.

Dewart, G. (1970). Seismic investigation of ice properties and bedrock topography at the confluence of the north and central arms of Kaskawulsh glacier. In Bushnell, V. C. and Ragle, R. H., editors, *Icefield Ranges Research Projects. Scientific Results*, volume 2, pages 77–102. American Geographical Society and Arctic Institute of North America.

Doake, C. S. M. and Wolff, E. W. (1985). Flow law for ice in polar ice sheets. *Nature*, 314(6008):255–257.

Dozier, J. (1970). Channel adjustements in supraglacial streams. In *Studies of Morphology and Stream Action on Ablating Ice*, pages 67–117. The Arctic Institute of North America. Res. Paper No. 57.

Duval, P., Ashby, M. F., and Anderman, I. (1983). Rate-controlling processes in the creep of polycrystalline ice. *Journal of Physical Chemistry*, 87(21):4066–4047.

Echelmeyer, K. and Kamb, B. (1987). Glacier flow in a curving channel. *Journal of Glaciology*, 33(115):281–292.

Echelmeyer, K. A. (1983). *Response of Blue Glacier to a perturbation in ice thickness: theory and observation.* PhD thesis, California Institute of Technology.

Ewing, K. J. (1970). Supraglacial streams on the Kaskawulsh glacier, Yukon territory. In *Studies of Morphology and Stream Action on Ablating Ice*, pages 119–167. The Arctic Institute of North America. Res. Paper No. 57.

Eyles, N. (1976a). Morphology and development of medial moraines: comments on the paper by R. J. Small and M. J. Clark. *Journal of Glaciology*, 17:161–162.

Eyles, N. (1976b). Morphology and development of medial moraines: further comments on the paper by R. J. Small and M. J. Clark. *Journal of Glaciology*, 17:164–165.

Eyles, N. and Rogerson, R. J. (1977). Glacier movement, ice structures, and medial moraine form at a glacier confluence, Berendon Glacier, British Colombia, Canada. *Can J. Earth Sci.*, 14:2807–2816.

Eyles, N. and Rogerson, R. J. (1978). A framework for the investigation of medial moraine formation: Austerdalsbreen, Norway, and Berendon Glacier, British Colombia, Canada. *Journal of Glaciology*, 20:99–113.

Fabri, K. (1991). Eisdickenmessungen im Aaregletschergebiet, eine Anwendung von Radio-Echo-Sounding. Praktikumsarbeit an der VAW, ETH-Zürich, unter Anleitung von M. Funk und G. Meyer (unveröffentlicht).

Flotron, A. (1924 to date). Jährliche Berichte über die Ergebnisse der Gletschermessungen im Auftrag der Kraftwerke Oberhasli. Annual reports.

Flotron, A. (1979). *Verschiebungsmessungen aus Luftbildern*, volume 41, pages 39–44. Mitteilungen der Versuchsanstalt für Wasserbau, Hydrologie und Glaziologie der ETH Zürich, Gloriastrasse 37-39, ETH-Zentrum, CH-8092 Zürich.

Flotron, A. (Jahrg. 71, Fachblatt, 1973). Photogrammetrische Messung von Gletscherbewegungen mit automatischer Kamera. *Vermessung, Photogrammetrie und Kulturtechnik*, Ht. 1-73:15–17.

Funk, M. (1986). Glaziologisches Gutachten im Zusammenhang mit der allfälligen Erstellung einer Stauanlage Grimsel-West. Bericht Nr. 20.3, unveröffentlicht, VAW. Im Auftrag der Kraftwerke Oberhasli AG, Innertkirchen.

Funk, M. (1987a). Schlussbericht über die Sondierungen 1986. Bericht Nr. 20.4, unveröffentlicht, VAW. Im Auftrag der Kraftwerke Oberhasli AG, Innertkirchen.

Funk, M. (1987b). Sondierungen Unteraargletscher und Gletscherrückzug. Bericht Nr. 20.6, unveröffentlicht, VAW. Im Auftrag der Kraftwerke Oberhasli AG, Innertkirchen.

Funk, M. (1987c). Überprüfung des angenommenen Gletscherrückzuges; Abschätzung des Schmelzvermögens des Sees. Bericht Nr. 20.5, unveröffentlicht, VAW. Im Auftrag der Kraftwerke Oberhasli AG, Innertkirchen.

Funk, M., Echelmeyer, K., and Iken, A. (1994). Mechanisms of Fast Flow in Jakobshavns Isbrae, Greenland; Part II: Modeling of englacial temperatures. *Journal of Glaciology*. In press.

Funk, M. and Röthlisberger, H. (1989). Forecasting the effects of a planned reservoir that will partially flood the tongue of Unteraargletscher in Switzerland. *Annals of Glaciology*, 13:76–80.

Gartling, D. K., Nickell, R. E., and Tanner, R. I. (1977). A finite element convergence study for accelerating flow problems. *International Journal for Numerical Methods in Engineering*, 11:1155–1174.

Glen, J. W. (1952). Experiments on the deformation of ice. *Journal of Glaciology*, 2(12):111–114.

Glen, J. W. (1955). The creep of polycrystalline ice. *Proceedings of the Royal Society of London, Ser A*, 228(1175):519–538.

Gomez, B. and Small, R. J. (1985). Medial moraines of the Haut glacier D'Arolla, Valais, Switzerland: debris supply and implications for moraine formation. *Journal of Glaciology*, 31(109):303–307.

Gudmundsson, G. H. (1989). Modellrechnungen zu rezenten Alpenhebungen. Diplomarbeit, Geophysical Institute ETH — Zürich.

Gudmundsson, G. H. (1994a). The characteristics of creeping flow close to bedrock undulations, and the form of the sliding law in the absence of friction, bed separation and regelation, for linear and non-linear ice rheology and a sinusoidal bed. Mitteilung, Versuchsanstalt für Wasserbau, Hydrologie und Glaziologie der ETH Zürich, Gloriastrasse 37-39. ETH-Zentrum, CH-8092 Zürich. in press.

Gudmundsson, G. H. (1994b). *Convergent Glacier Flow and Perfect Sliding Over a Sinusoidal Bed.* PhD thesis, ETH Zürich. Nr. 10711.

Haefeli, R. (1970). Changes in the behaviour of the Unteraargletscher in the last 125 years. *Journal of Glaciology*, 9(56):195–212.

Hallet, B. (1981). Glacial abrasion and sliding: their dependence on the debris concentration in basal ice. *Annals of Glaciology*, 2:23–28.

Harrison, W. D. (1975). A measurment of surface-perpendicular strain-rate in a glacier. *Journal of Glaciology*, 14(70):31–37.

Hodge, S. M. (1974). Variations in the sliding of a temperate glacier. *Journal of Glaciology*, 13(69):349–369.

Holdsworth, G. (1969a). An examination and analysis of the formation of transverse crevasses, Kaskawulsh Glacier. In Bushnell, V. C. and Ragle, R. H., editors, *Icefield Ranges Research Projects. Scientific Results*, volume 1, pages 109–126. American Geographical Society and Arctic Institute of North America.

Holdsworth, G. (1969b). Primary transverse crevasses. *Journal of Glaciology*, 8(52):107–129.

Hugi, F. J. (1830). *Naturhistorische Alpenreise.* Amiet-Lutiger, Solothurn.

Hugi, F. J. (1842). *Über das Wesen der Gletscher.* J. G. Cotta'scher Verlag, Stuttgart und Tübingen.

Hutter, K. (1983). *Theoretical glaciology; material science of ice and the mechanics of glaciers and ice sheets.* D. Reidel Publishing Company/Tokyo, Terra Scientific Publishing Company.

Hutter, K. and Olunloyo, V. O. S. (1980). On the distribution of stress and velocity in an ice strip which is partly sliding over and partly adhering to its bed, using a Newtonian viscous approximation. *Proceedings of the Royal Society of London, Ser A*, 373(1754):385–403.

Hutter, K. and Olunloyo, V. O. S. (1981). Basal stress concentrations due to abrupt changes in boundary conditions: a cause for high till concentration at the bottom of a glacier. *Annals of Glaciology*, 2:29–44.

Iken, A. (1978). Variations of surface velocities of some Alpine glaciers measured at intervals of a few hours. *Zeitschrift für Gletscherkunde und Glazialgeologie*, 13:23–35.

Iken, A. (1981). The effect of the subglacial water pressure on the sliding velocity of a glacier in an idealized numerical model. *Journal of Glaciology*, 27(97):407–421.

Iken, A. and Bindschadler, A. (1986). Combined measurements of subglacial water pressure and surface velocity of Findelengletscher, Switzerland: Conclusions about drainage system and sliding mechanism. *Journal of Glaciology*, 32(110):101–119.

Iken, A., Röthlisberger, H., Flotron, A., and Häberli, W. (1983). The uplift of the Unteraargletscher at the beginning of the melt season – a consequence of water storage at the bed? *Journal of Glaciology*, 29(101):28–47.

Jacka, T. H. (1984a). Laboratory studies on relationship between ice crystal size and flow rate. *Cold Regions Science and Technology*, 10(1):31–42.

Jacka, T. H. (1984b). The time and strain required for development of minimum strain rates in ice. *Cold Regions Science and Technology*, 8(3):261–268.

Kadota, T., Naruse, R., Skvarca, P., and Aniya, M. (1992). Ice flow and surface lowering of Tyndall Glacier, southern Patagonia. *Bulletin of Glacier Research*, 10:63–68.

Kleiber, M. (1989). *Incremental Finite Element Modelling in Non-linear Solid Mechanincs*. Ellis Horwood Limited.

Knecht, H. and Süsstrunk, A. (1952). Bericht über die seismischen Sondierungen der schweizerischen Gletscherkommission auf dem Unteraargletscher, 1936 - 1950. Bericht No. 512.

Lile, R. C. (1978). The effect of anisotropy on the creep of polycrystalline ice. *Journal of Glaciology*, 21(85):475–483.

Lliboutry, L. A. and Duval, P. (1985). Various isotropic and anisotropic ices found in glaciers and polar ice caps and their corresponding rheologies. *Annals of Geophysics*, 3:207–224.

Loomis, S. R. (1970). Morphology and structure of an ice-cored medial moraine, Kaskawulsh glacier, Yukon. In *Studies of Morphology and Stream Action on Ablating Ice*, pages 1–65. The Arctic Institute of North America. Res. Paper No. 57.

MARC (1992). *MARC/MENTAT User's Manual*. MARC Analysis Research Corporation, 260 Sherida Avenue, Palo Alto, CA 94306, K5 edition.

Meier, M. F., Kamb, B., Allen, C. R., and Sharp, R. P. (1974). Flow of Blue Glacier Olympic Mountains, Washington, U.S.A. *Journal of Glaciology*, 13(68):187–212.

Mellor, M. (1980). Mechanical properties of polycrystalline ice. In Tryde, P., editor, *Physics and mechanics of ice*, pages 217–245, Copenhagen. IUTAM Symposium 1979.

Nye, J. F. (1952). The mechanics of glacier flow. *Journal of Glaciology*, 2(12):82–93.

Nye, J. F. (1953). The flow law of ice from measurements in glacier tunnels, laboratory experiments and the Jungfraufirn borehole experiment. *Proceedings of the Royal Society of London, Ser A*, 219(1193):477–489.

Nye, J. F. (1957). The distribution of stress and velocity in glaciers and ice-sheets. *Proceedings of the Royal Society of London, Ser A*, 239(1216):113–133.

Nye, J. F. (1959). A method of determining the strain-rate tensor at the surface of a glacier. *Journal of Glaciology*, 3(25):409–418.

Nye, J. F. (1965). The flow of a glacier in a channel of rectangular, elliptic or parabolic cross-section. *Journal of Glaciology*, 5(41):661–690.

Paterson, W. S. B. (1981). *The physics of glaciers.* Pergamon Press, Oxford, 2. edition.

Pironneau, O. (1989). *Finite Element Methods for Fluids.* John Wiley & Sons Limited.

Raymond, C. F. (1971). Flow in a transverse section of Athabasca Glacier, Alberta, Canada. *Journal of Glaciology*, 10(58):55–69.

Raymond, C. F. (1980). *Dynamics of snow and ice masses.* S.C. Colbeck *(editor)*, chapter on Temperate valley glaciers, pages 79–139. Academic Press.

Rogers, J. C. and LaChapelle, E. R. (1974). The measurement of vertical strain in glacier bore holes. *Journal of Glaciology*, 13(68):315–319.

Röthlisberger, H. (1967). Recent D. C. resistivity soundings on Swiss glaciers. *Journal of Glaciology*, 6(47):607–621.

Sambeth, U. and Frey, P. (1987a). Auswertung der Geoelektrischen Messungen im unteren Gebiet der Zunge des Unteraargletschers. Technical Report Ref. Nr. 87107, Peter Frey, Geolog. Expertisen, Zug.

Sambeth, U. and Frey, P. (1987b). Geophysikalische Messungen zur Abklärung des Aufbaus des Unteraargletschers, der unterliegenden Sedimente und der Felsoberkante. Technical Report Ref Nr. 87102, Peter Frey, Geolog. Expertisen, Zug.

Shah, R. K. and London, A. L. (1978). *Laminar Flow Forced Convection in Ducts.* Advances in Heat Transfer. Academic Press, Inc., New York.

Small, R. J. and Clark, M. J. (1976a). Morphology and development of medial moraines: reply to comments by N. Eyles. *Journal of Glaciology*, 17:162–164.

Small, R. J. and Clark, M. J. (1976b). Morphology and development of medial moraines: reply to further comments by N. Eyles. *Journal of Glaciology*, 17:165–165.

Smiraglia, C. (1989). The medial moraines of Chicciaio Dei Forni, Valtellina, Italy: Morphology and sedimentology. *Journal of Glaciology*, 35:81–84.

van der Veen, C. J. and Whillans, I. M. (1990). Flow laws for glacier ice: comparison of numerical predictions and field measurments. *Journal of Glaciology*, 36(124):324–339.

Vere, D. M. and Benn, D. I. (1989). Structure and debris characteristics of medial moraines in Jotunheimen, Norway: Implications for maraine classification. *Journal of Glaciology*, 35(120):276–280.

Wagner, P. (1969a). Description and evolution of snow and ice features and snow surface forms on the Kaskawulsh Glacier. In Bushnell, V. C. and Ragle, R. H., editors, *Icefield Ranges Research Projects. Scientific Results*, volume 1, pages 51–54. American Geographical Society and Arctic Institute of North America.

Wagner, P. (1969b). Snow facies and stratigraphy on the Kaskawulsh Glacier. In Bushnell, V. C. and Ragle, R. H., editors, *Icefield Ranges Research Projects. Scientific Results*, volume 1, pages 55–62. American Geographical Society and Arctic Institute of North America.

Zienkiewicz, O. C., Loehner, R., Morgan, K., and Nakazawa, S. (1984). Finite elements in fluid mechanics — a decade of progress. In Gallagher, R. H., Oden, J. T., Zienkiewicz, O. C., Kawai, T., and Kawahara, M., editors, *Finite Elements in Fluids*, volume 5, chapter 1, pages 1–26. John Wiley & Sons Limited.

Acknowledgements

The subject of this work was suggested by Dr. Almut Iken. Her continuous guidance during the course of this study is gratefully acknowledged.

The study was made possible by Prof. Dr. Dr. h. c. D. Vischer, head of the Hydraulics, Hydrology and Glaciology Laboratory (VAW) of the ETH Zürich, who provided all facilities and equipment. His support, particularly during the evaluative stages of the work, is greatly appreciated.

Dr. Martin Funk gave me very valuable assistance during most of the field campaigns. Among other things he took full responsibility for the radio-echo-sounding field work. His generous and unselfish assistance was of great value to me.

Prof. K. Hutter critically reviewed the work and his numerous suggestion greatly enhanced its value.

I want to thank Dr. Ayako Abe-Ouchi, Hermann Bösch, Kristian Fabri, Karina Gut, Martin Lüthi, Bruno Mandela, Hannibal Moore, Willy Schmid (†), Simone Strohm and Jörg Wenzel who gave a helping hand during the field trips.

I also benefited from discussions with Dr. Stephan Wagner and PD Dr. Wilfried Haeberli.

Dr. Peter Collins corrected the English.

Special thanks to Simone Strohm. Her continuous support was essential for the successful completion of this work.

This work was supported by the Swiss National Science Foundation (Schweizerischer Nationalfonds), Grant Nr. 20-29619.90.